工學博士學位論文

Specific Molecule Detection Using Polyacrylonitrile Nanoparticles and Cytotoxicity of Conducting Polymer Nanomaterials

폴리아크릴로니트릴 나노물질을 이용한 특정 분자의 검출 및 기능성 고분자 나노물질의 세포독성규명

2012年 8月

서울大學校 大學院

化學生物工學部

吳 完 奎

Specific Molecule Detection Using Polyacrylonitrile Nanoparticles and Cytotoxicity of Conducting Polymer Nanomaterials

폴리아크릴로니트릴 나노물질을 이용한 특정 분자의 검출 및 기능성 고분자 나노물질의 세포독성규명

指導敎授 張 正 植

이 論文을 工學博士 學位論文으로 提出함

2012年 6月

서울大學校 大學院

化學生物工學部

吳 完 奎

吳完奎의 工學博士 學位論文을 認准함

2012年 6月

委 員 長 _____ (인)

副委員長 _____ (인)

委 員 _____ (인)

委 員 _____ (인)

委 員 _____ (인)

Specific Molecule Detection Using Polyacrylonitrile Nanoparticles and Cytotoxicity of Conducting Polymer Nanomaterials

by

Wan-Kyu Oh

Submitted to the Graduate School of Seoul National

University in Partial Fulfillment of the Requirements for the

Degree of Doctor of Philosophy

August, 2012

Thesis Adviser: Jyongsik Jang

Abstract

Specific Molecule Detection Using Polyacrylonitrile Nanoparticles and Cytotoxicity of Conducting Polymer Nanomaterials

Wan-Kyu Oh

School of Chemical and Biological Engineering

The Graduate School

Seoul National University

Functional polymer nanomaterials are fabricated by chemical oxidation polymerization and emulsion templating polymerization, and evaluate their cytotoxicity and cellular effect. In addition, the functional polymer nanomaterials are applied for detection of specific molecules. In particular, polyacrylonitrile (PAN) nanoparticles with surface modification are used as a cellular imaging agent, anthrax detector, monosaccharide detector, and intracellular hydrogen peroxide detector. Additionally, conducting polymer nanomaterials including polypyrrole (PPy), polyaniline (PANi), and poly(3,4-ethyldioxythiophene) (PEDOT) with controlled sizes and shapes

are employed for nanotoxicological assessments. PAN nanoparticles with ethylenediamine treatment by vapor phase show photoluminescence and are modified with Anti-ErbB2 antibody on the surface for selective cellular imaging. Schiff base modified PAN nanoparticles are additionally treated with lanthanide metal complex, and are applied for an anthrax biomarker. These nanoparticles represent ratiometric detection without calibration due to the internal fluorescence reference, and exhibit a remarkable limit of detection (10 pM) and outstanding selectivity (160×) over aromatic ligands in aqueous solution. Boronate-modified PAN nanoparticles are employed for enantioselective monosaccharide sensors. These nanoparticles show enhanced fluorescence due to photo-induced electron transfer mechanism and enable molecular recognition owing to covalent bonds with enantiomers of monosaccharides, including D-/L-glucose, D-/L-galactose, and D-/L-fructose. Boronic acid pinacol ester-treated PAN nanoparticles are fabricated for a selective H_2O_2 sensor. The representative features of the these nanoparticles that make them particularly attractive for H_2O_2 and ROS detection are the following: they are easily synthesized as PET sensors; they exhibit a characteristic emission peak and peak shift that distinguishes reaction with H_2O_2 from other ROS; they act as a prochelator of metal ions; and compared to organic compounds, the sensing moiety on BPAN polymer

nanoparticles are more thermally stabile and have superior mechanical properties, enabling their use in various biomedical applications. PEDOT nanomaterials with different shapes are investigated about the cytotoxicity and proinflammatory response toward mammalian cells. PPy nanoparticles with five different diameters are prepared for evaluating size-dependent cytotoxicity. PANi nanomaterials with different aspect ratios on human fibroblast cells are investigated by in vitro assays. These results provide new understading of size- and shape-dependent cytotoxicity of conducting polymer nanomaterials.

Keywords: Conducting polymer nanomaterials; Cytotoxicity; Bioimaging; Specific molecule detection; Anthrax detection

Student Number: 2009-30244

List of Abbreviations

AOT: sodium bis(2-ethylhexyl) sulfosuccinate

APS: ammonium persulfate

ATP: adenosine triphosphate

aV: annexin V

BET: Brunauer-Emmett-Teller

CV: cyclic voltamogram

DCF-DA: 2´,7´- dichlorodihydrofluorescein diacetate

DDS: drug delivery system

DLS: dynamic light scattering

EA: elemental analysis

EDA: ethylenediamine

EDX: energy-dispersive X-ray spectroscopy

ELS: electrophoretic light scattering

EMEM: Eagle's minimum essential medium

FACS: flow cytometry

FITC: fluorescein isothiocyanate

FRET: fluorescence resonance energy transfer

FT-IR: Fourier transform-infrared

HEPES: 4-(2-hydroxyethyl)-1-piperazineethanesulfonic acid

HR-TEM: high resolution-transmission electron microscopy

ICP: Inductively coupled plasma

ICT: intramolecular charge transfer

LDH: lactate dehydrogenase

MIP: Molecularly imprinted polymer

PAN: polyacrylonitrile

PANi: polyaniline

PBS: phosphate buffered saline

PEDOT: poly(3,4-ethylenedioxythiophene)

PET: photo-induced electron transfer

PI: propidium iodide

PL: photoluminescent

PPy: polypyrrole

PT: polythiophene

PVA: poly (vinyl alcohol)

PVP: poly(vinyl pyrrolidone)

QD: quantum dot

ROS: reactive oxygen species

TEM: transmission electron microscopy

VDP: vapor deposition polymerization

XPS: X-ray photoelectron spectroscopy

XRD: X-ray diffraction

List of Tables

List of Figures

reaction time. The time increasing (30 min, 1, 2, and 4 h) represents the EDA treatment time on the PAN nanoparticles.

Figure 11. Absorption and emission spectra of PAN and tPAN nanoparticles colloid dispersed in aqueous media (inset: photograph of emission of colloids excited by 365 nm UV lamp).

Figure 12. Cell viability of PAN and tPAN nanoparticle treated human breast cancer cells (SK-BR-3) at different particle concentrations for 24 h. Error bars represent standard deviations (n=3).

Figure 13. Live cell microscopic images of human breast cancer SK-BR- 3 cells incubated with a) tPAN nanoparticles, b) anti-ErbB2 antibody conjugated tPAN nanoparticles, and c) PEG conjugated tPAN nanoparticles.

Figure 14. Time lapse live cell fluorescent images of antibody conjugated tPAN nanoparticles in SK-BR-3 cells over 11 h. The blue represents nanoparticles in cells. The scale of each square is 50 μm. The images are taken at 30 min interval for 11 h.

Figure 15. Differential interface contrast (DIC) and fluorescent z-sectioning images of SK-BR-3 cell treated with antibody conjugated tPAN nanoparticles for 24 h. The sections are ordered from apex of the cell to the near substrate plane. Z-scan step width is 0.1μm. (Scale bars: 20 μm)

Figure 16. Schematic diagram for fabrication procedure of Eu-PAN

Figure 35. Schematic diagram of H_2O_2 detection using BPAN nanoparticles and representative fluorescence spectra of PAN (blue line) and BPAN (red line) nanoparticles.

Figure 36. Ratiometric fluorescence spectral changes of 10 μg mL^{-1} BPAN nanoparticles in the presence of H_2O_2 as a function of different excitation wavelength: a) 300 nm, b) 320 nm, and c) 360 nm. Data were acquired at 25^oC in 20 mM HEPES, pH 7, 1min after the addition of H_2O_2. H_2O_2 concentrations represent 0, 20, 40, 60, and 80 μM.

Figure 37. Fluorescence response of 10 μg mL^{-1} BPAN nanoparticle solution in the presence of H_2O_2 and other ROS excited at a) 300 nm, b) 320 nm, and c) 360 nm. Bars exhibit fluorescence changes after addition of each ROS(20 μM) compared with pristine BPAN nanoparticle solution. Data acquired at 25 ^oC in 20 mM HEPES, pH 7. Emission was collected between a) 320 and 500 nm; b) 340 and 500 nm; c) 380 and 500 nm. Values exhibit mean ±SD and each experiment was performed in triplicate.

Figure 38. Live cell differential interference contrast (DIC) BPAN-treated RAW264.7 cells (a) 5 and b) 10 μg mL^{-1}); left images are before treatment of PMA and right images are 10 min after treatment of 1 μg mL^{-1} of PMA. Scale bars = 50 μm; Mean fluorescence intensity (MFI) values of BPAN-treated RAW264.7 cells (a) 5 and b) 10 μg mL^{-1}); left bar represents before

treatment of PMA and right bar indicates 10 min after treatment of 1 μg mL^{-1} of PMA.

Figure 39. Flow cytometry analyzes of particle uptake. Quantification of cellular uptake of a) negative control, b) 10 μg mL^{-1} and c) 100 μg mL^{-1} FITC-modified PAN nanoparticles. Upper right values mean the number of nanoparticle-contained PC-12 cells and upper left median values indicate the amount of uptaken nanoparticles.

Figure 40. Viability of RAW264.7 cells incubated with PAN (closed squares) and BPAN nanonanoparticles (open circles) for 24 h. The viability was calculated relative to negative control. ROS production by RAW264.7 cells after being incubated with PAN (closed bars) and BPAN nanoparticles (open bars). H_2O_2 (0.02%) was used as positive control. Values exhibit mean ± SD and each experiment was performed in triplicate.

Figure 41. TEM images of PEDOT nanomaterials of three different shapes (width: 55±20 and 50±10 nm): a) PEDOT-1, b) PEDOT-2, and c) PEDOT-3.

Figure 42. Microscope images of PEDOT nanomaterial-treated IMR90 cells and J774A.1 cells at concentration of 10 μg mL^{-1}; Scale bars = 10 μm.

Figure 43. Viability of fibroblast (IMR90) and macrophage (J774A.1) cells in the presence of PEDOT nanomaterials, which was determined by the amount of ATP in the cells. IMR90 was incubated with PEDOT

nanomaterials for a) 24h and c) 48h; J774A.1 for b) 24h and d) 48h. Values exhibit mean ± SD and each experiment was performed in triplicate. *Statistically significant difference from control exposed to PEDOT nanomaterials ($P<0.05$).

Figure 44. Cytotoxicity of fibroblast (IMR90) and macrophage (J774A.1) cells in the presence of PEDOT nanomaterials, which was determined by the amount of LDH release. IMR90 was incubated with PEDOT nanomaterials for a) 24h and c) 48h; J774A.1 for b) 24h and d) 48h. Values exhibit mean ± SD and each experiment was performed in triplicate. *Statistically significant difference from control exposed to PEDOT nanomaterials ($P<0.05$).

Figure 45. Apoptosis and necrosis ratio obtained from annexin V and PI staining. IMR90 and J774A.1 were incubated with PEDOT nanomaterials (25 μg mL^{-1}) for 24 h. Each experiment was performed in triplicate. *Statistically significant difference from control exposed to PEDOT nanomaterials ($P<0.05$).

Figure 46. Live cell differential interference contrast (DIC) and fluorescent images of PEDOT nanomaterial treated IMR90/J774A.1 cells (25 μg mL^{-1}); negative control, PEDOT–1, PEDOT–2, and PEDOT–3. DIC images were taken at the same time corresponding to the cells. Green (aV) means

apoptosis, red (PI) means necrosis. Scale bars = 40 μm.

Figure 47. ROS production by a) IMR90; b) J774A.1 cells after incubation with PEDOT nanomaterials at 24 h. H_2O_2 (0.02%) was used as positive control. Values exhibit mean ± SD and each experiment was performed in triplicate. *Statistically significant difference from control exposed to PEDOT nanomaterials ($P<0.05$).

Figure 48. Gene expression of IL-1, IL-6, and TNF-α in J774A.1 macrophages incubated with culture medium containing PEDOT nanomaterials at 25 μg mL^{-1} for a) 6 and b) 24 h. Values exhibit mean ± SD and each experiment was performed in triplicate. *Statistically significant difference from control exposed to PEDOT nanomaterials ($P<0.05$).

Figure 49. SEM images of the PPy nanoparticles with different diameters (below: size distribution histograms determined by ELS). The average diameters are about (a) 20, (b) 40, (c) 60, (d) 80, and (e) 100 nm, respectively.

Figure 50. TEM images of the human lung fibroblast IMR90 cells incubated with 100 nm PPy nanoparticles for 24 h (25 μg mL^{-1}). (a) Overall IMR90 cell morphology (scale bar: 2 μm). (b-e) Higher magnification of the boxed area in (a) (scale bar: 500 nm). Red arrows indicate the PPy nanoparticles. (N, nucleus; mi, mitochondria; PM, plasma membrane)

Figure 51. TEM images of the mouse macrophage J774A.1 cells incubated with 100 nm PPy nanoparticles for 24 h (25 μg mL^{-1}). (a) Overall J774A.1 cell morphology (scale bar: 2 μm). (b-d) Higher magnification of the boxed area in (a) (scale bar: 500 nm). Red arrows and greed doted lines indicate the PPy nanoparticles and the protrusion of the plasma membrane for phagocytosis, respectively. (N: the nucleus, mi: the mitochondria, and PM: the plasma membrane)

Figure 52. TEM images of (a-e) the human lung fibroblast IMR90 and (f-j) the mouse macrophage J774A.1 cells incubated with different diameters of the PPy nanoparticles for 24 h (25 μg mL^{-1}). White arrows indicate the PPy nanoparticles.

Figure 53. Viability of (a) the IMR90 and (b) the J774A.1 cells in the presence of the PPy nanoparticles, which was determined by the amount of ATP in the viable cells. Viability was calculated relative to untreated cells (a negative control). Values exhibit mean ± SD and each experiment was performed in triplicate. *Statistically significant difference from the control exposed to the PPy nanoparticles ($P<0.05$).

Figure 54. ROS production by (a) the IMR90 and (b) the J774A.1 cells after being exposed to different diameter of the PPy nanoparticles for 24 h. Intercellular ROS were measured using a DCF-DA staining and H_2O_2 (0.7%)

was used as a positive control. Untreated cells were considered as a negative control. Values exhibit mean ± SD and each experiment was performed in triplicate. *Statistically significant difference from the negative control exposed to the PPy nanoparticles ($P<0.05$).

Figure 55. Expression of costimulatory markers (a) CD40, (b) CD80, and (c) CD86 on the J774A.1 cells incubated with 25 μg $mL^{-1}$of the PPy nanoparticles after 24 h. Treated cells were stained with FITC-conjugated antibodies and analyzed by flow cytometry. LPS (0.25 μg mL^{-1}) and FITC conjugated Rat IgG2a, κ isotype control antibody incubated cells were used as a positive control and an isotype control, respectively. Free of the PPy nanoparticles in the cells was considered as a negative control. Each experiment was carried out in triplicate. *Statistically significant difference from the negative control exposed to the PPy nanoparticles ($P<0.05$).

Figure 56. Apoptosis and necrosis ratio obtained by aV and PI double staining and measured by flow cytometry. (a) The IMR90 and (b) the J774A.1 cells were treated with the PPy nanoparticles for 24 h (25 μg mL^{-1}). Free of the PPy nanoparticles in the cells was used as a negative control. Each experiment was performed in triplicate.

Figure 57. Live cell differential interference contrast (DIC) and fluorescence images of the PPy-treated (a-e) IMR90 and (f-j) J774A.1 cell (25 μg mL^{-1}).

The cells were double stained with aV (green) and PI (red) for detection of apoptosis and necrosis. From up to the bottom, diameters of the PPy nanoparticles are (a, f) 20, (b, g) 40, (c, h) 60, (d, i) 80, and (e, j) 100 nm, respectively. DIC images were taken at the same time, corresponding to the fluorescence images. (Scale bars: 20 μm)

Figure 58. FE–SEM images of PANi nanomaterials with increasing aspect ratio: (a) PANi–1 (2.09), (b) PANi–2 (2.94), (c) PANi–3 (3.92), and (d) PANi–4 (5.35).

Figure 59. Cell viability obtained from luminescent assay for PANi nanomaterial treated human fibroblast cells determined by the amount of ATP in the cells; a) 24h, b) 48h incubation with PANI nanomaterials.

Figure 60. Cell viability obtained from CellTiter Blue assay for PANi nanomaterial treated human fibroblasts indicating metabolically active cells; a) 24h, b) 48h incubation with PANi nanomaterials.

Figure 61. Cell cytotoxicity of PANi nanomaterials on human fibroblast cells determined by the amount of LDH release; a) 24h and b) 48h incubation with PANi nanomaterials.

Figure 62. Live cell fluorescent and differential interference contrast (DIC) images of PANi nanomaterial treated IMR90 cells; a) positive control, b) PANi−1, c) PANi−2, d) PANi−3, e) PANi−4, and f) bulk. DIC images were

taken at the same time corresponding to the cells in panels a–f. Green (annexin V conjugated FITC) means apoptosis, red (PI) means necrosis. Scale bars approximately 20 μm.

Figure 63. Apoptosis and necrosis on IMR90 affected by (a)PANi–1, (b) PANi–2, (c) PANi–3, (d) PANi–4, and (e) bulk.

Figure 64. ROS production by IMR90 cell line after incubation with PANi nanomaterials at 24 h (25 μg/well); H_2O_2: 5 mM H_2O_2 as a positive control.

Contents

Chapter 1 Introduction

1.1 Background

1.1.1 Polymer nanomaterials

1.1.1.1 Synthesis and characteristics

The advance of electronic nanomaterials has been a rapidly developing field of research owing to the recognition that well-studied materials can represent new and sometimes fascinating properties at the nanoscale [1]. To date, nanomaterials have been devoloped from both fundamental and practical perspectives, and their unique chemical and physical characteristics have been continuously discovered. Among various synthesis methods of polymer nanomaterials, this study will describe two major synthetic methods: chemical oxidation polymerization and ultrasonic-induced emulsion polymerization.

Generally, major chemical polymerization of conducting polymers is the addition polymerization and differs from electrochemical polymerization in a basic mechanism [1-3]. For example of chemical oxidation polymerization

of pyrrole, in the initiation step, radical cations ($C_4NH_5^+$) are generated by the oxidation of pyrrole monomer. Figure 1 represents the possible chemical structure of polypyrrole (PPy) molecules during chemical oxidation polymerization. A radical-radical coupling between two radical cations forms a dimer with deprotonation, leading to a bipyrrole [4]. The bipyrrole is reoxidized and couples with other radical cations. This process is repeated consecutively during the propagation step. The termination occurs when nucleophilic water molecules or impurities attack in the polymer chains.

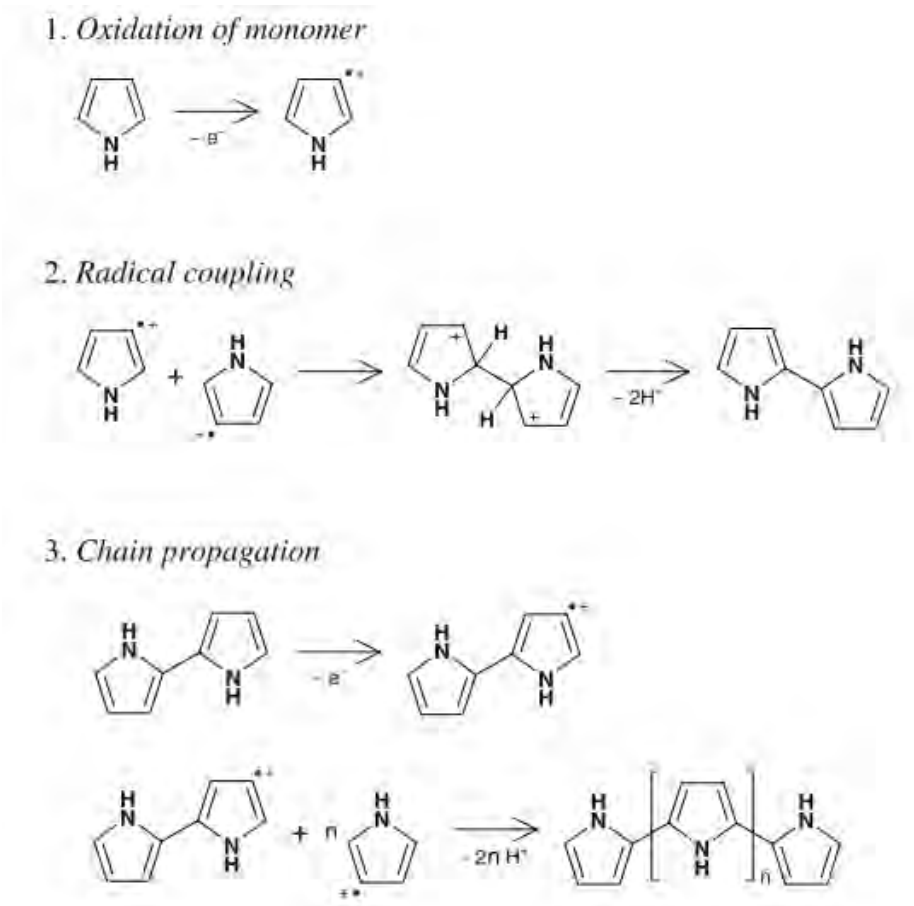

Figure 1. Possible mechanism of polymerization of pyrrole monomer.

To date, soft template synthesis, which involves the introduction of precursor materials within channels of templates, developed by Martin and modified by other groups [5-7] has been widely used to fabricate polymer nanomaterials. Recently, researchers have reported several alternative ways to produce polymer nanomaterials with tunable diameters. Among them, microemulsion polymerization has become an attractive methodology for fabricating polymer nanomaterials [8] because microemulsion provides advantages such as thermodynamic stability, the use of nanometer-sized micelles as nanoreactors, and a wide selection of surfactants (Figure 2) [9]. For example, polyacrylonitrile (PAN) nanomaterials have been fabricated using a salt-assisted microemulsion polymerization [10]. A salt was employed as the structure-directing agent and for coordination-complex formation with PAN nanoparticles during polymer nanomaterial formation. Considering this evidence, it was necessary to perform fundamental studies to investigate the fabrication of polymer nanomaterials by chemical oxidation polymerization and microemulsion polymerization.

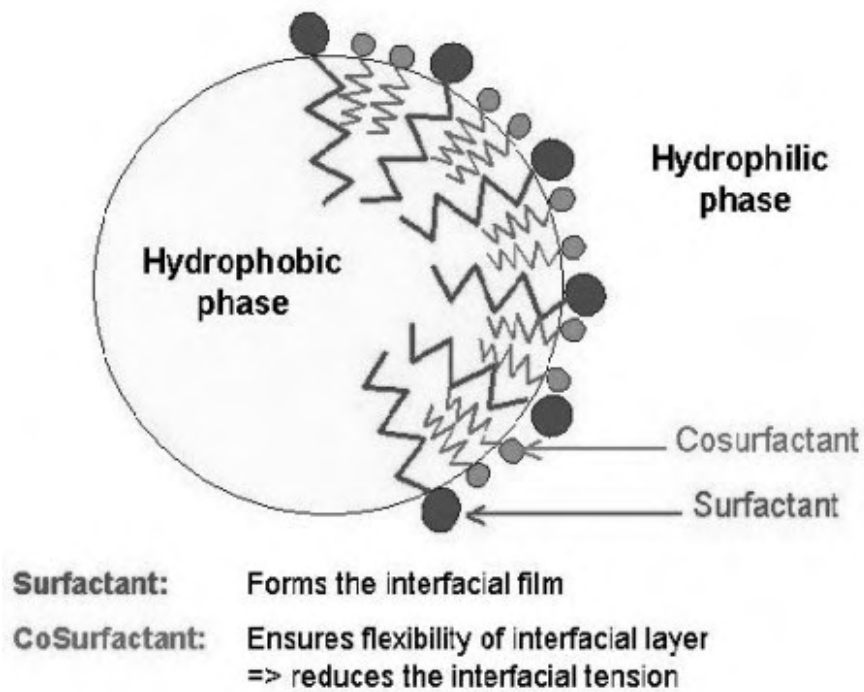

Figure 2. Expected diagram of microemulsion micelle in aqueous solution.

1.1.1.2 Their functionalities and applications

Polymer nanomaterials have received a great attention in various fields due to their functionality and biocompatibility [11]. However, there has been relatively little research on polymeric nanomaterials, in contrast to the inorganic counterparts [12]. Of a wide range of polymer materials, conducting polymers are of particular interest due to the electrical and optical properties that are similar to those of metals or inorganic semiconductors [13]. Conducting polymers have a variety of advantages such as facile synthesis, structural diversity and flexibility, light weight, and cost effectiveness. As a result, these materials are expected to be critical in the development of nanoscale devices. However, their usefulness extends far beyond the mere miniaturization of electronic components. These novel materials are a fascinating playground for scientists and engineers to explore the effects of low dimensionality on a material's physical properties.

Functionalized nanoparticles are of increasing interest in a variety of scientific fields such as cell biology, biotechnology, diagnostics, nanoanalytics, and pharmaceutics [14-16]. In polymer nanomaterials, diverse functional groups make them to get functionalities including fluorescence, targeting ligand, charge, sensing moiety, and enhancer of their physical

property. In medicine, for example, such functionalized particles find applications in sensing and diagnostics on the single-cell level [17]. Furthermore, recent progress of nanomaterials provides dual-functionality in therapy and diagnostic, called “theragnosis”.

1.1.2 Polymer nanomaterials as a detector

1.1.2.1 Imaging agents

Functional nanomaterials containing luminescence have been of great interest in bioscience such as bioimaging, drug carriers, and corresponding disease therapy [18]. Quantum dots (QDs) as an imaging probe represent unique optical properties such as wideband excitation, narrow emission, and high quantum yield [19]. However, these nanomaterials have intrinsic difficulties for bio-applications owing to complicated functionalization and potential cytotoxicity [20]. In addition, upconversion fluorescent nanoparticles have been attractive as emerging fluorescence biolabels [21]. These nanoparticles could exhibit near-infrared-to-visible upconversion luminescence via an anti-Stokes emission mechanism, resulting in reduced back ground noise and enhanced sensitivity owing to the absence of autofluorescence [22]. However, the use of rare earth metal could lead to toxicity through bio-accumulation and difficulties in functionalization. On the other hand, polymer nanoparticles have several advantages in bioimaging over inorganic based approaches, including diverse functionality, facile surface modification and low toxicity [23]. In general, the polymer nanoparticles for bioimaging have been mostly combined with the

fluorescent labels including fluorescent dyes or QDs [24]. The release of dyes with associated toxicity and ambiguity in imaging make it necessary to explore alternative strategies for the design of safer and brighter fluorescent nanoparticles.

1.1.2.2 Specific molecule detectors

Molecularly imprinted polymers (MIPs) as sensing materials have been widely investigated, but several limitations are also exposed [25]. When the density of imprinted site is low, the sensing process could be delayed due to slow diffusion of the analyte. Additionally, thick imprinted site could disrupt communication between the bound analyte and transducer on which the MIP is located. Recently, fluorescent boronic acid-based sensors have received considerable attention because of the formation of reversible covalent bonds [26]. Fluorescence transduction mechanisms include fluorescence resonance energy transfer (FRET), intramolecular charge transfer (ICT), and photo-induced electron transfer (PET) [27]. For example, boronic acid-based sensors are typically achieved using a PET sensing mechanism, in which the fluorophore acts as the electron acceptor and a conjugated N atom as the electron donor of the PET process [28].

1.1.3 Nanomaterials

1.1.3.1 Unique characteristics of nanomaterials

Over the past decades, nanomaterials have been of great interest in applications for biological fields such as drug delivery systems, biosensors, and bioimaging agents [29-31]. Nanomaterials including metal, ceramic, polymer, and composite define in the range of 1 – 100 nanometers (nm). The unit of nanometer derives its prefix nano form a Greek word meaning dwarf or extremely small. Considering that one nanometer contains 3 – 5 atoms in a row, surface atoms of nanomaterials are more exposed to environment than those of bulk materials. In particular, nanomaterials exhibit the quantum phenomena and atomic physics which are not observed in traditional bulk materials [32]. Nanomaterials with controlled sizes and shapes have the tremendous potential to make significant advances possible in medical science [33]. Compared with their bulky counterparts, nanomaterials often proved to show superior bioactivity by the exponential increase in surface-to-volume ratio with decreasing size of materials [34]. Furthermore, nanomaterials have fascinating physicochemical properties arising from size, shape, surface functionality, and composition [35].

Particle size and surface area are important material characteristics

from a toxicological perspective. As the size of a particle decreases, its surface area increases and also allows a greater proportion of its atoms or molecules to be displayed on the surface rather than the interior of the material. Figure 3 shows the inverse relationship between the particle size and the number of molecules expressed on the particle surface. As the particle size for airborne particles with fixed mass (10 mg m^{-3}) and unitary density (1 g cm^{-3}) decreases, their number increases exponentially along with the surface area. The increase in surface area determines the potential number of reactive groups on the particle surface.

By some estimates, nanotechnology promises to far exceed the impact of the Industrial Revolution and is projected to become $1 trillion market by 2015. Nanomaterials are already being used in sporting goods, tires, stain-resistant clothing, sunscreens, cosmetics, and electronics and will also be increasingly utilized in medicine for purposes of diagnosis, imaging, and drug delivery. The U.S. National Nanotechnology Institute envisages four generations of nanotechnology. The current era is that of passive nanostructures, materials designed to perform one task. The second phase will introduce active nanostructures for multitasking, for example, actuators, drug delivery devices, and sensors. The third generation is expected to emerge around 2010 and feature nanosystems with thousands of interacting

components. A few years after that, the first integrated nanosystems, functioning much like a mammalian cell with hierarchical systems within systems, are expected to evolve.

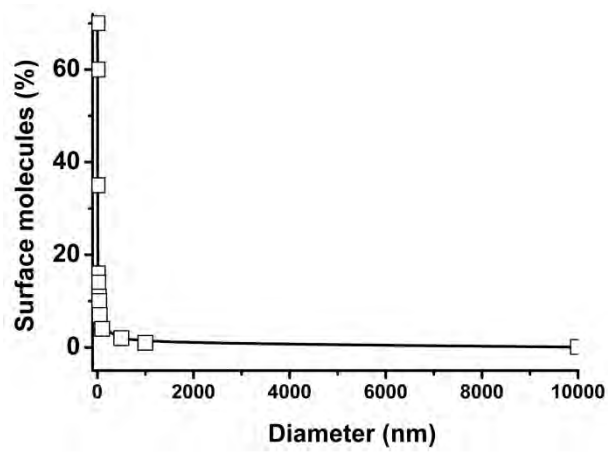

Figure 3. Inverse relationship between particle size and number of surface molecules. In the size range < 100 nm, the number of surface molecules (expressed as a % of the molecules in the particle) is inversely related to particle size.

1.1.3.2 Toxicity of nanomaterials

The unique physicochemical properties of nanomaterials may cause adverse effects to human organs [36-38]. The unusual physicochemical properties of nanomaterials are attributable to their small size (surface area and size distribution), shape, chemical composition (purity, crystallinity, electronic properties, etc.), surface structure (surface reactivity, surface groups, inorganic or organic coatings, etc.), solubility, and aggregation. Although impressive from a physicochemical viewpoint, the novel properties of nanomaterials raise concerns about adverse effects on biological systems, which at the cellular level include structural arrangements that resemble nanomaterials in terms of their function. Indeed, some studies suggest that nanomaterials are not inherently benign and that they affect biological behaviors at the cellular, subcellular, and protein levels [39,40]. Moreover, some nanoparticles readily travel throughout the body, deposit in target organs, penetrate cell membranes, lodge in mitochondria, and may trigger injurious responses (Figure 4).

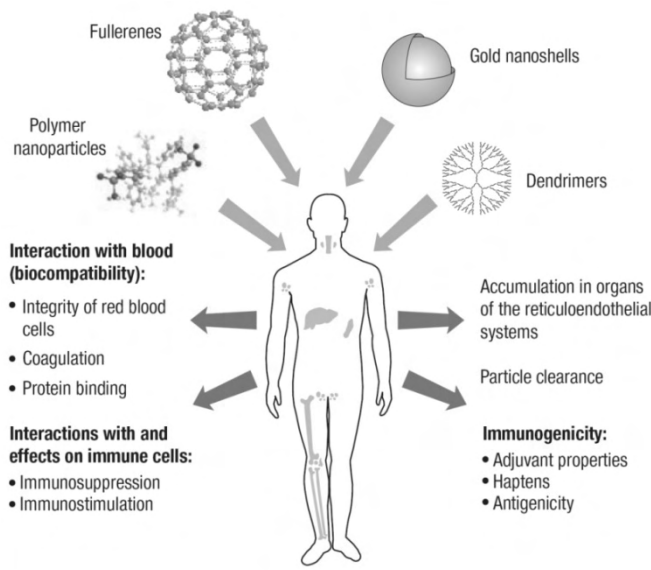

Figure 4. Possible effects on biological system of nanoparticles.

Nel et al. reported that the cellular response against nanomaterials was size-dependent, indicating that nanotoxicity was associated with endocytosis [41]. Additionally, the cytotoxicity and pro-inflammatory response of nanomaterials was previously shown to be size-, shape-, and surface functionality-dependent, indicating that the toxicity of nanomaterials was influenced by the interaction between the surface of the nanomaterials and cells [42]. Functional groups could induce harmful effect to biological systems mainly owing to their oxidative stress and inflammatory response [43]. For instance, electron capture on the surface of nanoparticles can lead to the formation of superoxide radical ($O_2^{\cdot-}$), resulting in generating additional reactive oxygen species due to Fenton chemistry and dismutation [44]. Nevertheless, there are the limited researches concerning size- and surface functionality-dependent nanotoxicity on biological systems.

The change in the physicochemical and structural properties of nanomaterials with a decrease in size could be responsible for a number of material interactions that could lead to toxicological effects [45]. For instance, shrinkage in size may create discontinuous crystal planes that increase the number of structural defects as well as disrupt the well-structured electronic configuration of the material, so as to give rise to altered electronic properties [46]. This could establish specific surface

groups that could function as reactive sites. The extent of these changes and their importance strongly depend on the chemical composition of the material. Surface groups can make nanomaterial hydrophilic or hydrophobic, lipophilic or lipophobic, or catalytically active or passive. An example of how those surface properties can lead to toxicity is the interaction of electron donor or acceptor active sites (chemically or physically activated) with molecular dioxygen (O_2). Electron capture can lead to the formation of the superoxide radical ($O_2^{\bullet -}$), which through dismutation or Fenton chemistry can generate additional ROS. Single-component materials as well the presence of transition metals on the surface can participate in the formation of such active sites. For instance, ultrafine particles contain transition metals (e.g., Fe and vanadium) and are also coated with redox-cycling organic chemicals (e.g., quinones), whereas carbon nanotubes contain metal impurities that can amplify chemical changes in the nanomaterial environment. Thus, several nanomaterial characteristics can culminate in ROS generation [47], which is currently the best-developed paradigm for nanoparticle toxicity. Other nanomaterial properties such as shape, aggregation, surface coating, and solubility may also affect the addressed specific physicochemical and transport properties, with the possibility of negating or amplifying the size effects (Figure 5).

The shape of nanomaterials has been considered for the optimal design of specific systems for biomedical applications [48]. The following three factors may be affected by the shape of nanomaterials: i) internalization rate at the cellular level, ii) strength of adhesion to cells, and iii) margination dynamics in blood vessel [49]. For example, it is known that ellipsoidal nanomaterials outperform spherical nanomaterials in terms of the adhesion and margination dynamics. Accordingly, the control of nanomaterial morphology is of great importance in biomedical field. However, to date, there have been only limited studies addressing the geometry-dependent toxicity of nanomaterials [50].

Nanomaterials can permeate into the human body via different routes. Since nanomaterials have great possibility to be airborne owing to their size, inhalation may be the major route of exposure of nanomaterials. From this point of view, the harmful effect of nanomaterials following inhalation is of key important in so-called nanotoxicology [51]. Alveolar macrophages protect the body *via* phagocytosis against nanomaterials entered though a respiratory route. As a result, *in vitro* toxicity investigation of lung fibroblast and alveolar macrophage cells could be helpful to understand pulmonary nanotoxicology such as cellular effect and uptake of nanomaterials.

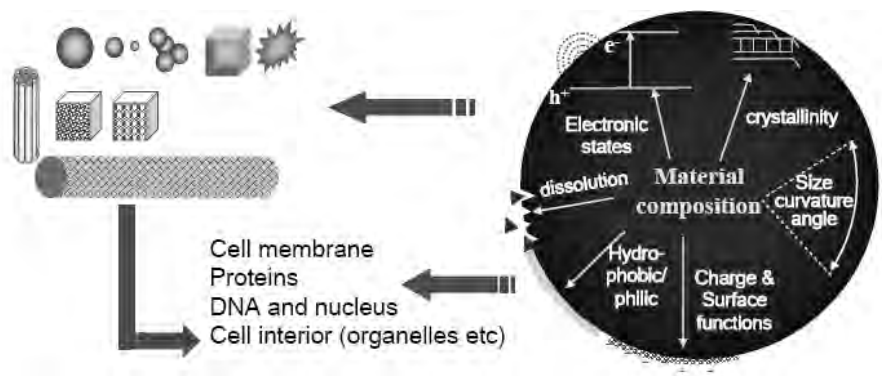

Figure 5. Elements of nanomaterials that can affect cellular system such as shapes, crystallinity, electronic states, dissolution, and charge or surface functionality.

1.2 Objectives and Outline of the study

1.2.1 Objectives

The aim of this dissertation provides fabricating functional polymer nanomaterials using chemical oxidation polymerization and emulsion templating polymerization, and evaluating their cytotoxicity and cellular effect. Additionally, the functional polymer nanomaterials applied for detection of specific molecules. In particular, conducting polymer nanomaterials including PPy, PANi, and PEDOT with controlled sizes and shapes are employed for nanotoxicological assessments. Furthermore, PAN nanoparticles with surface modification are applied for a cellular imaging agent, anthrax detector, and intracellular hydrogen peroxide detector.

1.2.2 Outline

This dissertation focuses on the fabrication of functional polymer nanomaterials and the investigation of their cellular effects and of specific molecule detections. In the viewpoint of abovementioned topics, this dissertation involves the following subtopics;

I. PAN nanoparticles for bioimaging

II. PAN nanoparticles for anthrax detection

IV. PAN nanoparticles for intracellular H_2O_2 detection

V. Cytotoxicity of PEDOT nanomaterials

VI. Cytotoxicity of PPy nanoparticles

VII. Cytotoxicity of PANi nanomaterials

A detailed outline of the study is as follows:

1. We report on the fabrication of novel photoluminescent (PL) PAN nanoparticle platforms and their application on in-vitro imaging of human breast cancer SK-BR-3 cell. The PAN nanoparticles with uniform diameter were produced by ultrasonic induced emulsion polymerization. The nanoparticles could possess PL properties and amine functional groups through ethylenediamine (EDA) treatment by vapor phase. After anchoring Anti-ErbB2 antibody on treated PAN, the polymer nanoparticles, for the first time, could be used as labeling agent to image human breast cancer SK-BR-3 cells without additional fluorophores.

2. Fluorescent polyacrylonitrile nanoparticles were synthesized by microemulsion polymerization and Schiff base modification. By further modification with europium, the polyacrylonitrile nanoparticles could be used as a highly sensitive and rapid sensor for *Bacillus anthracis* spore detection in aqueous solution. The europium-modified polyacrylonitrile nanoparticles were readily combined with dipicolinic acid as a unique biomarker of *B. anthracis*, leading to high fluorescence emission. These nanoparticles enabled ratiometric detection without instrument-specific calibration due to the internal fluorescence reference. Additionally, the europium-modified polyacrylonitrile nanoparticle sensors exhibited a remarkable limit of detection (10 pM) for dipicolinic acid and outstanding selectivity (160×) over aromatic ligands in aqueous solution. The ultrafine nanoparticle sensor showed a high capability for detecting anthrax due to the increased surface area-to-volume ratio and enhanced dispersibility.

4. Fluorescent boronate-modified polyacrylonitrile (BPAN) nanoparticles of 50 nm diameter were fabricated for use as a selective H_2O_2 sensor. The fluorescence intensity changed and an emission peak shifted when BPAN nanoparticles selectively interacted with H_2O_2, relative to other reactive

oxygen species (ROS). The BPAN nanoparticles undergo PET between a Schiff base moiety and boronate, which enhances the fluorescence and makes the nanoparticles suitable for selective ROS recognition. Moreover, the BPAN nanoparticles, after reaction with ROS, became an effective iron scavenger to inhibit the Fenton reaction. We demonstrate the use of these nanoparticles as a detector of endogenous H_2O_2 produced in living cells. The representative features of the fluorescent BPAN nanoparticles that make them particularly attractive for H_2O_2 and ROS detection are the following: they are easily synthesized as PET sensors; they exhibit a characteristic emission peak and peak shift that distinguishes reaction with H_2O_2 from other ROS; they act as a prochelator of metal ions; and compared to organic compounds, the sensing moiety on BPAN polymer nanoparticles are more thermally stabile and have superior mechanical properties, enabling their use in various biomedical applications.

5. PEDOT is recognized as one of the most promising conducting polymers to realize future applications in the fields of electronics, optics, energy storage/conversion systems, and biomedical science. Accordingly, the toxicity of PEDOT should be considered to hold the great potential for the widespread application. Herein, we report the cytotoxicity and

proinflammatory response of PEDOT nanomaterials of three different shapes are investigated toward human lung fibroblast (IMR90) and mouse alveolar macrophage (J774A.1) cells. The shape-dependent toxicity of the PEDOT nanomaterials is evaluated by examining cell morphological change, cytotoxicity, apoptosis/necrosis, oxidative stress, and immune response. Cytotoxicity and apoptosis of the PEDOT nanomaterials increase with decreasing aspect ratio of nanomaterials in both cell lines. The formation of reactive oxygen species in PEDOT nanomaterial treated cells is dependent on the shape and concentration of the nanomaterials. In addition, proinflammatory cytokines such as interleukin-1 (IL-1), interleukin-6 (IL-6), and tumor necrosis factor (TNF-α) from macrophages are induced by PEDOT nanomaterial treated cells.

6. Monodisperse PPy nanoparticles with five different diameters (20, 40, 60, 80, and 100 nm) were fabricated *via* chemical oxidation polymerization in order to evaluate size-dependent cytotoxicity. The cellular uptake of PPy nanoparticles in human lung fibroblasts (IMR90) and mouse alveolar macrophages (J774A.1) was observed by transmission electron microscopy. The nanoparticles were internalized into the IMR90 *via* endocytosis. In the J774A.1, the nanoparticles were entered *via* phagocytosis and endocytosis.

Endocytosed nanoparticles were transported *via* endosome-network and arrived in lysosomes. The cytotoxicity and innate immune response of PPy-treated cells were systematically investigated by viability assay, oxidative stress, apoptosis/necrosis, and expression of costimulatory molecules. The viability, oxidative stress, and apoptosis/necrosis of PPy-treated cells revealed size- and dose-dependency. Because of phagocytosis, PPy treatment had more adverse effects on J774A.1 than IMR90. Innate immune response of PPy-treated macrophages was measured by the expression of costimulatory molecules on surface of the cells. The expression of costimulatory molecules involved in Th1 response (CD40 and CD80) was lightly up-regulated and the other costimulatory molecule related in Th2 response (CD86) was less expressed than a negative control. These findings may provide better nanotoxicological information of polymer nanomaterials, and support the further development of PPy nanoparticles in bioelectronic applications.

7. The toxicity of PANi nanomaterials with four different aspect ratios on human lung fibroblast cells was investigated by cell viability assay, cytotoxicity assay, apoptosis/necrosis measurement, and reactive oxygen species production. The toxicity increased with decreasing aspect ratio of

PANi nanomaterials. In contrast, the highest aspect ratio PANi nanomaterials showed similar results with bulk PANi materials. The adverse effect of PANi nanomaterials was also concentration- and time-dependent. Low aspect ratio PANi nanomaterials induced more necrosis and more reactive oxygen species than others. These results provide new understanding of shape-dependent toxicity of nanomaterials.

Chapter 2 Experimental Details

2.1 PAN nanoparticles for bioimaging

2.1.1 Fabrication of PAN nanoparticles

Ultrasound (350 W) was introduced into the solution composed of 1.5 ml of acrylonitrile monomer, 0.5 g of sodium dodecylsulfacte and 20 ml of distilled water for 10 min. After adding 0.1 g of cerium sulphate and 0.025 g of nitroacetic acid into the solution, polymerization was performed for 10 min by aid of ultrasound irradiation. The solution was diluted by adding excess ethanol and 1 M of nitric acid (to remove cerium ions) and the precipitates were dried. The products (0.1 g) were loaded into the closed vessel including sealing apparatus. The vessel was evacuated until inner pressure reaches 10^{-2} torr, and heated to 70 ^{o}C. 0.1 ml of EDA was introduced and vapor phase treatment were performed for desired time. The residual monomer and EDA vapor was removed from the reactor by additional evacuation.

The tPAN nanoparticles (5 mg) were mixed with 0.1 M of PBS buffer solution (5 ml) and F127 as a dispersant (10 mg mL^{-1}), and exposed to ultrasound for 40 min to obtain uniform dispersion. The 1 mL of Anti-ErbB2 antibody (ab2428, Abcam Inc., MA) (10 μg mL^{-1}) was added into the above

solution, which had been previously incubated with EDC/NHS for 12 h [52]. The EDC/NHS conjugation method is very well-known procedure that connects carboxyl and amine group in biological experiments. EDC is a water-soluble derivative that catalyzes the formation of amide bonds between carboxylic acids and amines by activating carboxyl to form an O-urea derivative. This derivative reacts readily with nucleophiles. NHS is employed to activate carboxylic acids and amines toward amide formation, sometimes without EDC [53]. This reaction was extensively applied to couple covalently protein/enzyme molecules to self-assemble monolayers of thiolcarboxylic acids. After 2 hours reaction at 25 ^{o}C, the residual Anti-ErbB2 is removed by centrifugal force.

TEM images were obtained with a JEOL EM-2000 EX II microscope. SEM was performed with a JEOL 6330F at an acceleration voltage of 10 kV. A Bomem MB 100 FTIR spectrometer was used to characterize the PAN and tPAN nanoparticles. UV-vis spectrum of the tPAN nanoparticles was taken with a Perkin-Elmer Lambda-20 spectrometer. The Emission spectra of PAN and tPAN nanoparticles were obtained with a JASCO FP-6500 spectrofluorometer.

2.1.2 Application for bioimaging

Human breast cancer SK-BR-3 cell were obtained from ATCC. SKBR-3 were cultured in RPMI-1640 medium, with 10% fetal bovine serum, 1% penicillin- streptomycin solution, 300 mg L^{-1} of L-glutamine, 25 mM of sodium bicarbonate, and 25 mM of HEPES. Cells were incubated in a 5% CO_2 incubator at 37 ^{o}C and 100% humidity. Cells were placed in 75T flask and maintained between 1×10^5 and 1×10^6 cells mL^{-1} of medium. The medium was changed every 2-3 days or as required.

Cell viability was measured using CellTiter glow luminescent cell viability assay (Promega, Madison, WI). The assay is performed by estimating the number of viable cells in system, based on quantification of the ATP concentration. The single step procedure produces a luminescent signal, which is proportional to the quantification of ATP present in cells. This assay is depended on the alteration of beetle luciferin to oxyluciferin by a thermostable luciferase in the presence of ATP. The experiments were performed in 96-well plates. For the cell viability assay, 3000 cells per well were plated and treated with different concentrations of nanomaterials for 24 h.

Cells were seeded at a density of 2000 cells per well, in 8–well Lab–

Tek™ II Chambered Coverglass and treated with PAN nanomaterials (10 μg mL^{-1}). After incubation with PAN nanomaterials for 24 h, the plates were observed under a DeltaVision® RT imaging system with temperature (37^{o}C) and CO_2 (5%) control and photographed using a Cascade II EMCCD camera.

Polyethylene glycol-N-hydroxysuccinimide (PEG-NHS; Nanocs Inc., NY) was used for surface functionalization of the tPAN nanoparticles that could reduce the non-specific uptake on the cells due to the electrostatic attraction between positive charge of tPAN surface and negative charge of cell lipid layer. NHS is highly reactive compounds suitable for the modification of amino groups. NHS is the most common type of activated esters. The reaction of PEG-NHS with amines is conducted as manufacturer's instructions. Briefly, tPAN nanoparticles (10 mg) were mixed with 0.1 M of PBS (10 mL). Then, 4 mM of PEG-NHS in DMSO was added into the tPAN solution. After 3 h reaction at 25 ^{o}C, the product was washed thoroughly by 0.1 M PBS.

2.2 PAN nanoparticles for Anthrax detection

2.2.1 Fabrication of PAN nanoparticles

The following chemicals were purchased and used as received: 2,6-

pyridinedicarboxylic acid (Aldrich), 2,3-pyridinedicarboxylic acid (Aldrich), 2,5-pyridinedicarboxylic acid (Aldrich), 3,5-pyridinedicarboxylic acid (Aldrich), isophthalic acid (Aldrich), picolinic acid (Aldrich), benzoic acid (Aldrich), terephthalic acid (Aldrich), nicotinic acid (Aldrich), decyltrimethylammonium bromide (TCI Korea), acrylonitrile (Aldrich), ammonium persulfate (Aldrich), hydrogen chloride (Samchun Chemical), diethyl ether (Samchun Chemical), ammonia solution (Aldrich), ethyl alcohol (Samchun Chemical), glutaraldehyde (Aldrich), ethylenediamine (Aldrich), ethylenediamine tetraacetic acid dianhydride (Aldrich), europium chloride (Aldrich), terbium chloride (Aldrich), and 1 M phosphate buffer solution (Aldrich).

The PAN nanoparticles were prepared by micelle templating method. First, to synthesize PAN25 nanoparticles, decyltrimethylammonium bromide (DeTAB; 4.8 g) was dissolved in distilled water (40 mL). Acrylonitrile (AN; 0.28 g) was added dropwise into the DeTAB solution, and then APS (0.04 g) was added into the solution. The polymerization was carried out for 24 h. To synthesize PAN50 nanoparticles, DeTAB (2.4 g) was introduced into distilled water (20 mL). After inserting AN monomer (1.0 g), APS (0.052 g) was added into the solution. The microemulsion polymerization proceeded for 24 h. The resulting product was diluted by adding excess

ethanol, and subsequently the precipitates were dried in a vacuum oven at room temperature.

To synthesis Schiff base on the surface of PAN nanoparticles, Pinner synthesis was used. 0.5 g of PAN nanoparticles in ethanol (10 mL) were added into 1 M HCl in diethyl ether (20 mL) at 0 ^{o}C for 72 h in round-bottomed flasks under N_2 reflux. After the first step of Pinner modification, the product was washed with ethanol and precipitated. Then, the product was treated with ammonia solution (20 mL) under nitrogen purge for 3 h. The sample was washed with ethanol and precipitated for the next step. The amidine groups on the PAN nanoparticles were obtained by Pinner method. Then, the product was inserted into 1% glutaraldehyde solution to synthesize the Schiff base. The solution was diluted by distilled water and centrifuged. Schiff base-modified PAN (S-PAN) nanoparticles were dried in vacuum oven for the next experiments.

The S-PAN naoparticles (0.1 g) in 5 mL of distilled water were reacted with ethylenediamine (0.1 mL) for 2 h and washed with distilled water and centrifuged. Next, the product was reacted with ethylenediamine tetraacetic acid dianhydride (0.1 M; 1 mL) for 2 h. Subsequently, the product was redispersed in aqueous solution of $EuCl_3$ (0.1 M; 1 mL) by sonication and stirred for 3 h. The product (Eu-PAN) was centrifuged and washed with

distilled water. In the case of the terbium modification, $TbCl_3$ (0.1 M; 1 mL) was used instead of $EuCl_3$.

TEM images were obtained with a JEOL EM-2000 EX II microscope. SEM was performed with a JEOL 6330F at an acceleration voltage of 10 kV. A Bomem MB 100 FTIR spectrometer was used to characterize the PAN, S-PAN, and Eu-PAN nanoparticles. The emission spectra of S-PAN and Eu-PAN nanoparticles were obtained with a JASCO FP-6500 spectrofluorometer. XP analysis was performed to investigate the chemical composition of the surface-modified PAN nanoparticles using SIGMA PROBE (ThermoVG, UK) where the photon source was a microfocused monochromator source. The C 1s core level peak was taken as reference at 284.5 eV.

2.2.2 Application for Anthrax detection

PL quantum yield of S-PAN nanoparticles was determined by a comparision method of the fluorescence emission with the standard reference, DAPI (D1306, Molecular Probes Inc., OR), in aqueous solution. The PL quantum yield of S-PAN nanoparticles was calculated by following formula:

$$\Phi_P = \frac{F_P}{A_P} \times \frac{A_D}{F_D} \times \Phi_D$$

where Φ is the fluorescence quantum yield, F is the integrated fluorescence signal in the emission region, and A is the absorption coefficient at the excitation wavelength [54]. The term with a suffix P means the term for S-PAN nanoparticles and D indicates the term for DAPI.

Samples were prepared to a final volume of 3 mL in fluorescence quartz cuvettes and analyzed at 25 ^{o}C using a FP-6500 spectrofluorometer (JASCO). The optimal stoichiometry for complex formation with Ca-DPA was determined using Job's method of continuous variation. Ca-DPA solution was prepared by varying the concentration from 0 to 1000 nM. Eu-PAN and Tb-PAN nanoparticles were diluted to 1 μM, and these samples were excited at 270 nm (emission scan: 570 - 650 nm). The emission peaks at 581, 594, and 616 nm that were originated from $^{5}D_{0} \rightarrow {}^{7}F_{0}$, $^{7}F_{1}$, and $^{7}F_{2}$, respectively were scanned for sensing Ca-DPA. The limit of detection was determined using the background intensity plus three standard deviations.

2.3 PAN nanoparticles for intracellular H_2O_2 detection

2.3.1 Fabrication of PAN nanoparticles

The following chemicals were purchased and used as received: acrylonitrile (Aldrich), decyltrimethylammonium bromide (TCI Korea), ammonium persulfate (Aldrich), hydrogen chloride (Samchun Chemical), diethyl ether (Samchun Chemical), ammonia solution (Aldrich), ethyl alcohol (Samchun Chemical), glutaraldehyde (Aldrich), 1 M phosphate buffer solution (Aldrich), 2-aminopyridine-5-boronic acid pinacol ester (Aldrich), hydrogen peroxide (35 wt % solution in water; Aldrich), tert-butyl hydroperoxide solution (70 wt % in solution; Aldrich), sodium hypochlorite solution (Hanawa chemical pure), iron (III) chloride (Sigma-Aldrich), iron (II) chloride (Sigma-Aldrich), copper chloride (Aldrich), and zinc chloride (Sigma-Aldrich).

The PAN nanoparticles were prepared by microemulsion templating method. First, decyltrimethylammonium bromide (DeTAB; 2.4 g) was dissolved in distilled water (20 mL). Acrylonitrile (AN; 1 g) was added dropwise into the DeTAB solution, and then ammonium persulfate (APS; 0.052 g) was inserted into the solution. The microemulsion polymerization

proceeded at 70^{o}C for 24 h. The resulting product was diluted by adding excess ethanol, and subsequently the precipitates were dried in a vacuum oven at room temperature.

To graft boronate on the surface of PAN nanoparticles, Pinner synthesis was employed. 0.5 g of PAN nanoparticles in ethanol (10 mL) were added into 1 M HCl in diethyl ether (20 mL) at 0 ^{o}C for 72 h in flasks under N_2 reflux. Then, the product was washed with ethanol and precipitated. The product was treated with ammonia solution (20 mL) under nitrogen purge for 3 h. The product was washed with ethanol and precipitated for the next step. The product was inserted into 1% glutaraldehyde solution to synthesize the Schiff base. The solution was diluted by distilled water and centrifuged. Subsequently, the product was reacted with 2-aminopyrimidine-5-boronic acid pinacol ester (0.1 M; 2 mL) for 2 h. The resulting BPAN nanoparticles was washed with distilled water and centrifuged. (see Figure 6)

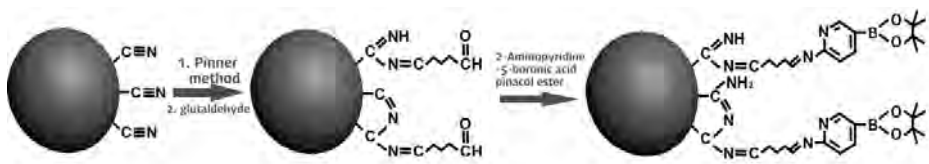

Figure 6. Schematic diagram of fabrication of BPAN nanoparticles.

Transmission electron microscope (TEM) images were obtained with a JEOL EM-2000 EX II microscope. Scanning electron microscope (SEM) was performed with a JEOL 6330F at an acceleration voltage of 10 kV. A Bomem MB 100 FT-IR spectrometer was used to characterize the PAN and BPAN nanoparticles. The emission spectra of BPAN nanoparticles were obtained with a JASCO FP-6500 spectrofluorometer. X-ray photoelectron (XP) analysis was performed to investigate the chemical composition of the PAN and BPAN nanoparticles using SIGMA PROBE (ThermoVG, UK) where the photon source was a microfocused monochromator source. The C 1s core level peak was taken as reference at 284.5 eV.

2.3.2 Application for intracellular H_2O_2 detection

The fluorescence intensity changes of PAN nanoparticles after Schiff base treatment were monitored at 424 nm (λ_{ex} = 360 nm). In the case of BPAN nanoparticles, the fluorescence was measured at λ_{ex} = 300, 320, 360 nm. A 0.1 M 4-(2-hydroxyethyl)-1-piperazinee-thanesulfonic acid (HEPES) buffer solution was employed in all experiments. The concentration of the nanoparticles was fixed at 10 μg mL^{-1}. Samples for absorption and emission measurements were contained in 1-cm × 1-cm quartz cuvettes (3.5-ml

volume, from Hellma). H_2O_2, TBHP, and OCl^- were diluted from 35, 70, and 5% aqueous solution, respectively. ·OH and ·OtBu were acquired by reaction of 1 mM Fe^{2+} with 100 μM H_2O_2 or 100 μM TBHP, respectively.

The rate of oxidation of BPAN to HPAN was determined under pseudo first-order conditions with excess H_2O_2 [55]. To a 3.0 mL solution of BPAN nanoparticles in 0.1 M PBS buffer at 10 μg mL^{-1} was added H_2O_2 to final concentrations of 20 μM, 40 μM, 60 μM, 80 μM, and 100 μM. Spectra were monitored over 0.5-5 min at room temperature with at least 30 spectra recorded. The change in absorbance at 360 nm was monitored. The negative slope of the linear fit of $\ln[(A-A_{HPAN})/(A_0-A_{HPAN})]$ vs time gives the rate constant k_{obs} (where A_{HPAN} is the absorbance of a 10 μg mL^{-1} sample of the HPAN and A_0 is the initial absorbance of BPAN, respectively). The rate of conversion (k ($M^{-1}S^{-1}$)) was determined from the slope of the line of k_{obs} vs. $[H_2O_2]$. The value of k was measured to be 3.59 $M^{-1}S^{-1}$ in accordance with Equation (1).

$$\text{Rate} = k[\text{BPAN}][H_2O_2] \quad (1)$$

ICP (JP/ICPS-7500, Shimdzu) measurement was used for quantifying metal ions removed by HPAN nanoparticles. The BPAN nanoparticles of 10 μg mL^{-1} in aqueous solution were treated with 50 μM H_2O_2 for 1 h. The

HPAN nanoparticles were washed and centrifuged. Metal ions such as Fe^{3+}, Cu^{2+}, and Zn^{2+} of three different concentrations were added in the HPAN solution and reacted for 5 min. After washing and collect supernatant, 48-51 wt % HF and 2 wt % HNO_3 with ultrasound were added to allow dissolution of metal ions. The mass of metal ions after reacting with HPAN nanoparticles was measured by ICP method.

Binding constant (K') of HPAN nanoparticles for Fe^{3+} and Cu^{2+} were measured spectrophotometrically by competition experiments with EDTA in PBS buffer at pH 7.4. The experiment establishes an exchange equilibrium (K_{ex}) between EDTA and HPAN for binding Fe^{3+} or Cu^{2+}, as shown in Eq. (2) in which M is denoted as either Fe^{3+} or Cu^{2+}. The equilibrium expression K_{ex} (Eq. (3)) comprises the individual equilibrium expressions for each ligand, defined in Eqs. (4) and (5). The values for K'_{CuEDTA} (15.81) and K'_{FeEDTA} (15.93) were calculated from the overall binding constants 18.7 and 25.0 respectively, adjusted for pH [56].

$$\text{M-EDTA} + \text{HPAN} \quad \overset{K_{ex}}{\rightleftharpoons} \quad \text{M-HPAN} + \text{EDTA} \qquad (2)$$

$$K_{ex} = \frac{[\text{EDTA}] \times [\text{M-HPAN}]}{[\text{HPAN}] \times [\text{M-EDTA}]} = \frac{K'_{\text{M-HPAN}}}{K'_{\text{M-EDTA}}} \qquad (3)$$

$$\text{M} + \text{EDTA} \quad \overset{K'_{\text{M-EDTA}}}{\rightleftharpoons} \quad \text{M-EDTA} \qquad (4)$$

$$M + HPAN \xrightleftharpoons{K'_{M\text{-}HPAN}} M\text{-}HPAN \qquad (5)$$

Solutions of EDTA (0.1 mM), $CuCl_2$ or $FeCl_3$ (0.05 mM) and HPAN (0-0.1 mM) were combined in 3 mL pH 7.4 0.1 M PBS buffer and allowed to equilibrate for at least 24 h. The excess of chelator-to-metal ensured that the metal ions remained coordinated at all times to prevent hydrolysis. After equilibration (as determined by the stabilization of the UV/Vis spectra), the absorbance at 355 nm due to the [Cu-HPAN] complex (or 341 nm for the [Fe-HPAN] complex) was recorded and converted to a concentration based on the respective extinction coefficient ([Cu-HPAN] ε_{355} = 1290 M^{-1} cm^{-1} and [Fe-HPAN] ε_{341} = 5230 M^{-1} cm^{-1}). Values for [EDTA], [HPAN] and [Cu-EDTA] were then determined from mass balance equations and a K_{ex} was calculated for each sample. Sixteen separate samples were prepared with varying concentrations of HPAN. The average K_{ex} value was then used to determine $K'_{Cu\text{-}HPAN}$ = 14.94 and $K'_{Fe\text{-}HPAN}$ = 20.23.

The apparent affinity of HPAN for Zn^{2+} at pH 7.4 was measured spectrophotometrically by a competition reaction between HPAN and PAR (4-(2-pyridylazo)resorcinol) in a method similar to that previously reported [56]. The exchange reaction and its equilibrium expression are shown in Eqs. (6) and (7), while the individual equilibria are shown in Eqs. (8) and (9),

where *K′* refers to the apparent binding constant under these conditions of buffer and pH. A solution of 100 μM PAR in 1 mL HEPES (10 mM HEPES, 100 mM NaCl, pH 7.4) was used as a background spectrum for the titration. To this solution was added 5 μM $ZnCl_2$ (2 μL of a 2.5 mM stock solution) and the absorbance spectrum from 200 to 800 nm was collected. To this solution were added 2 μM of HPAN (2 μL of a 1 mM solution) and the decrease in the absorbance at 350 nm was monitored until no further spectral changes were detected.

$$\text{M-PAR}_2 + \text{HPAN} \overset{K'_{ex}}{\rightleftharpoons} \text{M-HPAN} + 2\text{PAR} \qquad (6)$$

$$K_{ex} = \frac{[PAR]^2 \times [M\text{-}HPAN]}{[HPAN] \times [M\text{-}PAR_2]} = \frac{K'_{M\text{-}HPAN}}{K'_{M\text{-}PAR_2}} \qquad (7)$$

$$M + 2PAR \overset{K'_{M\text{-}PAR_2}}{\rightleftharpoons} \text{M-PAR}_2 \qquad (8)$$

$$M + HPAN \overset{K'_{M\text{-}HPAN}}{\rightleftharpoons} \text{M-HPAN} \qquad (9)$$

The concentration of [$M\text{-}PAR_2$] is obtained at each titration point from its extinction coefficient (ε=66000 M^{-1} cm^{-1}) and the concentrations of the

other components in Eq. (7) are calculated from mass balance equations. With K_{ex} in hand, and the known affinity of PAR (log K'=12.34) for zinc, the zinc binding constant ($K'_{M\text{-}HPAN}$) of HPAN is calculated according to Eq. (7). The average K_{ex} value was then used to determine $K'_{Zn\text{-}HPAN}$ = 7.13.

RAW 264.7 cells were cultured in Dulbecco's modified eagle medium (DMEM) with 10% fetal bovine serum, 1% penicillin-streptomycin solution, 4.5 g L^{-1} d-glucose, 300 mg L^{-1} l-glutamine, and 110 mg L^{-1} sodium pyruvate at 37°C in a 5% CO_2 atmosphere in 75–cm^2 flasks. The cells were subcultured three times per week. All experiments were performed in a clean atmosphere.

RAW 264.7 cells were spreaded at a density of 3000 cells per well, in 8–well Lab–Tek™ II Chambered Coverglass (Nunc, Thermo Fisher Scientific, USA) and treated with BPAN nanoparticles (5 and 10 μg mL^{-1}). After 24 h, the medium was removed and the cells were washed twice with 0.1 M PBS. Subsequently, the cells were treated with 1 μM PMA (Sigma) solution for 10 min at 37°C. The cells were analyzed with a Delta Vision® RT imaging system (Applied Precision, Issaquah, WA, USA) under 5% CO_2 at 37°C. To obtain images, a Cascade II electron multiplying charge-coupled device (EMCCD) camera was used.

RAW264.7 cells were plated in four-well plates at initial densities of

70,000 in 3 mL medium and grown for 24 h. PAN nanoparticles were surface-modified with fluorescein isothiocyanate (FITC) due to restriction of fluorescence lamp of flow cytometer. Fresh medium containing nanoparticles (10 μg mL^{-1} and 100 μg mL^{-1} PAN nanoparticles) was added to the cells and incubated for 24 h. All experiments were set up in triplicate. After the PAN nanoparticle incubation, cells were trypsinized and rinsed with 0.1 M PBS. For quantifying cells with the nanoparticels, cells were resuspended in 0.1 M PBS. Non-treated cells served as negative control; 10,000 cells were analyzed by using FACSAria flow cytometers using 488-nm laser excitation (Becton–Dickinson).

For cell viability test, Cell-Titer® glow luminescent cell viability assay (Promega, Madison, WI) was carried out as manufacturer's instruction. This assay is a homogeneous method to estimate the number of viable and metabollically active cells based on quantification of the ATP concentration. The luminescent intensity was detected after adding of the same amount of reagent to the medium. This luminescence was formed because of the transformation of beetle luciferin to oxyluciferin by luciferase in the presence of ATP in the cells. The assay was conducted in white opaque walled 96-well plates and the cells were seeded at a density of 3×10^3 cells per well. The cells were then incubated with different concentration of the

PAN and BPAN nanoparticles (50, 100, 200, and 250 μg mL^{-1}) for 24 h. After incubation, supernatant was removed and the cells were washed with 0.1 M PBS solution to remove residual nanoparticles. The luminescent signal was detected by Victor^3 Multilabel Readers at 595 nm emission.

The generation of superoxide radical and hydrogen peroxide was detected by DCF-DA staining. Without intracellular ROS, nonoxidized DCF-DA is nonfluorescent. In the prescence of ROS, it is converted to DCF highly fluorescent derivative. For ROS assay, 3×10^3 cells per well were cultured in white opaque 96-well plates and incubated with the PAN and BPAN nanoparticles (50, 100, 200, and 250 μg mL^{-1}) for 24 h. Then, the samples were washed with 0.1 M PBS solution and treated with 10 μM DCF-DA for 20 min at 37 °C. The cells were treated with hydrogen peroxide (0.02% H_2O_2) were used as positive control. Fluorescent intensity was detected by Victor^3 Multilabel Readers at an excitation wavelength of 485 nm and an emission wavelength of 535 nm.

2.5 Cytotoxicity of PEDOT nanomaterials

2.5.1 Fabrication of shape-controlled PEDOT nanomaterials

PEDOT nanomaterials of three different shapes were fabricated by chemical oxidation polymerization using sodium bis(2-ethylhexyl) sulfosuccinate (AOT) micelles as the soft template [57]. AOT was dissolved in hexane at a concentration of 3.4×10^{-1} M, and aqueous $FeCl_3$ solution (7 M) was added. The volume ratios of aqueous $FeCl_3$ solution to hexane were 1.1×10^{-2}, 1.6×10^{-2}, and 2.7×10^{-2} for the PEDOT-1, PEDOT-2, and PEDOT-3, respectively. All reactions were carried out at 20^{o}C. The resulting products were thoroughly washed with ethyl alcohol to remove residual reagents. TEM images were obtained with a JEOL EM-2000 EX II microscope. The surface charge (zeta potential) of PEDOT nanomaterials was measured by electrophoretic light scattering (ELS) with an ELS-8000 instrument (Otsuka Electronics, Japan).

2.5.2 Cytotoxicity of PEDOT nanomaterials

Human lung fibroblast IMR90 and mouse macrophage J774A.1 cell lines were obtained from American Type Culture Collection (ATCC, Manassas,

VA, USA). IMR90 cells were cultured in Eagle's minimum essential medium with glutamine (EMEM; ATCC, Manassas, VA, USA), supplemented with 10% fetal bovine serum, 1% penicillin–streptomycin solution, 1mM sodium pyruvate, 2mM L-glutamine, and 1500 mg L^{-1} sodium bicarbonate. J774A.1 cells were maintained in RPMI-1640 medium, with 10% fetal bovine serum, 1% penicillin–streptomycin solution, 300 mg L^{-1} L-glutamine, 25 mM sodium bicarbonate, and 25 mM 4-(2-hydroxyethyl)-1-piperazineethanesulfonic acid (HEPES). Cells were incubated in a 5% CO_2 incubator at 37 ^{o}C and 100% humidity. The cells were placed in a 75T flask and maintained at between 1×10^5 and 1×10^6 cells mL^{-1} of medium. The medium was changed every 5–6 days for IMR90 and 2–3 days for J774A.1 or as required.

All experiments were performed in a clean atmosphere to prevent endotoxin contamination, which might interfere with the toxicity of the PEDOT nanomaterials. Stock solutions of PEDOT nanomaterials (10 mg mL^{-1}) were prepared in 0.1 M phosphate-buffered saline (PBS) and diluted to the required concentrations (10, 25, 100, 250, and 500mg mL^{-1}). After incubation with PEDOT nanomaterial for 24 h, the plates were observed with a DeltaVision RT imaging system (Applied Precision, Issaquah, WA) under CO_2 (5%) control atmosphere at 37^{o}C and the sample images were

recorded using a Cascade II electronmultiplying charge-coupled device (EMCCD) camera.

Cell viability was measured using the CellTiter glow luminescent cell viability assay (Promega, Madison, WI, USA). The assay is a homogeneous technique for estimating the number of viable cells in a culture based on quantification of the ATP concentration. The single-step procedure detects a luminescence signal proportional to the amount of ATP present in the cells. This assay relies on the alteration of beetle luciferin to oxyluciferin by a thermostable luciferase in the presence of ATP. The experiments were performed in black, opaque-walled 96-well plates. For the cell viability assay, 3000 cells per well were plated and treated with different concentrations of nanomaterials (10, 25, 100, 250, and 500 mg mL^{-1}) for 24 and 48 h. The cells were analyzed using Victor3 Multilabel Readers (Perkin–Elmer, Waltham, MA, USA) at an emission wavelength of 595 nm.

Lactate dehydrogenase (LDH), which changes lactate to pyruvate, is an enzyme widely existing in cytosol. The LDH release level into a medium is proportional to the disrupted or changed plasma membrane integrity and increases depending on the material/chemical toxicity. Thus, higher LDH values in the medium indicate higher cytotoxicity levels. The CytoTox-ONE homogeneous membrane integrity assay (Promega, Madison, WI) involves

the fluorescence measurement of the release of LDH from cells with a damaged membrane. Cells were seeded at a density of 3000 cells per well in black, opaque-walled 96-well plates and treated with PEDOT nanomaterials as described for the cell viability assay. A time-dependent experiment was conducted that employed different incubation periods (24 and 48 h) after nanomaterial insertion. The cells were analyzed using Victor3 Multilabel Readers at an emission wavelength of 595 nm.

Propidium iodide (PI) and annexin V (aV) staining was conducted to differentiate apoptosis from necrosis induced by PEDOT nanomaterials. The aV assay provides a simple and effective method to detect apoptosis at a very early stage. It takes advantage of the fact that PS is translocated from the inner (cytoplasm) side of the plasma membrane to the outer (cell surface) side soon after the induction of apoptosis. PS on the outer side is able to bind aV, thus providing a simple staining assay. On the other hand, PI, which monitors plasma membrane integrity, provides the detection of necrotic cells. aV has a high affinity for translocated PS from the inner to the outer leaflet of the plasma membrane in apoptotic cells. aV conjugated to AlexaFluor 488 (Vybrant apoptosis assay kit, Molecular Probes, Invitrogen, Grand Island, NY) facilitates observation by an image restoration microscope. PI stains dead cells with red fluorescence, binding to the nucleic acids in the cells.

Cells were seeded at a density of 3000 cells per well in an eight-well Lab-Tek II chambered cover glass (Nunc, Thermo Fisher Scientific, USA) and treated with PEDOT nanomaterials (25 mg mL^{-1}). After 24 h of incubation, aV and PI staining were carried out as per manufacturer's instructions. Live cell images were obtained by a DeltaVision RT imaging system with temperature (37 ^{o}C) and CO_2 (5%) control. To acquire apoptosis and necrosis cell images, a 40× oil immersion objective was employed with a Cascade II EMCCD camera. aV was excited with a 488 nm laser line and PI was excited by a 543 nm laser line. Apoptosis and necrosis quantification was carried out by aV and PI staining followed by flow cytometric measurement of the fluorescence. Approximately 1×10^5 cells were seeded in six-well plates (Falcon, USA). After PEDOT nanomaterial treatment (25 mg mL^{-1}) for 24 h, the medium was aspirated and cells were washed twice. The cells were collected and centrifuged, then rinsed with HEPES buffer (Sigma–Aldrich, USA) and resuspended in HEPES at a concentration of 1×10^6 cells mL^{-1}. The staining was carried out as per manufacturer's instructions. Flow cytometry analysis was performed using a FACSCalibur system (Becton Dickinson, USA) at an emission wavelength of 530 nm for aV and 585 nm for PI.

The generation of hydrogen peroxide was detected by using 2′,7′-

dichlorodihydrofluorescein diacetate (DCF-DA; Invitrogen, Grand Island, NY) staining. In the presence of H_2O_2 and hydroxyl radicals, DCF-DA is converted to a highly fluorescent derivative, DCF. Shape-dependent measurements of the generation of ROS were prepared by incubating 3000 cells with PEDOT nanomaterials (10, 25, 100, 250, and 500 mg mL^{-1}) for 24 h in a 96-well plate, followed by addition of DCF-DA (10 mm) for 20 min at 37 ^{o}C. H_2O_2 (0.02%) was used as positive control. The cells were analyzed by Victor3 Multilabel Readers at an emission wavelength of 535 nm.

PEDOT nanomaterial (25 $mgmL^{-1}$)-treated cells (1×10^6 cells) were collected after 6 and 24 h of treatment and the total RNA was extracted by disrupting the cells in Trizol reagent (1.0 mL; Invitrogen, Carlsbad, CA, USA) after gentle shaking for 10 min. Chloroform (0.2 mL) was mixed in each tube at room temperature for 10 min and the tubes were centrifuged at 12 000 g and 4 ^{o}C for 15 min. The aqueous phase was transferred to a new tube along with isopropanol (0.5 mL) and incubated for 10 min, then centrifuged at 12 000 g and 4 ^{o}C for 20 min. The supernatant was removed and the pellet was washed with cold 75% ethanol/diethyl pyrocarbonate (DEPC) solution (1 mL). The pellet was centrifuged and dried for 10 min. The extracted RNA with 40 times dilution in DEPC/water was measured by UV/Vis spectrometry at 260 and 280 nm. The extracted RNA was

subsequently reverse-transcribed to complementary (cDNA) according to the manufacturer's instructions. Briefly, cDNA synthesis and amplification were performed using the SuperScript First-Strand Synthesis System for real-time PCR (Invitrogen, Carlsbad, CA, USA) as given in the supplier's instructions. Each sample for real-time PCR analysis contained 100 ng cDNA, SYBR Premix Ex Taq (Takara, Shiga, Japan), and 0.2 mM of each custom primer; b-actin was used as the reference housekeeping gene. The cDNA was used for real-time PCR analysis for the expression of TNF-a, IL-1, and IL-6 genes. The reactions were performed using the primer pairs: 5'-CGA GTG ACA AGC CTG TAG CC-3' and 5'-TTG AAG AGA ACC TGG GAG TAG AC-3' for TNF-α, 5'-CCC AAG CAA TAC CCA AAG AAG AAG-3' and 5'-TGT CCT GAC CAC TGT TGT TTC C-3' for IL-1, 5'-TTC CAT CCA GTT GCC TTC TTG-3' and 5'-TCA TTT CCA CGA TTT CCC AGA G-3' for IL-6, and 5'-TCC TGT GGC ATC CAC GAA ACT-3' and 5'-GGA GCA ATG ATC CTG ATC TTC-3' for β-actin. PCR amplification and real-time fluorescence detection were performed with an ABI PRISM 7000 sequence detection system (Applied Biosytems Inc, Foster City, CA, USA). The cDNA was denatured at 95 ^{o}C for 10 s. This was followed by amplification of the target DNA through 40 cycles of denaturation at 95 ^{o}C for 5 s and elongation at 60 ^{o}C for 30 s. The level of expression was calculated and normalized to β-actin.

Measured values were expressed as mean-standard deviation. Data in the above assays were analyzed by means of one-way analysis of variance (ANOVA) with a Duncan's test for the multiple comparisons. $p<0.05$ is considered as statistically significant.

2.5 Cytotoxicity of PPy nanoparticles

2.5.1 Fabrication of size-controlled nanoparticles

Poly(vinyl alcohol) (PVA; Mw: 9000) and ferric chloride ($FeCl_3$, 97%) were purchased from Aldrich Chemical Co. and used without further purification. Pyrrole (98%) monomer was also obtained from Aldrich Chemical Co. and used as received. PPy nanoparticles with different diameters could be prepared by water-soluble polymer/metal cation system, which was previously reported [58]. Briefly, PPy nanoparticles were fabricated using PVA/$FeCl_3$ and pyrrole monomer in aqueous solution. The fabrication of PPy nanoparticles consists of several stages. At first step, a variable amount of PVA was dissolved in distilled water at room temperature and magnetically stirred. The concentration of aq. PVA solution varied in the range of 1.25-7.50 wt% relative to the amount of water. After first step,

$FeCl_3$ was added into the aq. PVA solution. The molar ratio of $FeCl_3$ to pyrrole monomer was fixed ([$FeCl_3$]/[pyrrole]: 2.3). The water-soluble polymer/metal cation system evolved from a limpid state to a viscous orange state in appearance. After a few minutes to allow equilibration, pyrrole monomer was introduced into the PVA/$FeCl_3$ solution. The concentration of pyrrole monomer ranged from 0.1 to 1.0 M. Under our experimental conditions, the concentration of water-soluble polymer and pyrrole monomer was used as main factors for determining the diameter of PPy nanoparticles. Specifically, the PPy nanoparticles with different diameters could be acquired by following experimental conditions ([pyrrole]- PVA wt%): 0.1 M-7.50 wt%, 0.2 M-7.50 wt%, 0.8 M-7.50 wt%, 1.0 M-5.00 wt%, and 1.0 M-1.25 wt% based water-soluble polymer/metal cation system, and each PPy nanoparticles diameter was *ca*. 20, 40, 60, 80 and 100 nm, respectively. A polymerization proceeds immediately when a monomer contacts the oxidizing agents. The solution turned black within few minutes and was stirred for at least 3 h. After the polymerization, the resulting PPy nanoparticles were separated from the dispersion solution by centrifugation and washed several times with water to remove impurities.

2.6.2 Cellular uptake of PPy nanoparticles

Two cell lines, IMR90 and J774A.1, were purchased from ATCC. IMR90 cells were maintained in EMEM, containing 10% fetal bovine serum, 1% penicillin/streptomycin solution, 1 mM sodium pyruvate, 2 mM L-glutamine, and 1500 mg L^{-1} sodium bicarbonate. J774A.1 cells were cultured in RPMI-1640 medium, with 300 mg L^{-1} L-glutamine, 10% fetal bovine serum, 1% penicillin/streptomycin solution, 25 mM sodium bicarbonate, and 25 mM HEPES. The cells were cultured in a humidity controlled incubator at 37 ^{o}C with 5% CO_2. The cells were placed in 75T flask and culture media were changed once a week for IMR90 and three times a week for J774A.1.

The morphology of the cells incubated with the PPy nanoparticles was observed by TEM. Cells (2×10^4 cells mL^{-1}) were cultured in sterile culture dishes (Nunc, Thermo Fisher Scientific, USA) for 24 h, and PPy nanoparticles (25 mg mL^{-1}) were added for another 24 h. After incubation, cells werewashed with 0.1 M PBS, trypsinized with 0.25% Trypsin-EDTA (Gibco, USA), and collected in eppendorf tubes. Then, they were prefixed with modified Karnovsky's fixative (mixed with 2% paraformaldehyde and 2% glutaraldehyde in 0.05 M PBS buffer) at 4 ^{o}C for 2 h. After being washed three times with 0.1 M PBS, cells were postfixed with 1% osmium

tetraoxide at 4 ^{o}C for 2 h and stained with 0.5% uranyl acetate at 4 ^{o}C for overnight. Dehydration was conducted through a graded series of 30, 50, 70, 80, 90, and 100% ethanol and propylene oxide before embedding in spurr's resin. Resin blocks were hardened at 70 ^{o}C for 1 day and sectioned by ultramicrotomy. The sections were stained with 2% uranyl acetate and Raynolds' lead citrate and analysis was done using TEM.

2.5.3 Cytotoxicity and innate immune response of PPy nanoparticles

The viability of the PPy nanoparticles treated cells was measured using Cell-Titer-glow luminescent cell viability assay. This assay is a homogeneous method of estimating the number of viable cells based on amount of ATP in metabolically active cells. The luminescent signal is generated when the beetle luciferin is transformed into oxyluciferin by a recombinant luciferase in the presence of ATP. For the assay, cells were seeded at a density of 1.5×10^4 cells mL^{-1} in black opaque 96-well plates and treated with different concentrations of the PPy nanoparticles (10, 25, 100, 250, and 500 mg mL^{-1}) for 24 h. After incubation, supernatant was removed and following steps were carried out as supplier's instructions. Cell viability

was detected by Victor3 Multilabel Readers.

The intercellular production of hydrogen peroxide was monitored by using DCF-DA staining. Non-fluorescent DCF-DA is converted to DCF, highly fluorescent derivative, in the presence of ROS. 3000 cells per well were plated in black opaque 96-well plates and incubated with the PPy nanoparticles (10, 25, 100, 250, and 500 mg mL^{-1}) for 24 h. After that, these were treated with 10 mM DCF-DA for 20 min at 37 ^{o}C. Hydrogen peroxide (0.7% H_2O_2) treated cells were used as a positive control. ROS was detected by Victor3 Multilabel Readers at an excitation wavelength of 485 nm and an emission wavelength of 535 nm.

25 mg mL^{-1} of the PPy nanoparticles treated J774A.1 macrophage cells (1×10^5 cells) were washed with ice cold FACS buffer (0.1 M PBS, 0.5% BSA, and 0.05% 1 M NaN_3) and blocked for 30 min at 4 ^{o}C in blocking solution (0.1 M PBS,10% FBS, and 0.03% 1 M NaN_3). Cells were then stained with FITC-conjugated mouse monoclonal antibodies (CD40, CD80, and CD86) and Rat IgG2a, κ isotype control antibody (all purchased from BioLegend, San Diego, CA, USA). Cells were washed with ice cold FACS buffer, suspended in FACS buffer, and fixed with 2% paraformaldehyde. They are analyzed with FACSCalibur-flow cytometry and WinMDI 2.9 software.

For apoptosis detection, Alexa Fluor-488 conjugated aV and PI staining was used. Apoptosis and necrosis quantification were carried out by flow cytometric measurement of the fluorescence. 1×10^5 cells were incubated in sterile culture dishes for 24 h and 25 mg mL^{-1}. PPy nanoparticles were added for another 24 h. Then, cells were washed with 0.1 M PBS, trypsinized, and collected in FACS analysis tubes. Thereafter, the aV and PI staining were performed as supplier's instruction. Flow cytometric analyses were recorded using FACSCalibur-flow cytometry at an emission wavelength of 530 nm for aV and 585 nm for PI. 10,000 cells were counted per sample. Each experiment was performed in triplicate. Data were analyzed using WinMDI 2.9 software.

Apoptosis and necrosis were visualized by aV and PI staining. Cells were seeded at a density of 3000 cells per well, in 8-well Lab-Tek II Chambered Coverglass (Nunc, Thermo Fisher Scientific, USA) for 24 h. After 24 h of incubation, the PPy nanoparticles (10 mg mL^{-1}) were applied for another 24 h. The medium was removed and the cells were washed twice with 0.1 M PBS. The aV and PI double staining was conducted as manufacturer's instructions. Live cell images were obtained by Delta Vision-RT imaging system under CO_2 control (5%) at 37 ^oC. To obtain apoptosis and necrosis cell images, Cascade II EMCCD camera was used.

2.6 Cytotoxicity of PANi nanoparticles

2.6.1 Fabrication of PANi nanoparticles

All experiments were conducted in a clean atmosphere to remove the chances of endotoxin contamination which might interfere with the toxicity of the PANi nanomaterials. All used chemicals were of analytical grade. Aniline was distilled twice under vacuum before used. Aniline (Sigma-Aldrich, 2.7×10^{-2} mol) was introduced dropwise in 0.5 M aqueous HCl solution (70 mL) with stirring for 1 h. The polymerization proceeded using ammonium persulfate (APS, Sigma-Aldrich, 50 mL, 1.3×10^{-2} mol) employed at 25 ^{o}C as an oxidant at room temperature for 2 h, and then, the resulting product was washed more than 5 times with excess ethyl alcohol to eliminate the residual HCl and aniline. After drying in vacuum oven at 45 ^{o}C for 24 h, the resulting PANi nanomaterials were prepared for further investigations.

Aspect ratios of PANi nanomaterials were controlled by the weight ratio of poly(vinyl pyrrolidone) (PVP, Sigma-Aldrich, Mw:40,000)/aniline. PVP as a steric stabilizer was introduced in 70 mL of deionized water, followed by above–mentioned polymerized procedure. As PVP/aniline ratio was

changed from 0 to 1.6 (1.6: PANi–4, 1.2: PANi–3, 0.8: PANi–2, 0: PANi–1, respectively), the aspect ratio decreased from 5.35 to 2.09 (Table 1). In the case of bulk, as a control, the polymerization of aniline proceeded with vigorous stirring using APS without HCl and PVP.

The morphology of the synthesized PANi nanomaterials was observed by field emission scanning electron microscopy (FE–SEM, JEOL 6330F at an acceleration voltage of 10 kV). The surface charge (zeta potential) of PANI nanomaterials were measured by ELS–8000 (Otsuka Electronics, Japan) utilizing an electrophoretic light scattering (ELS). The nanomaterials were dispersed in aqueous solutions at a concentration of 25 μg mL^{-1}, and then sonicated for 3 min before measuring zeta potential. The conductivities of the nanomaterials were determined on pressed pellets (13 mm in diameter and 0.2 mm in thickness) at room temperature by a four probe method using a Kiethley 2400 sourcemeter.

2.6.2 Cytotoxicity of PANi nanoparticles

IMR90 cell lines were obtained from American Type Culture Collection (ATCC, USA). Normal human lung fibroblasts (IMR90, at passage 16–22) were maintained in eagles minimum essential medium with glutamine

(EMEM, ATCC, USA) supplemented with 10% FBS and 1% penicillin streptomycin. Cells were incubated in a 5% CO_2 incubator at 37^{o}C. Stock solutions of PANi nanomaterials (10 mg mL^{-1}) were prepared in sterile distilled water and diluted to the required concentrations using the cell culture medium.

The cell viability of PANi nanomaterial treated cells was measured using CellTiter glow luminescent cell viability assay (Promega, Madison, WI). The ATP assay is a homogeneous technique for estimating the number of viable cells in a culture based on quantification of the ATP concentration. The single step procedure generates a luminescent signal proportional to the quantification of ATP present in cells. This assay relies on the alteration of beetle luciferin to oxyluciferin by a thermostable luciferase in the presence of ATP. The experiments were performed in 96–well plates. Additional controls were included in the test to rule out autoluminescence and quenching by PANI nanomaterials. For the ATP assay, 3000 cells per well were plated and treated with different concentrations of nanomaterials (10, 25, 100, 250, and 500 μg mL^{-1}) for 24 and 48 h.

CellTiter blue cell viability assay (Promega, Madison, WI) is a fluorimetric method for determining the metabolically active cells in a culture. The mitochondrial and microsomal enzymes in the viable cells

reduce resazurin into resorufin, generating a fluorescent signal. Resorufin emits fluorescence at 584 nm, which is proportion to the number of viable cells. Cells were seeded at a density of 3000 cells per well, in black opaque walled 96–well plates and treated with PANi nanomaterials as described for ATP assay. A time–dependent experiment was conducted employing different incubation period (24 and 48 h) after PANi nanomaterial insertion. The experiments were carried out as supplier's instructions.

LDH that changes lactate to pyruvate is an enzyme widely existing in cytosol. Disrupted or changed plasma membrane integrity causes LDH leakage into media and released LDH level increases depending on the material/chemical toxicity. Thus, higher LDH values in the medium suggest higher cytotoxicity levels. LDH assay (Promega, Madison, WI) is a fluorescent measurement of the release of LDH from cells with a damaged membrane. Cells were seeded at a density of 3000 cells per well, in black opaque walled 96–well plastes and treated with PANi nanomaterials as described for ATP assay. A time–dependent experiment was conducted employing different incubation period (24 and 48 h) after nanomaterial insertion. The LDH assay was carried out as supplier's instructions.

Use of aV and PI staining was conducted to differentiate apoptosis from necrosis induced by PANi nanomaterials. The aV has a high affinity for

translocated phosphotidylserine from the inner to the outer leaflet of the plasma membrane in apoptotic cells. The aV conjugated to fluorescein (FITC) facilitates observation by an image restoration microscope. PI stains dead cells with red fluorescent, binding to the nucleic acids in the cells. Cells were seeded at a density of 3000 cells per well, in 8–well Lab–Tek™ II Chambered Coverglass and treated with PANi nanomaterials (25 μg). After 24h incubation, the aV and PI staining were carried out as per manufacturer's instructions. Live cell imaging were obtained by DeltaVision® RT imaging system with temperature ($37^{o}C$) and CO_2 (5%) control. To acquire apoptosis and necrosis cell images, 40× oil immersion objective was employed with Cascade II EMCCD camera. FITC was excited with a 488 nm laser line and PI was excited by a 543 nm laser line.

Apoptosis and necrosis measurement was carried out by aV and PI staining followed by flow cytometric measurement of the fluorescence. Approximately 1×10^{5} cells were seeded in 6–well plate. After 25 μg PANi nanomaterial treatments for 24 h, the medium was aspirated and cells were washed twice in 0.1 M PBS. Cells were trypsinized and centrifuged. After stopping trypsin with full–EMEM, the cells were rinsed with HEPES buffer (Sigma–Aldrich, USA) and resuspended in HEPES at the concentration 1×10^{6} cells mL^{-1}. The staining was carried out as per manufacturer's

instructions. Flow cytometry analysis was performed using FACSCalibur (Becton Dickinson, USA) at an emission wavelength of 530 nm for annexin–V conjugated FITC and 585 nm for PI.

The generation of hydrogen peroxide was detected by using 2',7'–dichlorodihydrofluorescein diacetate (DCF–DA, invitrogen, Grand Island, NY) staining. In the presence of a H_2O_2 and hydroxyl radicals, DCF-DA is converted to a highly fluorescent derivative, 2',7'–dichlorodihydrofluorescein (DCF). Shape–dependent measurements of the generation of ROS were prepared by incubating 3000 cells with PANI nanomaterials (25 μg) for 3 h in 96–well plate, followed by adding with 10 μM DCF–DA for 20 min at 37^{o}C. Hydrogen peroxide treated cells (5 mM H_2O_2) were employed as a positive control for ROS analysis. Cells were analyzed by Victor^{3} Multilabel Readers.

Chapter 3 Results and Discussion

3.1 PAN nanoparticles for bioimaging

3.1.1 Fabrication of PAN nanoparticles

Figure 7 represents overall preparation procedure of PAN nanoparticles containing PL properties, which are conjugated with antibody for bio-labeling. PAN nanoparticles were produced by ultrasonic mediated emulsion polymerization. Typically, acrylonitrile (AN) monomer (1.5 mL) with 0.5 g of sodium dodecylsulfate (SDS) was dissolved in 25 mL of distilled water and exposed to ultrasound for 10 min. After introducing the initiator, additional ultrasound was performed for 10 min. PAN nanoparticles with average diameter of 40 nm could be obtained by washing, precipitating, and drying process. These nanoparticles were loaded on reaction vessel with sealing apparatus. Then, the reaction vessel was evacuated and heated up to 70 ^{o}C. The vapor phase of EDA was added into the vessel, and surface treatment was carried out. When the PAN nanoparticles were exposed to EDA vapor at elevated temperature, the primary amines of EDA spontaneously reacted with the cyano-groups of PAN [59]. Therefore,

diverse functional groups including amine, imine, and Schiff bases were introduced onto the surface of pristine PAN nanoparticles [60]. Antibodies were conjugated on the treated PAN (tPAN) surface by conventional N-ethyl-N′-(3-dimethylaminopropyl) carbodiimide hydrochloride (EDC)/N-hydroxysuccinimide (NHS) activation [61].

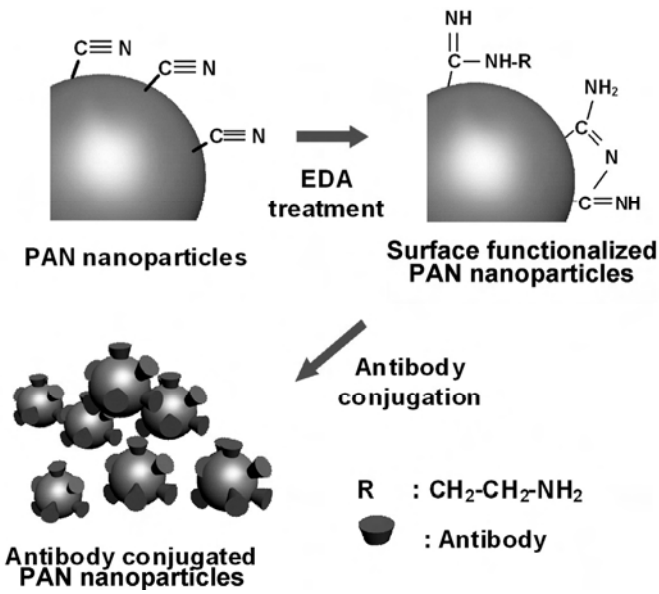

Figure 7. Schematic illustration for preparation procedure of antibody conjugated photo luminescent PAN nanoparticles.

Figure 8 demonstrates SEM and TEM images of PAN and tPAN nanoparticles. As shown in Figure 8a and b, the PAN nanoparticles with uniform diameter of *ca.* 40 nm were successfully fabricated by ultrasound induced emulsion polymerization. The diameter of PAN nanoparticles could be controlled by changing ratio of AN to SDS. The particle size of PAN nanoparticles can be varied from 48 nm to 18 nm by changing the monomer to SDS ratio from 4.0 to 1.0. It has been reported that an optimum geometry for endocytotic uptake is 20-50 nm and spherical shape [62]. Therefore, these nanoparticles could be suitable for cellular imaging probes. Furthermore, the synthesized PAN nanoparticles can be readily redispersible in aqueous media, even after removing anionic surfactants. SEM and TEM image of tPAN nanoparticles are presented in Figure 8c and d. Although the particle size of tPAN nanoparticles slightly increases, overall particle shape and water dispersity are maintained after EDA treatment (Figure 9). It is obvious that the preparation procedure of tPAN nanoparticles is relatively simple comparing to that of core/shell type of inorganic counterparts. In addition, vapor phase reaction provides diverse advantages over solvent treatments such as solvent-free technique, no recovering procedure and high potential to scale up.

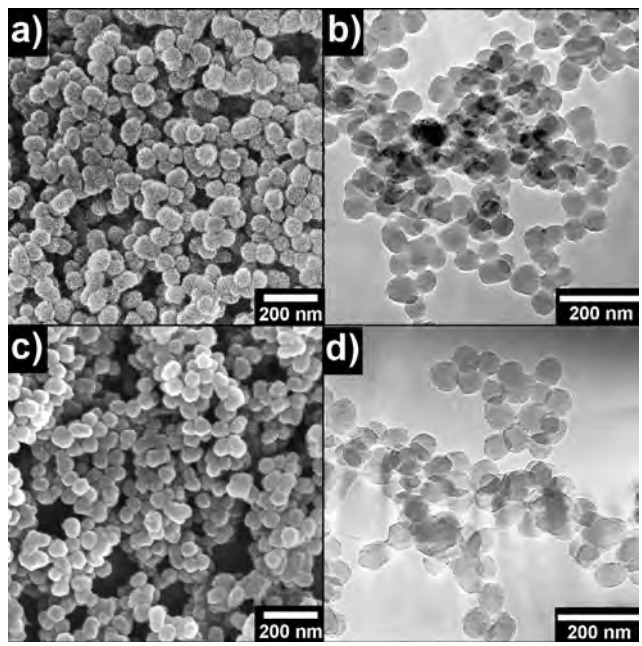

Figure 8. SEM image of PAN nanoparticles (a) and tPAN nanoparticles (c), and corresponding TEM images (b and d).

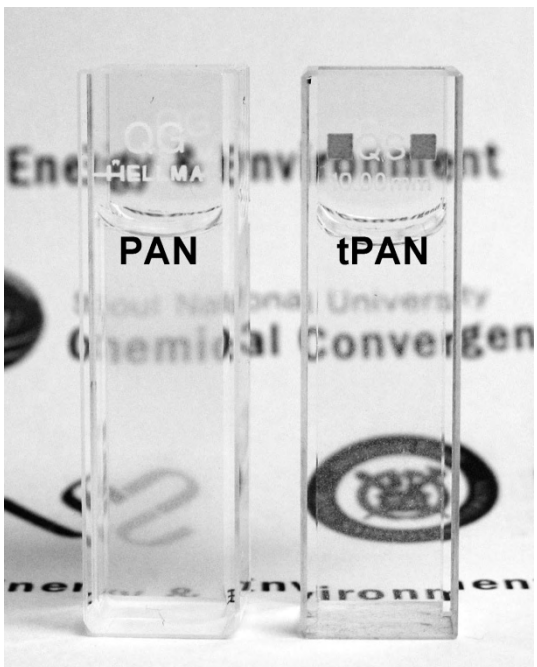

Figure 9. Photograph of aqueous media containing PAN and tPAN nanoparticles (0.1 mg mL^{-1}).

Figure 10 displays Fourier transform infrared (FTIR) spectra of PAN and tPAN with respect to different reaction time of vapor treatment. The FTIR spectrum of PAN nanoparticles represents characteristic peaks of PAN (black arrows in Figure 10), including the C≡N stretching band at 1446 cm^{-1}, and the C–H stretching peak at 2872 cm^{-1}. This result implies the successful polymerization of PAN by ultrasound process [63]. In the case of tPAN, the peaks related with nitrogen functional groups (red arrows) increased generally with increasing reaction time [64]. However, the characteristic peaks for PAN also appeared at tPAN, because the EDA was treated on the upmost surface of nanoparticles. Detailed peak assignments are illustrated in Table 1.

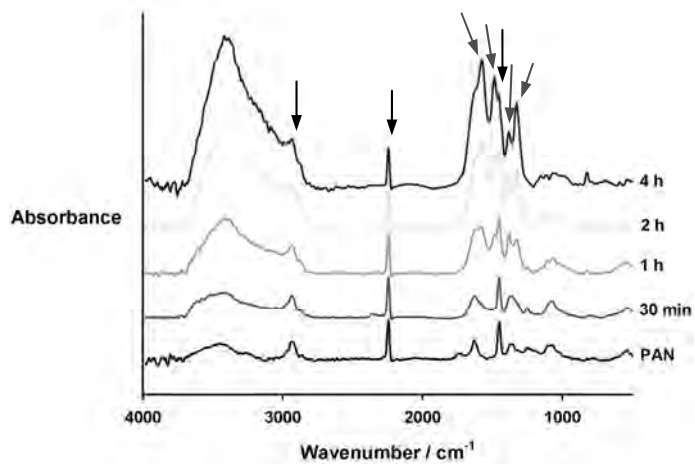

Figure 10. FTIR spectra of PAN and tPAN nanoparticles as a function of reaction time. The time increasing (30 min, 1, 2, and 4 h) represents the EDA treatment time on the PAN nanoparticles.

Table 1. FTIR assignment of PAN and tPAN nanoparticles

Materials	Wavenumber[a]	Assignments
PAN nanoparticles	2872	C−H stretching
	2241	C≡N stretching
	1446	C−H deformation
EDA Treated PAN nanoparticles	1568	N−H deformation of amine group
	1479, 1375	C−H stretching conjugated with EDA
	1319	C−N stretching
	815	N −H rocking

[a] unit: cm^{-1}

3.1.2 Application for bioimaging

The treatment of EDA on PAN nanoparticles can provide useful functional groups in biological applications, as well as make the PAN nanoparticles with the enhanced PL properties in label-free bioimaging. Figure 11 exhibits the absorption spectrum of the tPAN nanoparticles (4 h EDA treatment), PL spectra (excited at 270 nm), and emission photograph (inset; irradiated by 365 nm UV lamp) of the PAN and tPAN nanoparticles dispersed in aqueous solution with respect to EDA treatment time. The tPAN nanoparticles had an extinction band with a center wavelength of 268 nm. Although the bulk PAN had no PL properties, the PAN nanomaterials revealed violet luminescent, as described in our precedent work [64]. However, the violet emission has several limitations in bioimaging applications such as UV range excitation and poor eye-sensitivity. On the other hand, blue emission was enhanced as increasing reaction time of EDA treatment. The emission color can be directly compared from the photograph presented in inset of Figure 11. The tPAN with 4 h EDA treatment possessed useful emission color, which was adoptable in bioimaging. The tPAN nanoparticles represented broad-band PL spectrum in the range of 350-500 nm. The fluorescence quantum yield of the tPAN nanoparticles with 4 h treatment exhibited *ca.* 0.11, approximately 2.6

times higher than that of DAPI as a typical organic dye [54]. The mechanism of change of PL properties in tPAN nanoparticles was not fully understood, but it might be responsible for formation of Schiff base onto the cyano-groups or π-conjugation on the surface by the EDA treatment [65]. The fluorescence *via* Schiff bases that was very similar with the fluorescence phenomenon of the tPAN nanoparticles had been severally reported [59]. However, Further research should be performed to understand the fluorescence mechanism of the tPAN nanoparticles.

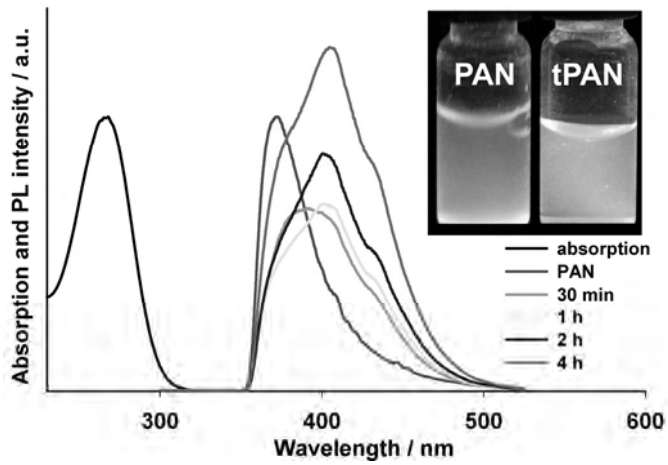

Figure 11. Absorption and emission spectra of PAN and tPAN nanoparticles colloid dispersed in aqueous media (inset: photograph of emission of colloids excited by 365 nm UV lamp).

The viability of PAN and tPAN treated human breast cancer cell lines (SK-BR-3) in 24 h incubation are exhibited in Figure 12. The PAN nanoparticles had no significant drop in viability below 25 μg mL^{-1} of particle concentration. The viability of PAN nanoparticles at these concentrations was more than 10 times higher than that of QDs and inorganic nanomaterials [66, 67]. It is generally accepted that the bulk PAN is also biocompatible when the unreacted monomer is perfectly removed. In addition, no large discrepancy was observed in cell viability of tPAN nanoparticles comparing with that of PAN nanoparticles. Therefore, it can be concluded that the tPAN nanoparticles are novel and powerful candidate to be applied in bioimaging agents.

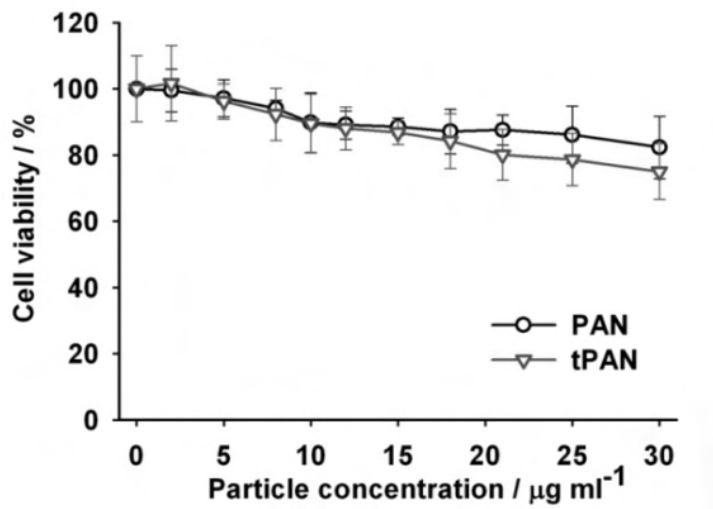

Figure 12. Cell viability of PAN and tPAN nanoparticle treated human breast cancer cells (SK-BR-3) at different particle concentrations for 24 h. Error bars represent standard deviations (n=3).

Figure 13 represents the live cell microscopic images of breast cancer SK-BR-3 cell labeled with tPAN nanoparticles and antibody conjugated tPAN nanoparticles for 24 h. As illustrated in Figure 13a, the tPAN could be also observed in cancer cell although the emission intensity and population were relatively smaller than the antibody conjugated tPAN nanoparticles. It was previously reported that the endocytosis of amine treated nanoparticles into the cells was relatively well accomplished due to the electrostatic attraction between positive charge of amine group and negative charge of cell lipid layer [68,69]. As a model system, the tPAN was conjugated with the anti-ErbB2 antibody to image SK-BR-3 cell. It was obvious that the cancer cell was covered by antibody conjugated tPAN nanoparticles with larger population of emission sites than tPAN nanoparticles (Figure 13b). No specific decrement of emission intensity was observed when the tPAN nanoparticles were conjugated with antibody. As a control experiment, polyethylene glycol (PEG) conjugated tPAN nanoparticles were used to reduce non-specific binding (Figure 13c). The majority of the PEG conjugated tPAN located on the surface or outside of the cells due to the electrostatic repulsion. The PL property of the tPAN nanoparticles was bright enough for cell imaging and the fluorescence images were well recognizable. In addition, it is clearly shown that the nanoparticles are incorporated into

the cell, as described in time lapse live cell fluorescent images of SK-BR-3 cell incubated with antibody conjugated tPAN nanoparticles for 11 h (Figure 14). Figure 15 shows the Z-sectional live cell microscopic images, indicating that the nanoparticles are not just attached onto the cell surface, but uptaken into the cytoplasm of cells. Therefore, it can be concluded that the prepared tPAN nanoparticles successfully play a pivotal role in detecting human breast cancer cell as a bioimaging probe.

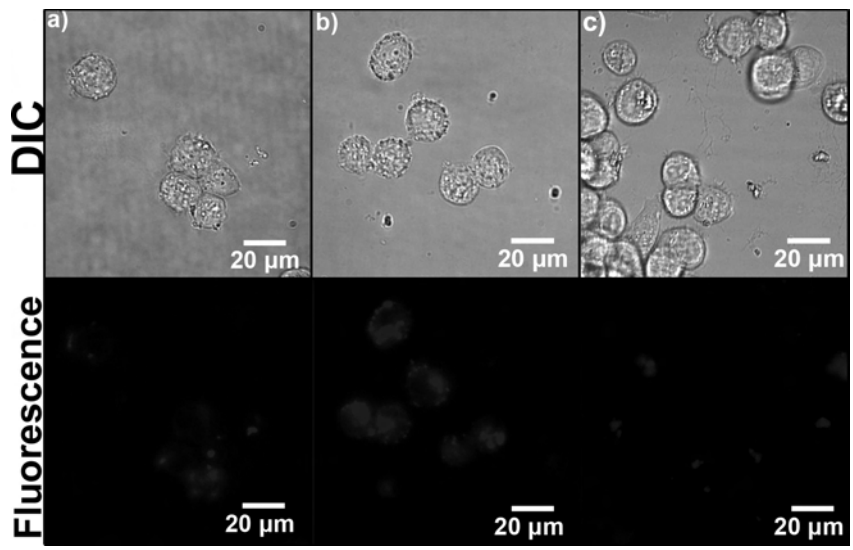

Figure 13. Live cell microscopic images of human breast cancer SK-BR- 3 cells incubated with a) tPAN nanoparticles, b) anti-ErbB2 antibody conjugated tPAN nanoparticles, and c) PEG conjugated tPAN nanoparticles.

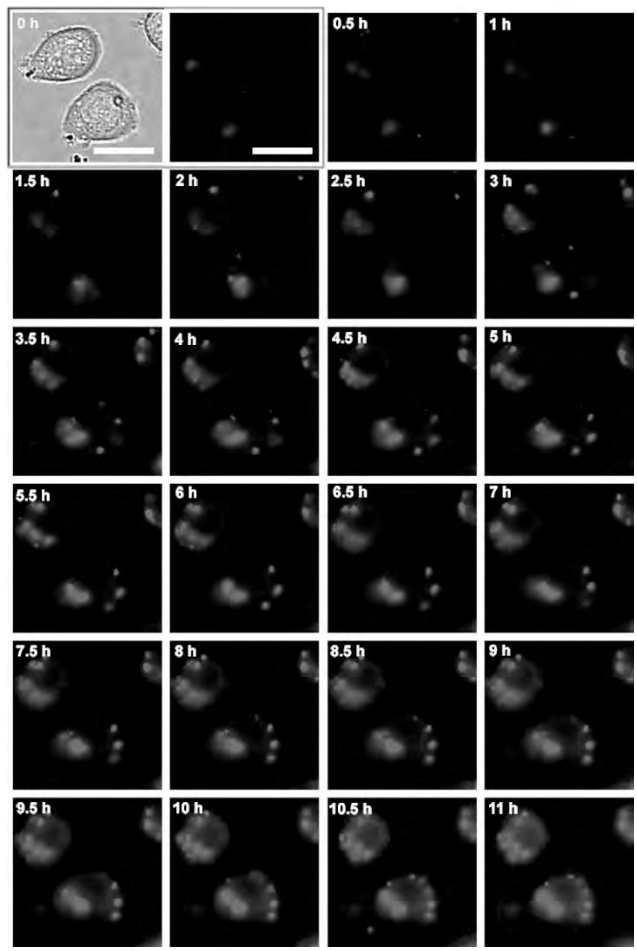

Figure 14. Time lapse live cell fluorescent images of antibody conjugated tPAN nanoparticles in SK-BR-3 cells over 11 h. The blue represents nanoparticles in cells. The scale of each square is 50 μm. The images are taken at 30 min interval for 11 h.

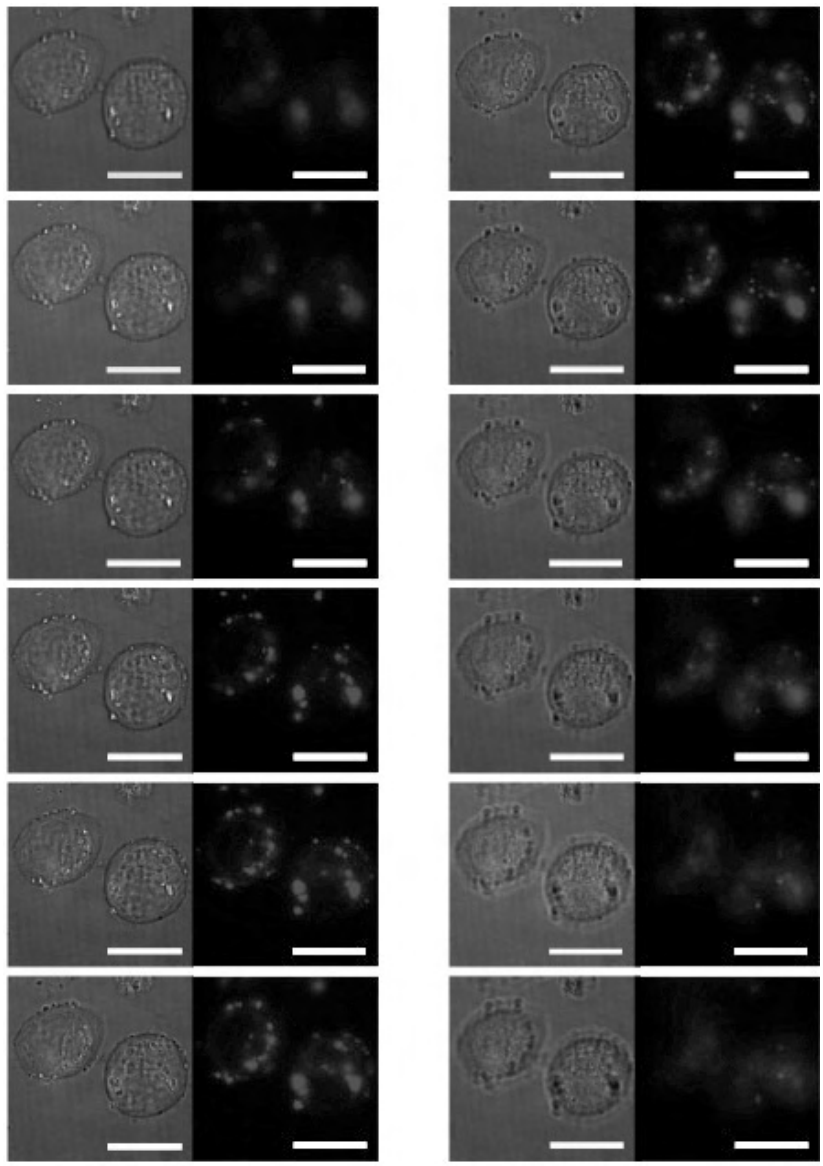

Figure 15. Differential interface contrast (DIC) and fluorescent z-sectioning images of SK-BR-3 cell treated with antibody conjugated tPAN nanoparticles for 24 h. The sections are ordered from apex of the cell to the near substrate plane. Z-scan step width is 0.1μm. (Scale bars: 20 μm)

3.2 PAN nanoparticles for Anthrax detection

3.2.1 Fabrication of PAN nanoparticles

A europium-modified fluorescence PAN (denoted Eu-PAN) nanoparticle sensor was prepared by the procedure shown in Figure 16. PAN nanoparticles of two different sizes were fabricated by microemulsion polymerization. To fabricate PAN nanoparticles of 25 and 50 nm (denoted PAN25 and PAN50), acrylonitrile (AN) monomer was dissolved in distilled water with DeTAB. After introduction of an initiator (APS), the microemulsion polymerization of AN monomer proceeded for 24 h. Thus, PAN nanoparticles with average diameters of 25 and 50 nm were acquired, as shown in the SEM images in Figure 17. SEM images of PAN nanoparticles exhibited monodispersity and were well-dispersed in aqueous solution at 50 mg mL^{-1}. The Pinner method was used to introduce Schiff bases onto the surface of PAN nanoparticles [59]. An intermediate imidoester was formed by reaction of the nitrile on the PAN nanoparticles with alcohol and hydrogen chloride under nitrogen. In the next step, an amidine group was obtained when the hydrochloride of the imidoester reacted with ammonia in an alcoholic solvent. Finally, the Schiff base was achieved by reaction with the amidine group and aldehyde group (denoted S-

PAN). For grafting the sensing moiety (europium) onto the nanoparticles, in the first step, ethylenediamine (EDA) was covalently grafted onto the S-PAN nanoparticles. In the second step, ethylenediaminetetraacetic acid dianhydride (EDTAD) was introduced onto the nanoparticles, leading to the reaction between the amino groups and the anhydride groups. The resulting EDTAD ligand on the nanoparticles was then converted into [Eu(EDTA)-$(H_2O)_3$)] complex by reaction with $EuCl_3$. Nanoparticle shapes were maintained after the surface modification steps, while the size of the Eu-PAN nanoparticles increased slightly, from approximately 25 to 27 nm and from 50 to 53 nm.

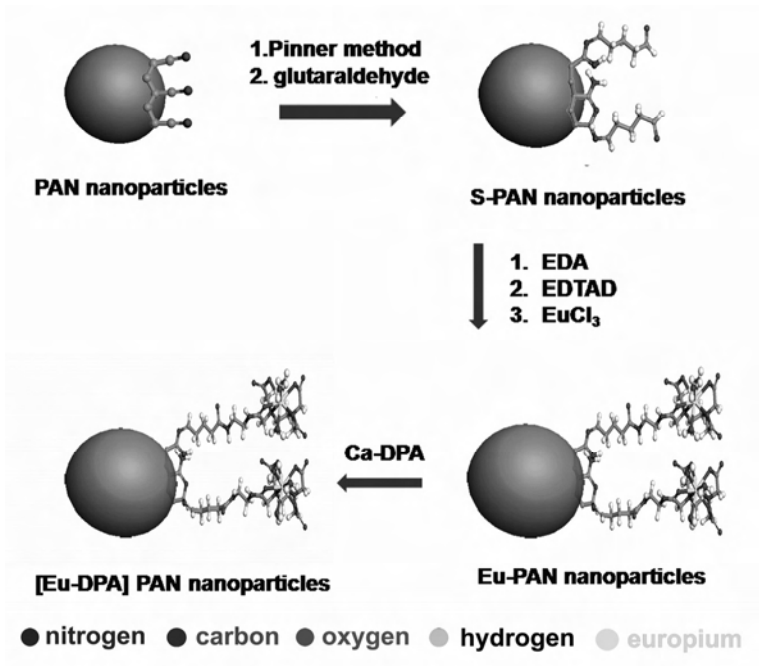

Figure 16. Schematic diagram for fabrication procedure of Eu-PAN nanoparticles and their sensing process with Ca-DPA.

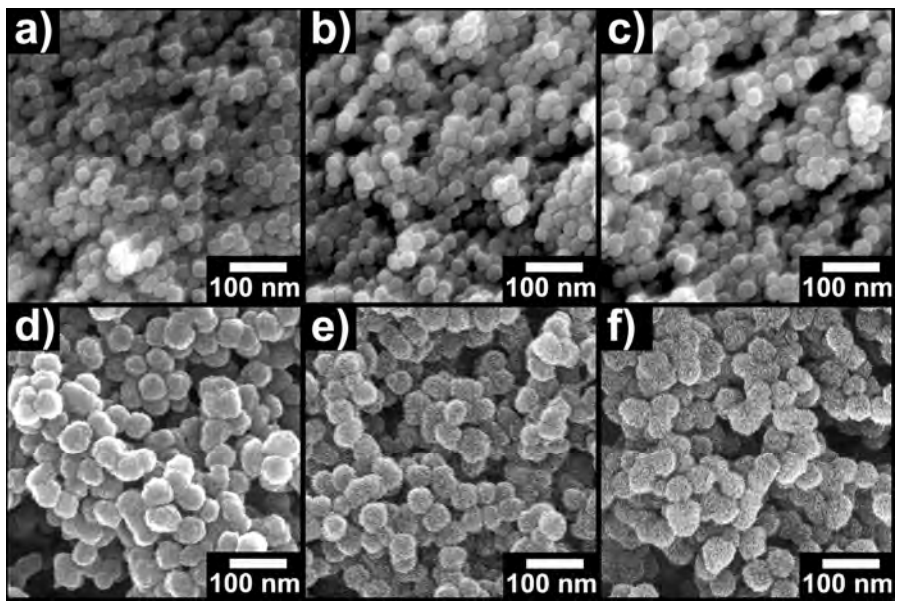

Figure 17. SEM images of a) PAN25, b) S-PAN25, c) Eu-PAN25, d) PAN50, e) S-PAN50, and f) Eu-PAN50 nanoparticles.

Formation of PAN, S-PAN, and Eu-PAN nanoparticles was confirmed by Fourier-transform infrared (FTIR) spectra (Fig. 18). The FTIR spectrum of the PAN nanoparticles shows the characteristic peaks of PAN, such as the C≡N stretching band at 2244 cm^{-1}, the C-H stretching peak at 2872 cm^{-1}, and the C-H deformation at 1446 cm^{-1}. These peaks indicate the successful polymerization of PAN by microemulsion polymerization [63]. In the case of S-PAN nanoparticles, the peaks related to the Schiff base increased, including the Schiff base peak at 1633 cm^{-1}, C-H deformation at 1384 cm^{-1}, N-H deformation at 1261 cm^{-1}, and NH_3^+ rocking at 804 cm^{-1} [64]. However, the characteristic peaks for PAN almost disappeared because the surface of the nanoparticles was successfully modified with the Schiff base. In the case of Eu-PAN nanoparticles, new peaks of carboxylic acid salts at 1592 cm^{-1} and 1394 cm^{-1}, and N-H deformation at 1538 cm^{-1} appeared due to formation of [Eu(EDTA)]. The FTIR peak assignments are summarized in Table 2. X-ray photoelectron spectroscopy (XPS) analysis was obtained for characterizing the surface modification of PAN nanoparticles. Fig. 18b exhibits full-scale XPS spectra of PAN, S-PAN, and Eu-PAN nanoparticles. The atomic concentrations of C, N, and O in PAN nanoparticles were determined to be 78.88, 17.93, and 3.29%, respectively (black line). In the case of S-PAN (red line), the atomic concentrations were 79.71, 4.35, and

15.94%, respectively. Additionally, Eu (3.77%) appeared and O (23.9%) increased in Eu-PAN mainly due to [Eu-(EDTA)] complex (blue line). Enlarged C 1s, N 1s, O 1s, and Eu 4d region of XP spectra denoted successful fabrication of S-PAN and Eu-PAN nanoparticles (Figure 19, 20, 21, and 22)

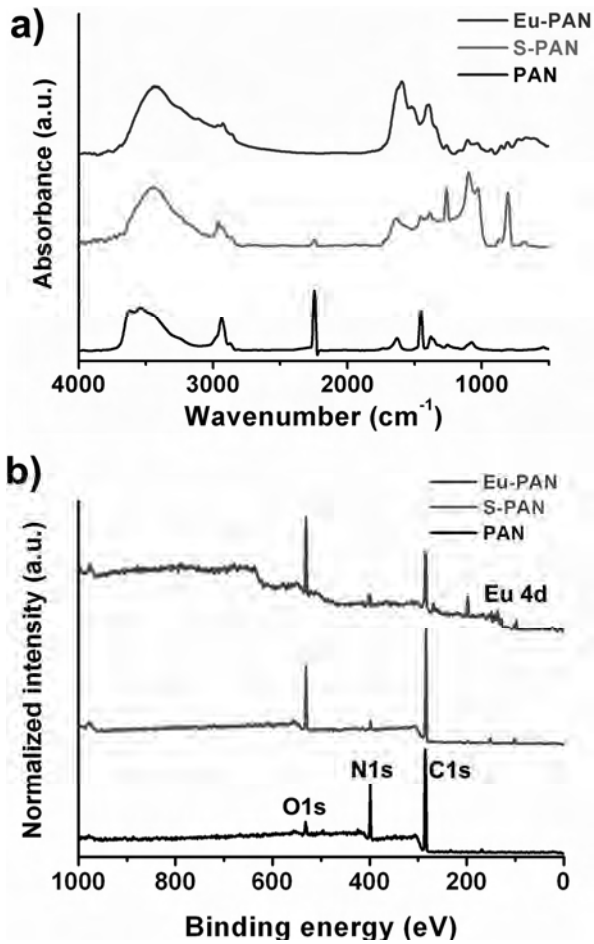

Figure 18. a) FTIR spectra of PAN, S-PAN, and Eu-PAN nanoparticles, b) XP survey spectra of PAN (black line), S-PAN (red line), and Eu-PAN (blue line).

Table 2. FTIR assignments of PAN, S-PAN, and Eu-PAN nanoparticles.

Materials	Wavenumber[a]	Assignments
PAN nanoparticles	2873	C−H stretching
	2244	C≡N stretching
	1452	C−H deformation
S-PAN nanoparticles	1633	Schiff bases
	1452	CH_3 deformation
	1409	C-H rocking
	1384	C-H symmetric deformation
	1261	N-H deformation
	804	NH_3^+ rocking
Eu-PAN nanoparticles	1592, 1394	Carboxylic acid salts
	1538	N-H deformation, amide

[a] unit: cm^{-1}

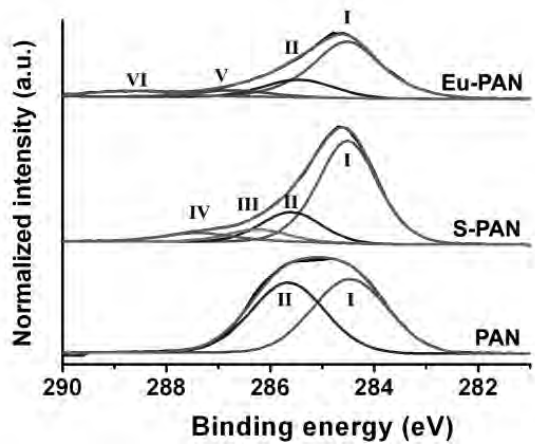

Figure 19. Enlarged C 1s spectra of PAN, S-PAN, and Eu-PAN nanoparticles.

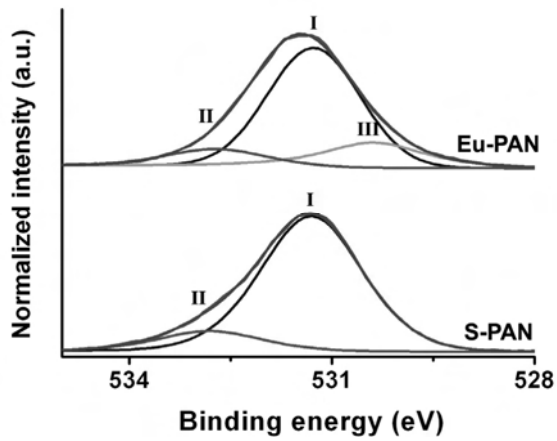

Figure 20. Enlarged O 1s spectra of PAN, S-PAN, and Eu-PAN nanoparticles.

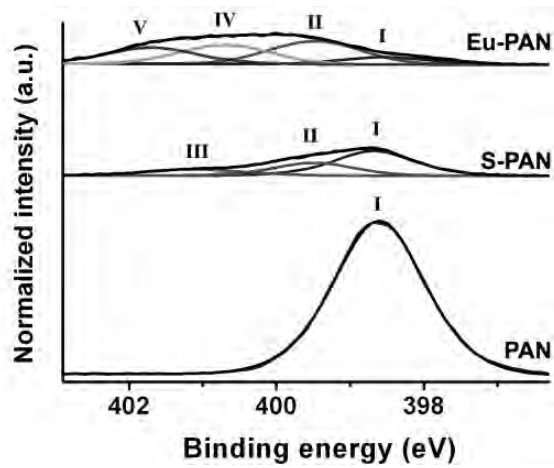

Figure 21. Enlarged N 1s spectra of PAN, S-PAN, and Eu-PAN nanoparticles.

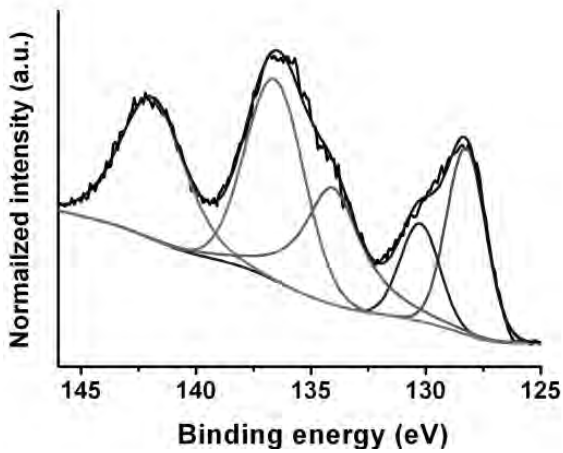

Figure 22. Enlarged Eu 4d spectra of PAN, S-PAN, and Eu-PAN nanoparticles.

3.2.2 Application for Anthrax detection

Schiff base-modified PAN (S-PAN) nanoparticles exhibited enhanced and red-shifted fluorescence compared with nanoparticles in our previous report [12]. Treatment of the Schiff base on the PAN nanoparticles can also provide useful functional groups (*e.g.,* aldehyde groups) for biological applications, as well as make PAN nanoparticles with enhanced PL properties. Fig. 23a shows the PL spectrum of S-PAN nanoparticles (black line; excitation at 360 nm). The fluorescence quantum yield of the S-PAN nanoparticles was *ca.* 0.15, which was approximately 3.75-fold higher than that of the typical organic dye DAPI [54]. Furthermore, this quantum yield was *ca.* 1.36-fold higher than that of PAN nanoparticles reported previously [61]. The surface functional groups of PAN nanoparticles were considered to be well converted to Schiff bases by the solution process, compared with the vapor deposition process described previously [54]. Additionally, this modification method provides both reference fluorescence and functional groups for further attachment of lanthanide metals.

Fluorescence recognition of Ca-DPA was performed to detect anthrax using a Eu-PAN nanoparticle sensor. A representative PL spectrum of the Eu-PAN nanoparticles in the presence of 1 μM Ca-DPA is shown in Fig. 23a

(red line; excitation at 270 nm). Upon addition of Ca-DPA, two sharp emission peaks appeared, at 593 and 616 nm, through the formation of the [Eu(EDTA)-(DPA)] complex because of the transition of the Eu^{3+} excited states $^5D_0 \rightarrow {}^7F_J$ (J = 0, 1, and 2) [70]. It has been reported that attachment to DPA reduces the non-radiative quenching of Eu^{3+} emission, resulting in an increase in the quantum yield and a corresponding enhancement of the detection sensitivity for Ca-DPA [71]. Eu^{III}–macrocycle complex enables selective DPA binding in aqueous solution because macrocycles reduce non-radiative quenching by coordinating water molecules. Macrocyclic ligands such as EDTA and 1,4,7,10-tetraazacyclododecane-1,7-diacetate readily form Eu^{III}–macrocycle complex and exhibit following advantages for selective DPA binding: i) EDTA binding keeps three adjacent coordination sites open and does not inhibit DPA binding, ii) the [Eu(EDTA)(DPA)]-complex eliminates water quenching, and iii) the complex can be modified with other molecules [70]. Under UV irradiation (365 nm; Fig. 23a inset), the Eu-PAN nanoparticles showed blue emission because of the Schiff base on the surface, whereas DPA attachment produced magenta emission due to the [Eu(EDTA)-(DPA)] complex. In this case, the low concentration of Ca-DPA (1 μM) resulted in a color change, from blue to magenta, that could be seen with the naked eye. Moreover, the whole sensing procedure took only

20 s, enabling the rapid detection of anthrax (Fig. 23b). Rapid detection of Ca-DPA via Eu-PAN nanoparticles has considerable advantages in practical applications because Anthrax is an agent of bioterrorism.

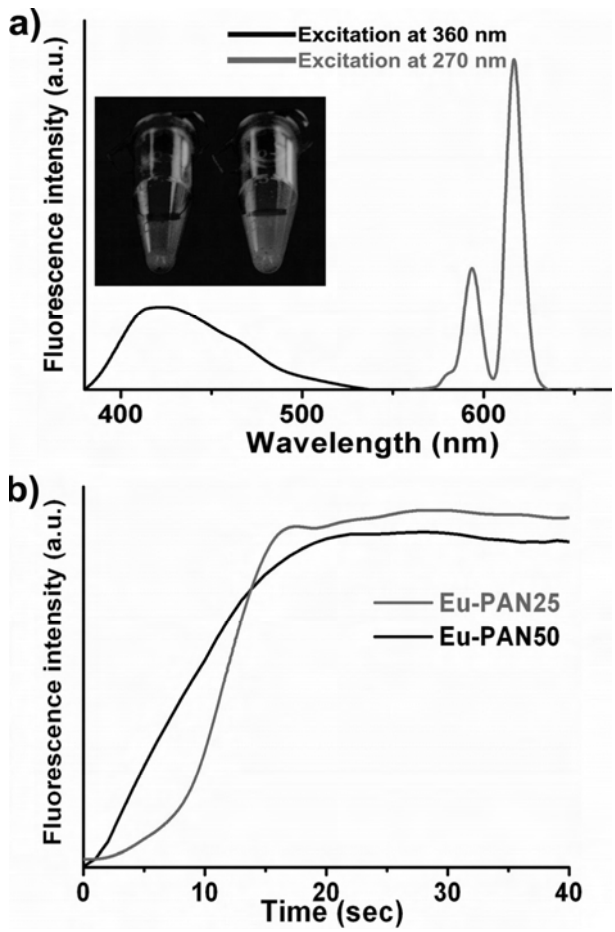

Figure 23. a) Representative fluorescence spectra of Eu-PAN excited at 360 nm (black line) and Eu-PAN nanoparticles excited at 270 nm (red line) (inset: photo of Eu-PAN and Eu-PAN nanoparticles in presence of 1 μM Ca-DPA under 365 nm UV irradiation); b) Time-dependent fluorescence intensity plot of Eu-PAN25 (red line) and Eu-PAN50 (black line) nanoparticles after Ca-DPA insertion (250 nM; detected at 616 nm emission).

To evaluate the sensitivity of Eu-PAN nanoparticles, different concentrations of Ca-DPA were added to 10 μM Eu-PAN nanoparticle solution. Inhalation of more than 10^4 *B. anthracis* spores can result in death, and thus a detection method should be both highly sensitive and rapid. The fluorescence intensities of Eu-PAN25 and Eu-PAN50 increased with addition of increasing concentrations of Ca-DPA, and were highly sensitive and ratiometric to Ca-DPA (Figure 24). The inset in Figure 24 shows the linear correlation between the emission intensity at 616 nm and the concentration of Ca-DPA (adjusted $R^2 = 0.998$ and 0.996 for Eu-PAN25 and Eu-PAN50, respectively). Compared with conventional fluorescence-based sensors, the Eu-PAN system has outstanding ability because the reference fluorescence plays a crucial role in omitting calibration curves and corrections for dilution.

The limit of detection (LOD) values of Eu-PAN25 and Eu-PAN50 nanoparticles for Ca-DPA were 10 pM and 50 pM, respectively, which was six orders of magnitude lower than the infectious dosage of the spores (6×10^{-5} M required). The sensitive $^5D_0 \rightarrow {}^7F_2$ change resulted in huge changes in the Eu^{3+} center and the displacement of three coordinating water molecules from the Eu^{3+} center [72]. Importantly, the Eu-PAN25 showed 5-fold higher sensitivity than Eu-PAN50. The higher surface area of the Eu-PAN25 system

is considered to have increased the frequency of contact with Ca-DPA, leading to higher fluorescence sensitivity. These LOD values were *ca*. 4–20-fold lower than those reported recently using lanthanide metals as a sensor reagent [71].

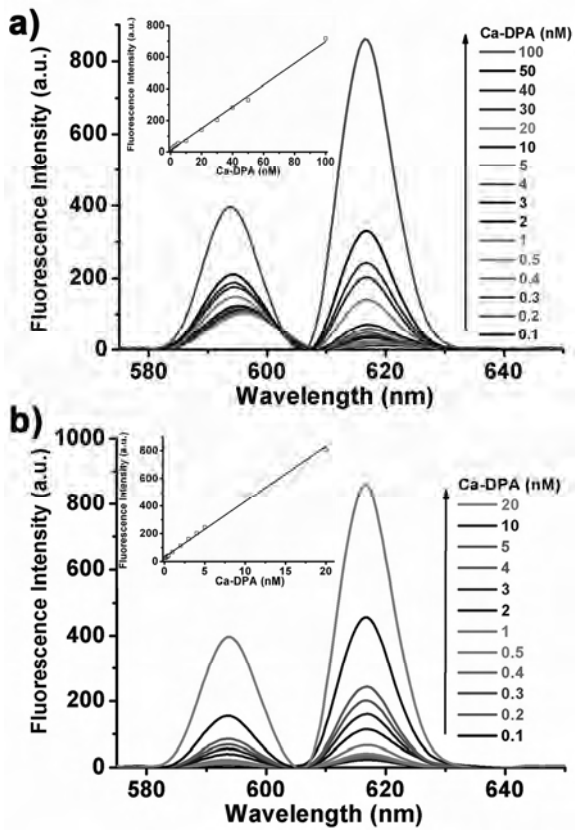

Figure 24. Fluorescence spectra of a) Eu-PAN25 nanoparticles and b) Eu-PAN50 nanoparticles in presence of Ca-DPA with concentration dependence (inset: plot of fluorescence intensity at 616 nm versus Ca-DPA concentration).

The sensitivity of terbium-modified PAN (designated Tb-PAN) nanoparticles was investigated as a control lanthanide metal sensor (Fig. 25). The Tb-PAN nanoparticles were also sensitive to Ca-DPA and the fluorescence intensity was increased by addition of increasing concentrations of Ca-DPA (excitation at 270 nm). Linear correlations were observed between the maximum emission intensities at 585 nm of Tb-PAN25 and Tb-PAN50 and the concentration of Ca-DPA (adjusted $R^2 = 0.994$ and 0.995, respectively; Fig. 25 inset). The relatively low fluorescence intensity and secondary scattering peak of Tb-PAN nanoparticles were major obstacles for detecting Ca-DPA. The [Tb(EDTA)-(DPA)] complex has a greater quantum yield than other lanthanide complexes because of the small energy gap and corresponding strong coupling between the Ca-DPA triplet state and the $^5D_4$ excited state of terbium [70]. However, when Tb-PAN nanoparticles were excited at 270 nm, the most efficient value, second-order scattering emission at 540 nm disrupted observation of the 544 nm emission of Tb-PAN [71]. Thus, the emission at 585 nm was used in Tb-PAN nanoparticle sensors for *B. anthracis* spores with lower intensity.

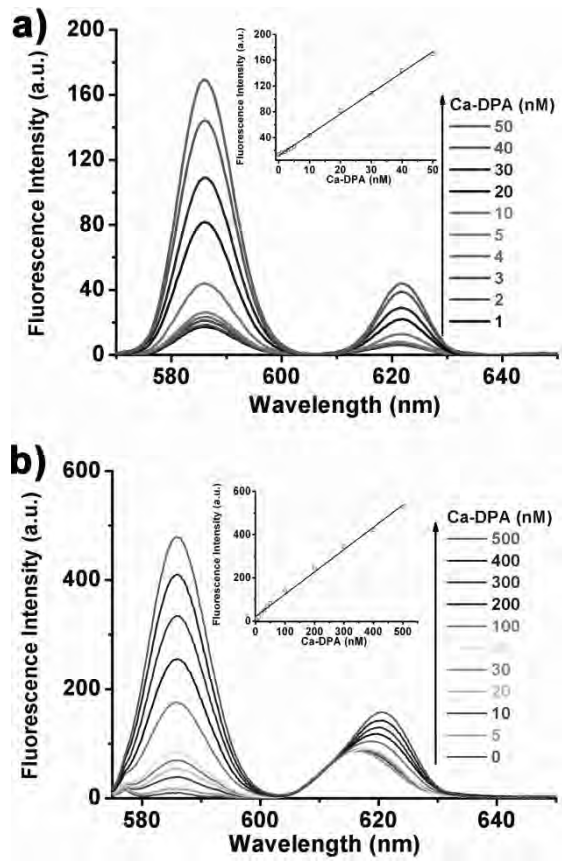

Figure 25. Fluorescence spectra of a) Tb-PAN25 nanoparticles and b) Tb-PAN50 in presence of Ca-DPA with concentration dependence (inset: plot of fluorescence intensity at 585 nm versus Ca-DPA concentration).

The principal function of Eu-PAN nanoparticle sensors is to bind Ca-DPA without interference by nonselective binding of aromatic ligands to Eu^{3+}, thus allowing practical application as an anthrax sensor. To investigate the selectivity of Eu-PAN nanoparticles different aromatic ligands, such as benzoic acid, terephthalic acid, and nicotinic acid, were used. Table 3 shows normalized fluorescence intensity ratios (I/I_0) of Eu-PAN nanoparticles (10 μM: Eu^{3+}) on aromatic ligands (1000 nM). Although there was almost no change for these ligands at the high concentration, Ca-DPA showed noticeable fluorescence improvement of both Eu-PAN25 and Eu-PAN50 (approximately 160- and 136-fold higher than other aromatic compounds, respectively). The bound water molecules with Eu^{3+} were considered not to be substituted by these aromatic ligands. Additionally, the smaller nanoparticles (Eu-PAN25) showed higher selectivity due to the increase in surface area-to-volume-ratio. These results indicated that the Eu-PAN nanoparticle sensor has outstanding ability to translate and amplify [Eu(EDTA)-(DPA)] interaction into detectable and ratiometric fluorescence with high sensitivity and selectivity, thus enabling accurate and rapid sensing for practical applications.

Table 3. Normalized fluorescence intensity (I/I_0) changes upon addition of Ca-DPA and different aromatic ligands onto Eu-PAN25 and Eu-PAN50 nanoparticles (1000 nM for each ligand).

	Eu-PAN25 (I/I_0)	Eu-PAN50 (I/I_0)
Ca-DPA	160.53	136.01
benzoic acid	0.98	0.95
terephthalic acid	1.48	1.01
nicotinic acid	1.30	1.00
isophthalic acid	1.60	1.24
picolinic acid	2.12	1.69

3.3 PAN nanoparticles for intracellular H_2O_2 detection

3.3.1 Fabrication of PAN nanoparticles

BPAN nanoparticles were prepared using the procedure displayed in Figure 26. First, 50-nm-diameter PAN nanoparticles were fabricated using radical polymerization by dissolving acrylonitrile (AN) monomer in distilled water with a stabilizer. After introducing ammonium persulfate, the radical polymerization of the AN monomer proceeded for 24 h. The PAN nanoparticles were uniform and monodispersed, as determined by SEM and TEM (Figure 27). A Schiff base was achieved by surface modification via the Pinner method and further aldehyde reaction. Finally, the BPAN nanoparticles were produced upon treatment with 3-aminopyridine-5-boronic acid pinacol ester.

The formation of PAN and BPAN nanoparticles was confirmed by Fourier-transform infrared (FT-IR) spectrometry (Figure 28 and Table 4). The FT-IR spectrum of the PAN nanoparticles shows characteristic PAN peaks, including the C≡N stretching bands at 1446 and 2244 cm^{-1} and the C–H stretching peak at 2872 cm^{-1} [63]. These peaks reveal the successful polymerization of PAN by microemulsion polymerization. For the BPAN nanoparticles, peaks related to the boronic acid pinacol ester and Schiff base

appeared, including symmetric B–O stretching at 1097 cm^{-1}, asymmetric C–O stretching at 1290 cm^{-1}, B–O stretching at 1402 cm^{-1}, B–C stretching at 1465 cm^{-1}, and the Schiff base peak at 1652 cm^{-1} [73]. Based on these data, boronic acid pinacol ester successfully modified the nanoparticle surfaces. X-ray photoelectron spectroscopy (XPS) was employed to characterize the surface modification of the PAN nanoparticles (Figure 29, 30, 31, 32, and 33). XP survey spectra and enlarged C 1s, N 1s, O 1s, and B 1s spectra confirmed the successful fabrication of PAN and BPAN nanoparticles.

To obtain the information on BPAN nanoparticle structure, the present nanoparticles were subjected to ^{13}C solid-state NMR measurement. Figure 34 shows NMR spectra with CPMAS measurement modes. The spectrum of BPAN nanoparticles (black line) represents the expected signals for Schiff base and pyridine boronic acid pinacol ester modification, which can be assigned on the basis of data reported in the previous literature [74,75]. Briefly, broad signal *a* at 31.9 ppm is assigned to the aliphatic chain of the BPAN. The region 72.0 and 122.2 ppm (*b* and *c*) are assigned to the Schiff base and pyridine, respectively, and the region 212.6 ppm (*e*) is assigned to boronic acid pinacol ester in the BPAN nanoparticles.

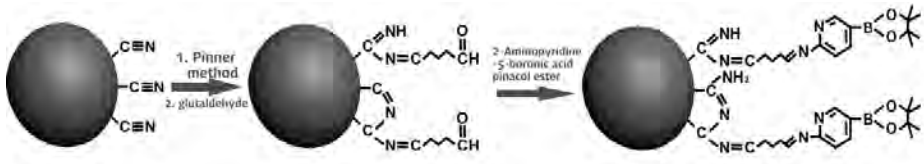

Figure 26. Schematic diagram of fabrication of BPAN nanoparticles.

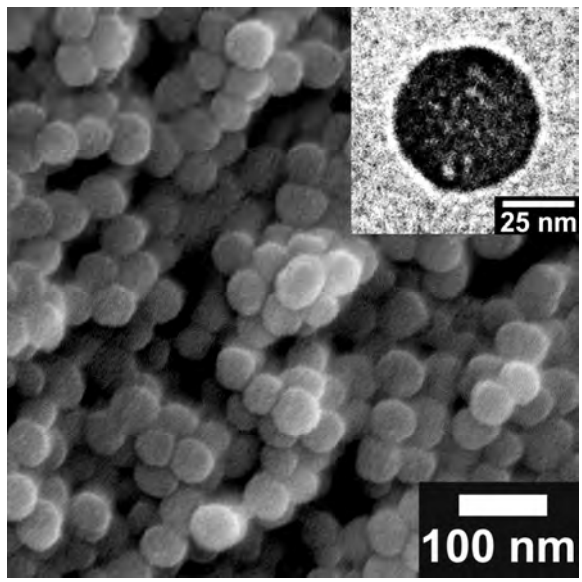

Figure 27. SEM image of BPAN nanoparticles (inset: TEM image of BPAN nanoparticles).

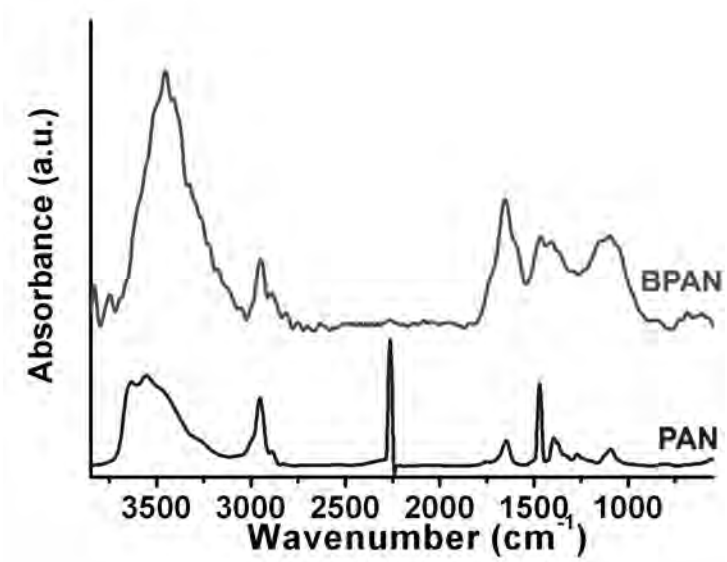

Figure 28. FT-IR spectra of PAN (blue line) and BPAN (red line) nanoparticles.

Table 4. FT-IR assignments of PAN and BPAN nanoparticles.

Materials	Wavenumber[a]	Assignments
PAN nanoparticles	2873	C−H stretching
	2244	C≡N stretching
	1446	
BPAN nanoparticles	1097	Symmetric B-O stretching
	1290	Asymmetric C-O stretching
	1402	B-O stretching
	1465	B-C stretching
	1652	Schiff bases

[a] unit: cm^{-1}

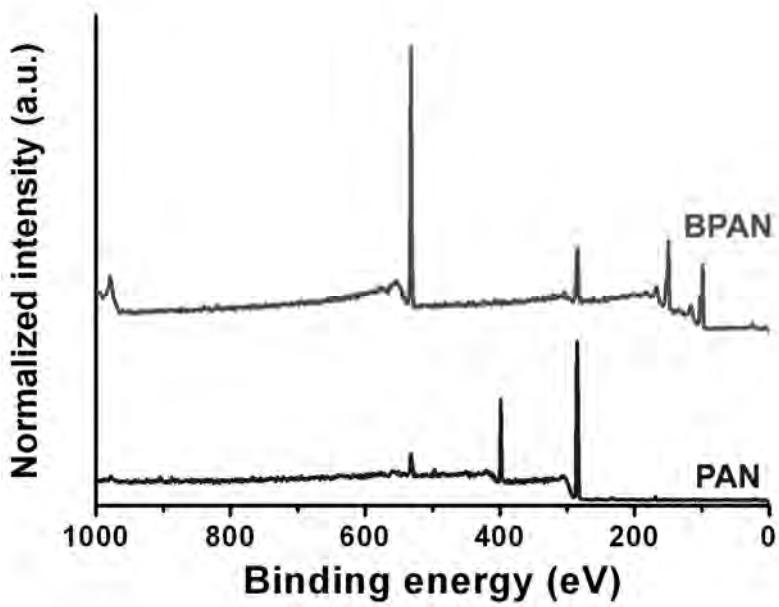

Figure 29. XP survey spectra of PAN (blue line) and BPAN (red line) nanoparticles.

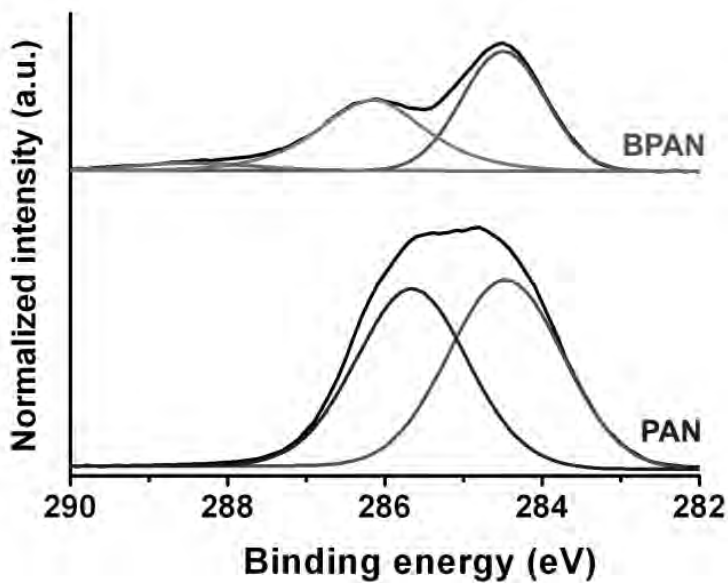

Figure 30. Enlarged C 1s spectra of PAN and B-PAN nanoparticles.

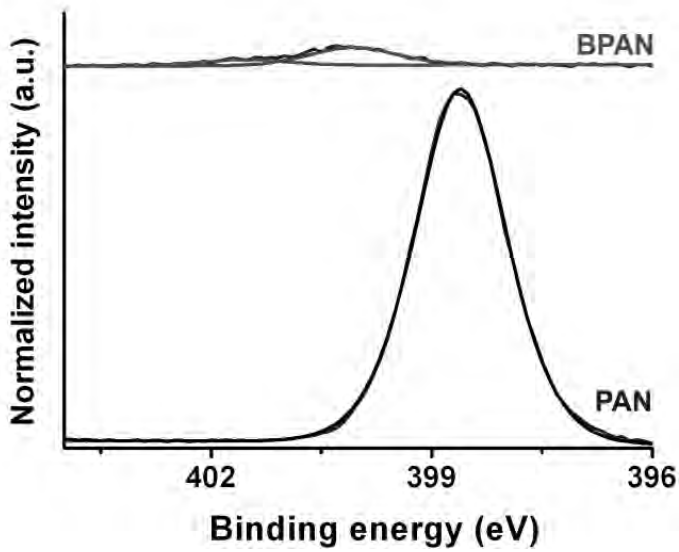

Figure 31. Enlarged N 1s spectra of PAN and BPAN nanoparticles.

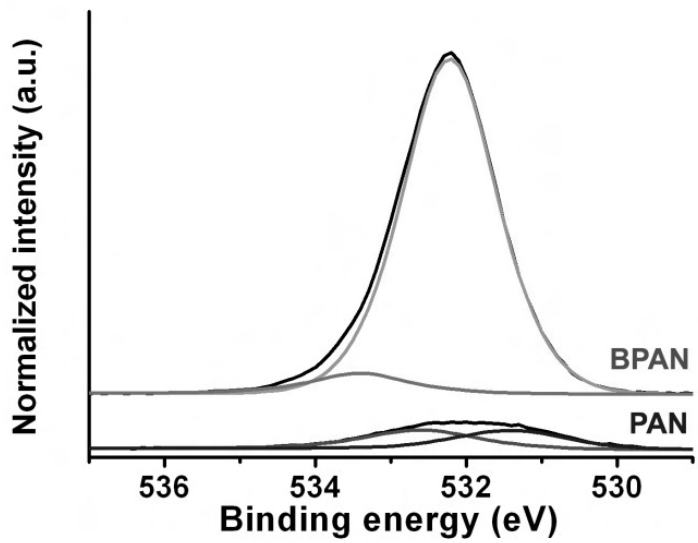

Figure 32. Enlarged O 1s spectra of PAN and BPAN nanoparticles.

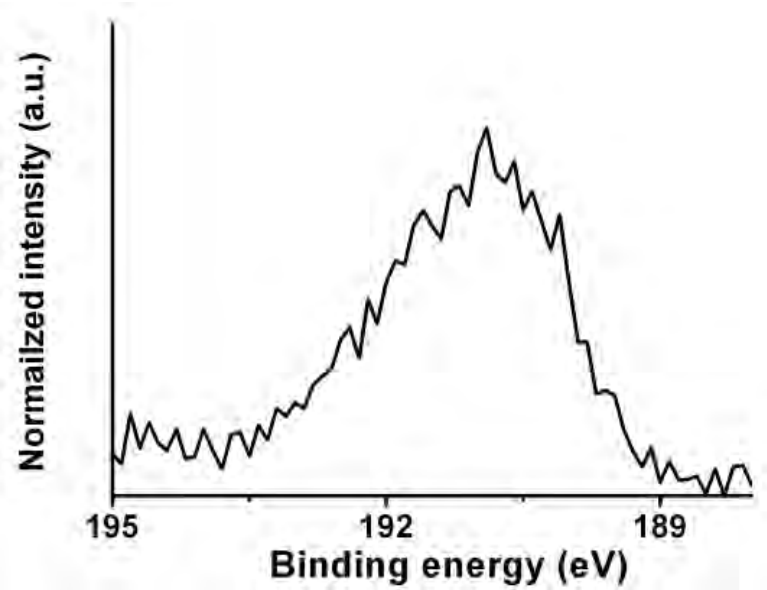

Figure 33. Enlarged B 1s spectrum of BPAN nanoparticles.

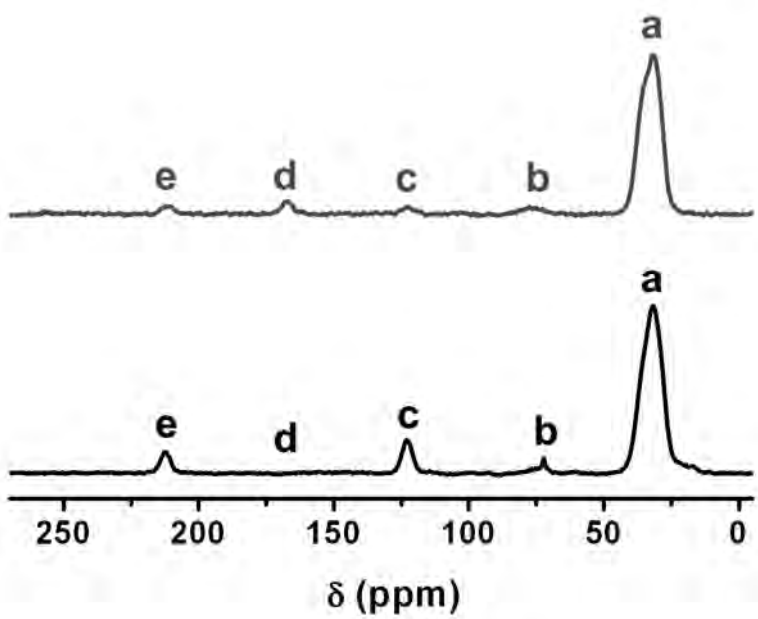

Figure 34. ^{13}C solid-state NMR spectra of the present BPAN (black line) and HPAN (red line) nanoparticles with CPMAS measurement.

3.3.2 Application for intracellular H_2O_2 detection

Figure 35 shows selective H_2O_2 sensing via fluorescent BPAN nanoparticles. Fluorescent PET sensors generally include a receptor and a fluorophore separated by a spacer to create a donor–bridge–acceptor system; on the BPAN nanoparticles, this donor–bridge–acceptor system is supplied by the Schiff base group and boronate [76]. Figure 35 inset shows representative fluorescence spectra of PAN and BPAN nanoparticles. The fluorescence quantum yield of the PAN nanoparticles (after Schiff base treatment) was *ca*. 0.15 (blue line; excitation at 360 nm), which was approximately 3.75-fold higher than that of the organic dye DAPI [54]. The BPAN nanoparticles showed up to *ca*. 6-fold fluorescence enhancement compared with that of the PAN nanoparticles (red line). Moreover, the excitation/emission (300 nm/376 nm) of the BPAN nanoparticles exhibited blue shifts compared to that of the PAN nanoparticles. This spectral change could be due to efficient electronic communication between the Schiff base and pyridine boronic acid pinacol ester group; for example, the construction of the π-conjugation and PET systems [77,78].

Reaction with H_2O_2 converts BPAN nanoparticles to H_2O_2-treated (HPAN) nanoparticles, in which some of the boronate groups are replaced by

pyridone groups [79,80]. This hydroxy group in turn make the HPAN nanoparticles an effective metal chelator. The OH groups of HPAN nanoparticles, in combination with other intraparticle functionalities, such as imine N and deprotonated phenolate O^{-}, could selectively sequester iron. Owing to this chemospecific deprotection mechanism, boronate derivatives on the BPAN nanoparticles exhibit high selectivity for H_2O_2 over other ROS and can respond to changes in H_2O_2 fluxes at oxidative stress levels.

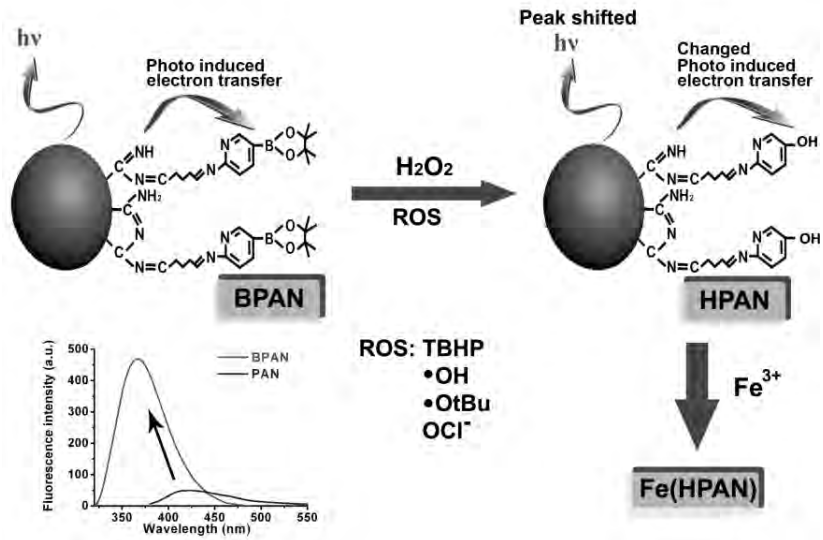

Figure 35. Schematic diagram of H_2O_2 detection using BPAN nanoparticles and representative fluorescence spectra of PAN (blue line) and BPAN (red line) nanoparticles.

We evaluated the spectral properties and H_2O_2 response of the new boronated nanoparticles in aqueous buffer at physiological pH (20 mM 4-(2-hydroxyethyl)-1-piperazinee-thanesulfonic acid (HEPES), pH 7; Figure 36). The boronate groups forced the BPAN nanoparticles to adopt a PET form that enhanced fluorescence in the blue region of the spectrum. The addition of H_2O_2 triggered a marked decrease in fluorescence intensity of the BPAN nanoparticles when the excitation wavelength was 300 nm. Moreover, a new emission peak, derived from the Schiff base, dramatically appeared after H_2O_2 treatment when the excitation wavelength was 360 nm. This peak was redshifted from 365 to 398 nm when the excitation wavelength was 320 nm. These observations provided a simple means to distinguish H_2O_2 from other ROS. The BPAN nanoparticles exhibited ratiometric detection of H_2O_2. The limit of detection (LOD) values of BPAN nanoparticles for H_2O_2 were 100 pM. This phenomenon is unique among conventional PET sensors and, to the best of our knowledge, has not been previously reported. We presume that intraparticle interactions are responsible for the peak shift and appearance. Additionally, the rate of conversion of BPAN to HPAN nanoparticles were determined by measuring the change in absorption using pseudo-first order reaction conditions with an excess of H_2O_2. The calculated rate constants indicated that the Schiff base and pyridine linkage in BPAN

nanoparticles provided the conversion with a rate constant of 3.59 $M^{-1}S^{-1}$.

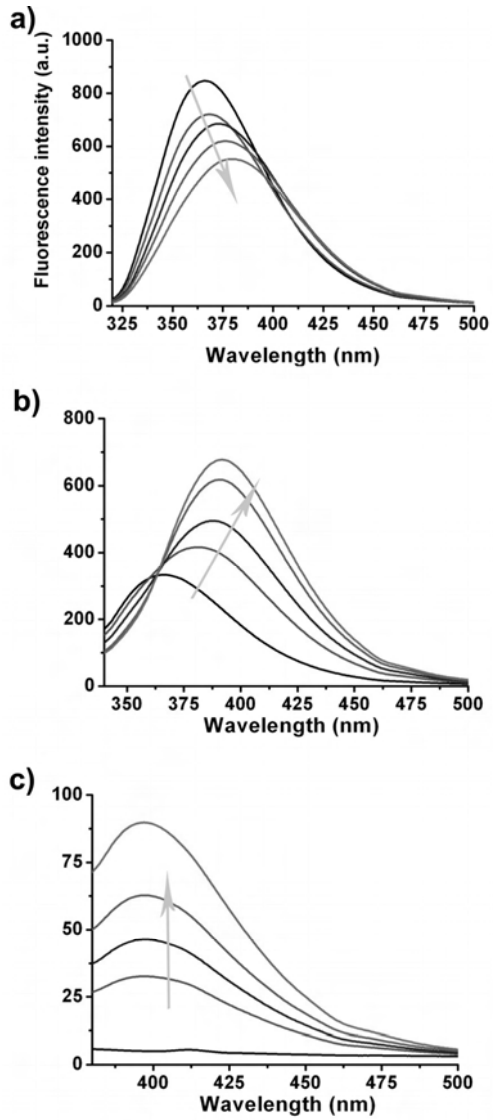

Figure 36. Ratiometric fluorescence spectral changes of 10 μg mL^{-1} BPAN nanoparticles in the presence of H_2O_2 as a function of different excitation wavelength: a) 300 nm, b) 320 nm, and c) 360 nm. Data were acquired at 25^{o}C in 20 mM HEPES, pH 7, 1min after the addition of H_2O_2. H_2O_2 concentrations represent 0, 20, 40, 60, and 80 μM.

Because of this chemospecific boronate switch and PET effect, the BPAN nanoparticles respond with good selectivity to H_2O_2 over a variety of biologically relevant ROS, including hypochlorite ($^-$OCl), tert-butyl hydroperoxide (TBHP), hydroxyl radical (·OH), and tert-butoxy radicals (·OtBu) (Figure 37). The fluorescence seen at an excitation wavelength of 360 nm was observed only when the BPAN nanoparticles interacted with H_2O_2, not with any other ROS, thus providing highly selective detection. Furthermore, the fluorescence response of the BPAN nanoparticles to H_2O_2 at three separate excitation wavelengths was clearly different from the response to other ROS, permitting one to distinguish between H_2O_2 and other biologically relevant ROS. Moreover, the fluorescence change observed at an excitation wavelength of 300 nm upon addition of ROS was ratiometric. These data provide further evidence that H_2O_2-triggered conversion of boronates to phenols is a robust and versatile methodology for reaction-based H_2O_2 detection. The whole sensing procedure took only 1 min, enabling rapid detection of H_2O_2, which would be considerably advantageous in biomedical applications. The fluorescence intensity of the reaction system barely changed after 1 min, indicating that the reaction product is photostable.

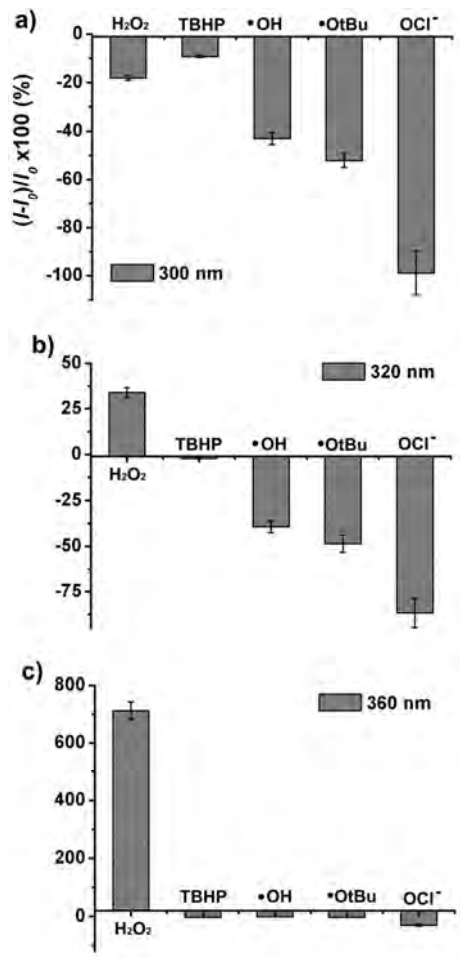

Figure 37. Fluorescence response of 10 μg mL^{-1} BPAN nanoparticle solution in the presence of H_2O_2 and other ROS excited at a) 300 nm, b) 320 nm, and c) 360 nm. Bars exhibit fluorescence changes after addition of each ROS(20 μM) compared with pristine BPAN nanoparticle solution. Data acquired at 25 ^{o}C in 20 mM HEPES, pH 7. Emission was collected between a) 320 and 500 nm; b) 340 and 500 nm; c) 380 and 500 nm. Values exhibit mean ±SD and each experiment was performed in triplicate.

Boronate reacts selectively with H_2O_2 to produce phenols, which are excellent metal-binding groups often incorporated into multidentate ligands [81]. To investigate the use of BPAN nanoparticles as a prochelator of metal ions, BPAN nanoparticles at a concentration of 10 μg mL^{-1} were reacted with 50 μM H_2O_2. Table 5 summarizes the quantity of residual metal ions after interaction between the resulting HPAN nanoparticles and Fe^{3+}, Cu^{2+}, and Zn^{2+}. The binding ability of the HPAN nanoparticles was in the order of $Fe^{3+} > Cu^{2+} > Zn^{2+}$. At low concentrations of Fe^{3+}, all metal ions were bound with the HPAN nanoparticles, whereas approximately 70% of the Fe^{3+} ions were removed by the HPAN nanoparticles at high concentrations of Fe^{3+}. The binding constant of HPAN nanoparticles for several metal ions was determined by a series of competition experiments in aqueous solution at pH 7.4. Fe^{3+} and Cu^{2+} affinities were measured by spectrophotometric titration with the competing chelator ethylenediaminetetraacetic acid (EDTA). Increasing concentrations of HPAN added to a solution of [Fe-EDTA] and [Cu-EDTA] result in an increase of the absorbance at 341 nm and 355 nm, respectively. The calculations of binding constants were log K'=20.23 for Fe^{3+} and log K'=14.94 for Cu^{2+} at pH 7.4. Additionally, the binding constant of the HPAN for Zn^{2+} was calculated by competitive binding experiment with 4-(2-pyridylazo)resorcinol). The binding affinity of the HPAN

nanoparticles for Zn^{2+} was calculated to log K'=7.13. Judging from these data, the BPAN nanoparticles may play a future role as a prochelator of Fe^{3+} and other metal ions to prevent iron-promoted ·OH generation.

Table 5. Removal of metal ions using HPAN nanoparticles.

Fe^{3+} (ppm)	Inhibition (%)	Cu^{2+} (ppm)	Inhibition (%)	Zn^{2+} (ppm)	Inhibition (%)
3.74	100	3.74	90.10	3.74	64.43
10.24	90.82	10.24	48.46	10.24	28.33
51.20	70.47	51.20	16.96	51.20	5.59

To investigate the *in vitro* application of BPAN nanoparticles, microscopic images were made of RAW264.7 cells incubated with 5 and 10 μg mL^{-1} BPAN nanoparticles (Figure 38a and b; left column). Cells with BPAN nanoparticles had no considerable change in cell shape. Blue fluorescence from the BPAN nanoparticles was observed both inside and outside the cells. These macrophages produce superoxide upon stimulation with phorbol-12-myristate-13-acetate (PMA), and superoxide is known to be degraded to H_2O_2 by superoxide dismutase or by spontaneous dismutation [77]. Consequently, BPAN-treated cells were stimulated with 1 μg mL^{-1} PMA for 20 min (Figure 38a and b; right column). The cells treated with PMA exhibited high fluorescence, while macrophages not stimulated with PMA displayed only weak intracellular fluorescence. The mean fluorescence intensity values differed by a factor of *ca.* 4–5 (Figure 38a and b; right graph). The blue-fluorescent BPAN nanoparticles were capable of visualizing endogenous H_2O_2 generation in RAW264.7 cells due to efficient electron transfer after reaction with H_2O_2; the fluorescence from the Schiff base on the HPAN nanoparticles appeared with 360-nm excitation, while the fluorescence from 300-nm excitation decreased. In general, confocal microscopy has a blue filter (ex: 360 nm; em: 457 nm), which is adoptable for this experiment. Judging from these experiments, the BPAN

nanoparticles are taken up by the cells and are nontoxic, as well as capable of detecting elevation in H_2O_2 levels under conditions of oxidative stress. The BPAN nanoparticles are sensitive enough to image H_2O_2 produced in RAW264.7 macrophages. This result is consistent with the findings of Abo *et al*. that monoboronate reporters are capable of detecting H_2O_2 in PMA-treated macrophages [78].

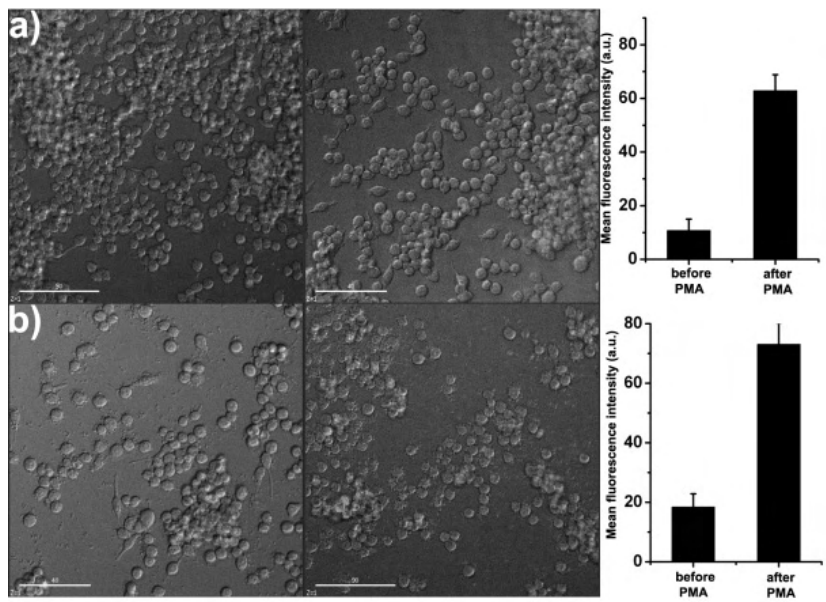

Figure 38. Live cell differential interference contrast (DIC) BPAN-treated RAW264.7 cells (a) 5 and b) 10 μg mL^{-1}); left images are before treatment of PMA and right images are 10 min after treatment of 1 μg mL^{-1} of PMA. Scale bars = 50 μm; Mean fluorescence intensity (MFI) values of BPAN-treated RAW264.7 cells (a) 5 and b) 10 μg mL^{-1}); left bar represents before treatment of PMA and right bar indicates 10 min after treatment of 1 μg mL^{-1} of PMA.

Cellular uptake efficiency of the nanoparticles was evaluated by flow cytometry analyze (Figure 39). FITC-modified PAN nanoparticles were used for this experiment due to the restriction of flow cytometry laser wavelength. RAW264.7 cells were incubated with 10 and 100 μg mL^{-1} nanoparticles for 24 h. Individual intracellular fluorescence intensities were measured via flow cytometry and averages were taken over 10,000 fixed cells to produce an averaged intracellular fluorescence curve. High internalization ratio of the nanoparticles was observed such as 98.8% and 99.7% for 10 and 100 μg mL^{-1}, respectively. Additionally, fluorescence median values increased from 30 for negative control to 648 and 9282, which indicated the intracellular particles increased with increment with the nanoparticle concentration.

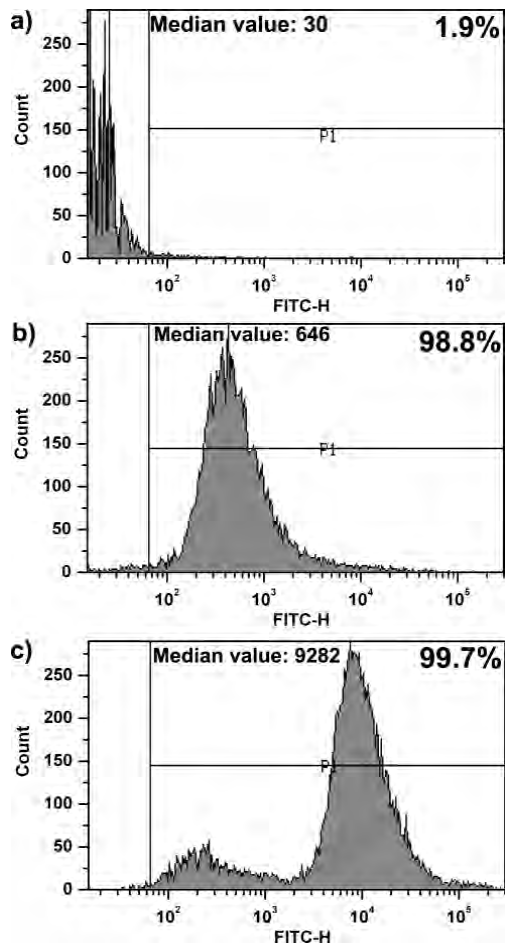

Figure 39. Flow cytometry analyzes of particle uptake. Quantification of cellular uptake of a) negative control, b) 10 μg mL^{-1} and c) 100 μg mL^{-1} FITC-modified PAN nanoparticles. Upper right values mean the number of nanoparticle-contained PC-12 cells and upper left median values indicate the amount of uptaken nanoparticles.

The viability of RAW264.7 cells with BPAN nanoparticles was determined *in vitro* (Figure 40). To evaluate the number of viable cells, a highly sensitive luminescence assay was conducted based on determination of the adenosine triphosphate (ATP) concentration. The level of ATP production in PAN nanoparticle- and BPAN nanoparticle-treated cells showed no significant decrease compared to a negative control. At a high concentration of nanoparticles (500 μg mL^{-1}), the viability was greater than 80%. To test whether the nanoparticles were generating ROS, we stained PAN- and BPAN-nanoparticle-treated cells for 24 h with DCF-DA. In the presence of ROS, DCF-DA is promptly oxidized to DCF, resulting in an increase in fluorescence from the cells. As shown in Figure 40, the ROS values are dose-dependent. ROS production was not significantly higher in treated than in untreated cells, and H_2O_2 was less than 0.02%. Therefore, the BPAN nanoparticles are an effective intracellular H_2O_2 detector without significant ROS production. Judging from these data, PAN and BPAN nanoparticles provide ratiometric and selective H_2O_2/ROS detection with low toxicity.

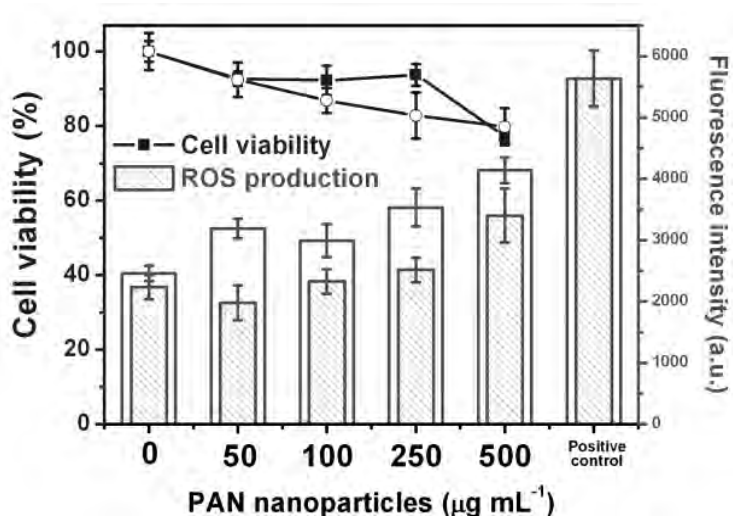

Figure 40. Viability of RAW264.7 cells incubated with PAN (closed squares) and BPAN nanonanoparticles (open circles) for 24 h. The viability was calculated relative to negative control. ROS production by RAW264.7 cells after being incubated with PAN (closed bars) and BPAN nanoparticles (open bars). H_2O_2 (0.02%) was used as positive control. Values exhibit mean ± SD and each experiment was performed in triplicate.

3.4 Cytotoxicity of PEDOT nanomaterials

3.4.1 Fabrication of shape-controlled PEDOT nanomaterials

PEDOT nanomaterials of three different shapes were fabricated by reverse (water-in-oil) micelle systems. This synthetic method allows precise control of the shape of 1D PEDOT nanomaterials by tuning the experimental parameters, such as the amounts of oxidizing agent and surfactant, type of solvent, and polymerization temperature [57,82]. Figure 41 shows the TEM images of PEDOT nanomaterials prepared with different amounts of aqueous $FeCl_3$ solution. On increasing the amount of this solution, the morphology of the PEDOT nanomaterials evolved from PEDOT-1 to PEDOT-2 and PEDOT-3 (Figure 41a–c). Importantly, the diameters of PEDOT-1 and PEDOT-2 (55±20 nm) were similar to the wall thickness of PEDOT-3 (50±10 nm), and this makes them suitable for a shape dependence study.

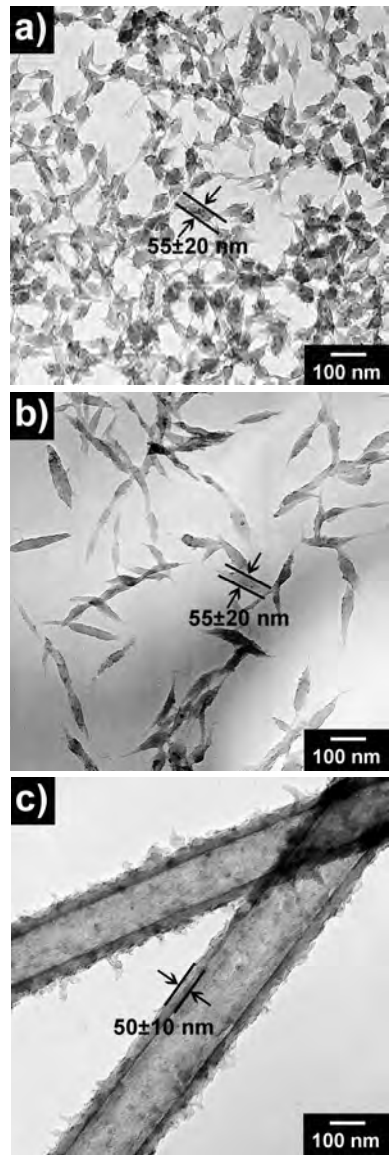

Figure 41. TEM images of PEDOT nanomaterials of three different shapes (width: 55±20 and 50±10 nm): a) PEDOT-1, b) PEDOT-2, and c) PEDOT-3.

The characteristics of the synthesized 1D PEDOT nanomaterials, including the aspect ratio, zeta potential, and conductivity, are summarized in Table 6. The surface charge of PEDOT nanomaterials was found to be negative, and the zeta potential increased with increasing aspect ratio of the nanomaterials [83]. The aspect ratio varied from about 1.3 to 4.5 and 25.0, and the morphology of the nanomaterials evolved from ellipsoids into rods and tubes. The resulting PEDOT nanomaterials were p-doped with anionic counterions, and their conductivity values were 35, 80, and 250 S cm^{-1} for PEDOT-1, PEDOT-2, and PEDOT-3, respectively. The conductivity was measured on pressed pellets consisting of numerous nanomaterials. The conductivities of the 1DPEDOTnanomaterials were higher than those of bulk PEDOT (10^{-3}–10^{0} S cm^{-1}) prepared with the identical oxidizing agent in an aqueous phase.

Table 6. Major characteristics of PEDOT nanomaterials.

Samples	Diameter (nm)	Length (nm)	Average aspect ratio (L/D)	ζ– potential (mV)	Conductivity (S/cm)
PEDOT-1	55±20	70±25	~1.3	-29.25	35
PEDOT-2	55±20	245±45	~4.5	-27.73	80
PEDOT-3	55±10	1350±140	~25.0	-20.18	250

3.4.2 Cytotoxicity and immune response of PEDOT nanomaterials

Figure 42 represents the cell morphology of IMR90 and J774A.1 cells treated with the PEDOT nanomaterials at a concentration of 10mg mL^{-1} for 24 h. There was no significant change in the morphology of these cells upon treatment with the nanomaterials. The PEDOT nanomaterials were mostly observed on the surface of the cells. Some blebs appeared on the surface of IMR90 cells and a small amount of PEDOT nanomaterial was taken up into J774A.1 cells due to phagocytosis. However, floating cells were barely found, which indicated that the nanomaterials had little effect on cell proliferation.

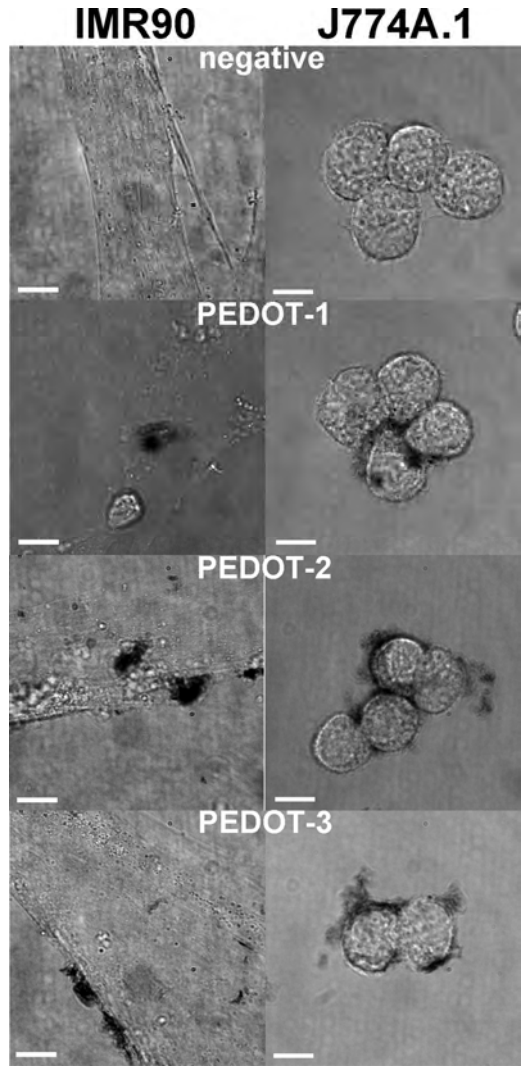

Figure 42. Microscope images of PEDOT nanomaterial-treated IMR90 cells and J774A.1 cells at concentration of 10 μg mL^{-1}; Scale bars = 10 μm.

The viability of cells treated with the PEDOT nanomaterials was evaluated in vitro using the IMR90 and J774A1 cell lines (Figure 43). The high sensitivity of a luminescence-based assay was employed to investigate the activity of the PEDOT nanomaterials. At a loading of 25 mg mL^{-1}, the nanomaterials induced no significant drop in the viability of both cell lines. When the PEDOT nanomaterial concentration was over 25 mg mL^{-1}, a drastic decrease in cell viability was observed. The production of ATP caused by PEDOT nanomaterials represented a shape-, concentration-, and time-dependent decrease in luminescence intensity on IMR90 and J774A.1 cells. This result was corroborated by the findings of Yen et al. that the cytotoxicity of gold and silver nanoparticles was size-dependent [84]. Although the difference in aspect ratio between PEDOT-1 and PEDOT-2 was only about 3.2, PEDOT-1 had a higher surface area than PEDOT-2. As a result, the cells treated with PEDOT-1 showed lower viability than those treated with PEDOT-2 over the entire range of nanomaterial concentration.

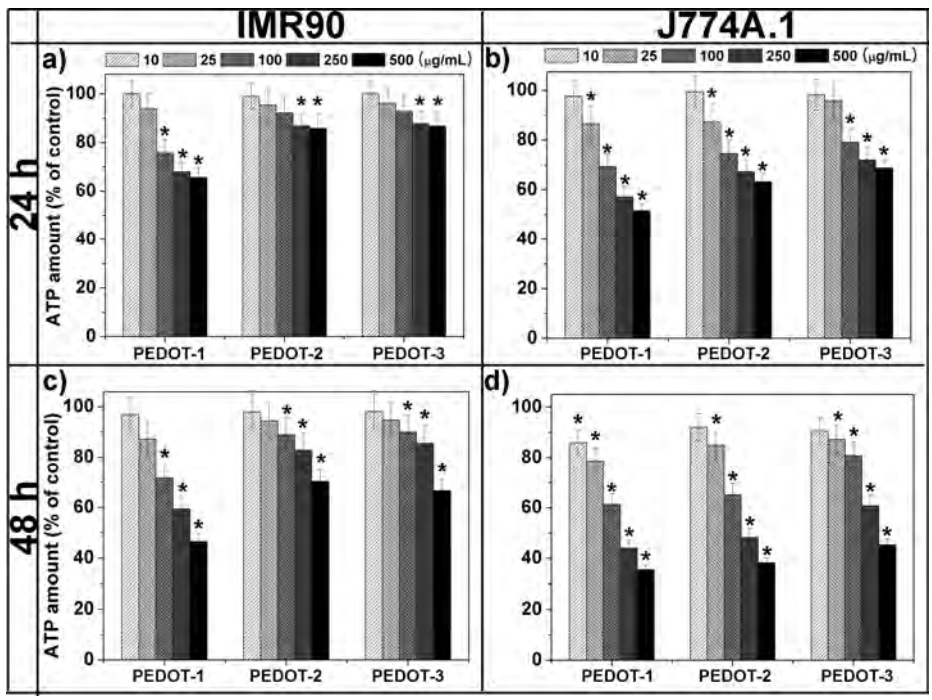

Figure 43. Viability of fibroblast (IMR90) and macrophage (J774A.1) cells in the presence of PEDOT nanomaterials, which was determined by the amount of ATP in the cells. IMR90 was incubated with PEDOT nanomaterials for a) 24h and c) 48h; J774A.1 for b) 24h and d) 48h. Values exhibit mean ± SD and each experiment was performed in triplicate. *Statistically significant difference from control exposed to PEDOT nanomaterials ($P<0.05$).

The cytotoxic effect of the PEDOT nanomaterials in IMR90 and J774A.1 cells is demonstrated in Figure 44. A fluorescence assay based on intracellular LDH release was used as a marker of membrane integrity, and thus it could be used for the measurement of cytotoxicity. There was no significant effect on cell proliferation for all samples at a concentration of 25 mg mL^{-1} after 24 h. The cytotoxicity increased with increasing concentration and treatment time of PEDOT nanomaterials. The cytotoxic effect of PEDOT-1 on cells was more pronounced than that of PEDOT-2 or PEDOT-3, thus indicating that the cytotoxicity of the PEDOT nanomaterials is shape-dependent. Several studies reported that lung fibroblasts and macrophages treated with nanomaterials showed significant cytotoxicity [85]. The cytotoxicity of single-walled carbon nanotubes (*ca*. 10–20 nm) toward macrophages was found to be about 50% at 10 mg mL^{-1} for 24 h. The cytotoxicity of gold nanoparticles (2–40 nm in diameter) ranged from 50 to70% at 10 mg mL^{-1} for 24 h. Under our experimental conditions, macrophages treated with the PEDOT nanomaterials at a concentration of 10 mg mL^{-1} revealed no cytotoxicity after 24 h. Judging from these data, PEDOT nanomaterials were less cytotoxic than the above-mentioned nanomaterials.

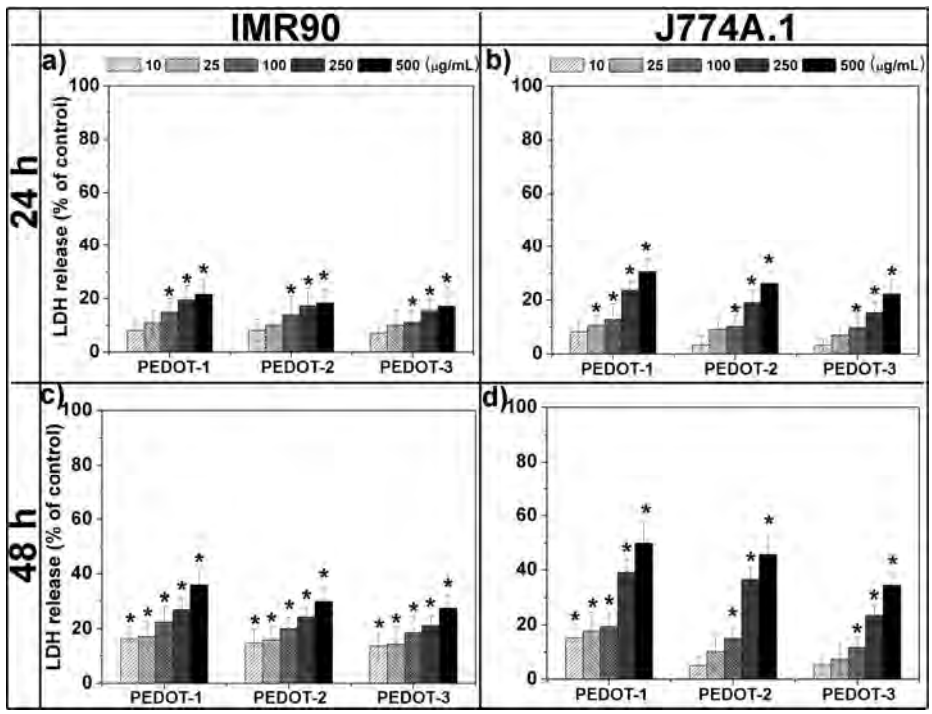

Figure 44. Cytotoxicity of fibroblast (IMR90) and macrophage (J774A.1) cells in the presence of PEDOT nanomaterials, which was determined by the amount of LDH release. IMR90 was incubated with PEDOT nanomaterials for a) 24h and c) 48h; J774A.1 for b) 24h and d) 48h. Values exhibit mean ± SD and each experiment was performed in triplicate. *Statistically significant difference from control exposed to PEDOT nanomaterials ($P<0.05$).

To verify the amount and mode of cell death, apoptosis and necrosis assays were conducted by FACSCalibur flow cytometry using aV and PI staining. Statistical results were obtained from the dot plots using WinMDIsoftware, based on the percentages of aV-/PI-(viable cells), and those with aV-/PI+ (necrotic cells), aV+/PI- (apoptotic cells), and aV+/PI+ (late apoptotic cells) in Figure 45. After summarizing the data for apoptotic and necrotic cells, a viability decrease from 90.39 in the control to 81.97, 83.08, and 87.06 was detected for IMR90 cells treated with PEDOT-1, PEDOT-2, and PEDOT-3, respectively. The decreased viability involved mainly late apoptosis. In the case of J774A.1, a drop in viable cells from 88.85 in the control to 71.01, 76.54, and 81.59 was shown upon treatment with PEDOT-1, PEDOT-2, and PEDOT-3, respectively. Early apoptosis and late apoptosis affected mostly the decreasing cell viability of J774A.1. Apoptosis and necrosis increased in inverse proportion to the decreasing aspect ratio. Figure 46 displays microscopy images of live cells treated with the PEDOT nanomaterials, in which the cells were stained with aV and PI. Unstained cells define viable cells, and green fluorescent labels/red fluorescent labels are classified as early apoptotic cells/necrotic cells. Dual-stained cells are categorized as late apoptotic cells. In the case of IMR90 cells, green fluorescent dots increased in inverse proportion to the aspect

ratio of the PEDOT nanomaterials. In particular, green fluorescent dots located mostly at blebs in IMR90 cells. On the other hand, green and red fluorescent dots appeared in each J774A.1 cell. The number of green and red dots increased with decreasing aspect ratio of the PEDOT nanomaterials. Some cells treated with PEDOT nanomaterials gathered together with a few cellular enlargements. This could be attributed to disorders in cytoskeletal functions as a result of PEDOT nanomaterial treatment [87].

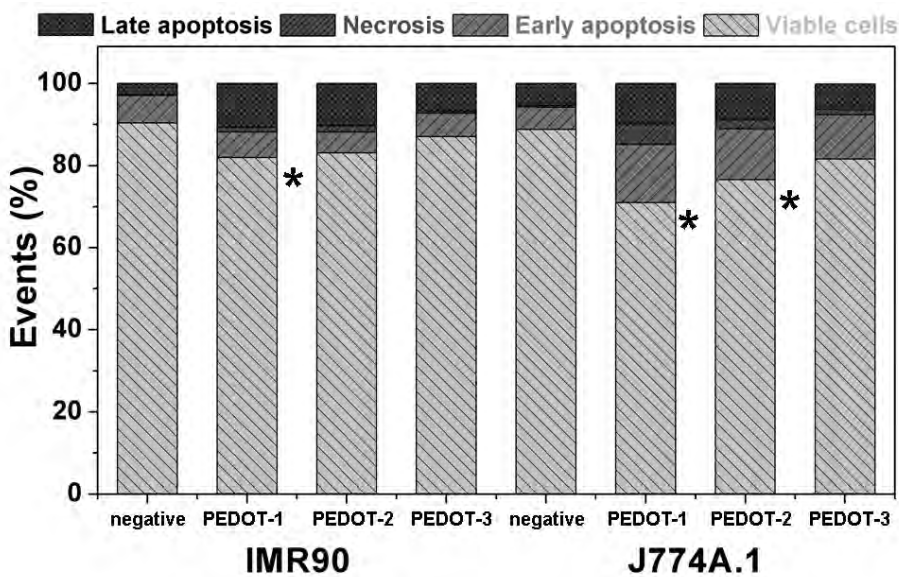

Figure 45. Apoptosis and necrosis ratio obtained from annexin V and PI staining. IMR90 and J774A.1 were incubated with PEDOT nanomaterials (25 μg mL^{-1}) for 24 h. Each experiment was performed in triplicate. *Statistically significant difference from control exposed to PEDOT nanomaterials ($P<0.05$).

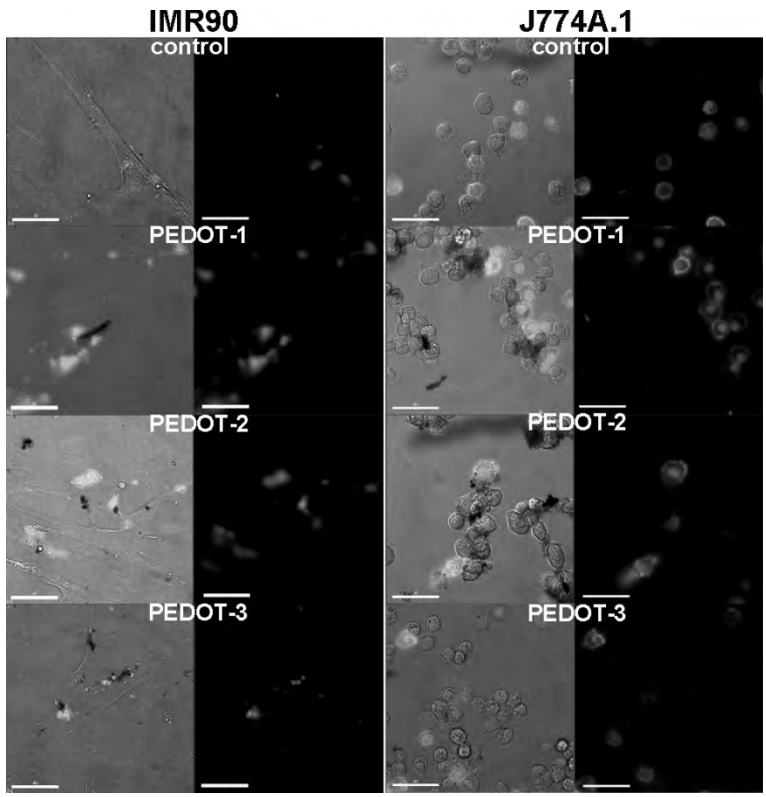

Figure 46. Live cell differential interference contrast (DIC) and fluorescent images of PEDOT nanomaterial treated IMR90/J774A.1 cells (25 μg mL^{-1}); negative control, PEDOT–1, PEDOT–2, and PEDOT–3. DIC images were taken at the same time corresponding to the cells. Green (aV) means apoptosis, red (PI) means necrosis. Scale bars = 40 μm.

The production of ROS induced by nanomaterials can damage external (membrane) or internal (after nanomaterial uptake) cells and can also contribute to inflammation [88]. To investigate the role of ROS in cells treated with the PEDOT nanomaterials, DCF-DA staining methods were performed after 24 h. In the presence of ROS, DCF-DA is rapidly oxidized to DCF, which results in an increase in the fluorescence intensity of the cells. ROS values were shape- and concentration-dependent (see Figure 47). It is known that ROS production and the following oxidative stress cause mitochondrial dysfunction. Judging from these results, PEDOT treatments on lung fibroblast and macrophage cells showed a decrease of cellular ATP content, membrane damage, and ROS generation, thus indicating the effect of nanomaterials on the mitochondrial respiratory chain [89]. In particular, ROS production of J774A.1 macrophages was much higher than that of IMR90 cells due to phagocytosis. In addition, ROS are known to initiate pro-apoptotic cell signaling [90]. The shape-dependent ROS production could be attributed to an increase in the apoptotic cells with respect to decreasing aspect ratio. The innate immune system consists of several cell types that are activated to recognition of nonself antigens via pattern recognition receptors and pathogen-associated molecular patterns resulting in eliciting various proinflammatory and cell-signaling molecules [84]. The release of three

proinflammatory mediators, interleukin-1 (IL-1), interleukin-6 (IL-6), and tumor necrosis factor a (TNF-a), was examined. These cytokines initiate inflammation and activate neighboring immune cells in the lung. It has previously been reported that nanoparticles induced cytokine release in the bronchiolar epithelium [91]. Under our experimental conditions, the proinflammatory response of macrophages to PEDOT nanomaterials was investigated by analyzing the induction of cytokines via the real-time polymerase chain reaction (PCR) of extracted RNA under lipopolysaccharide-free conditions.

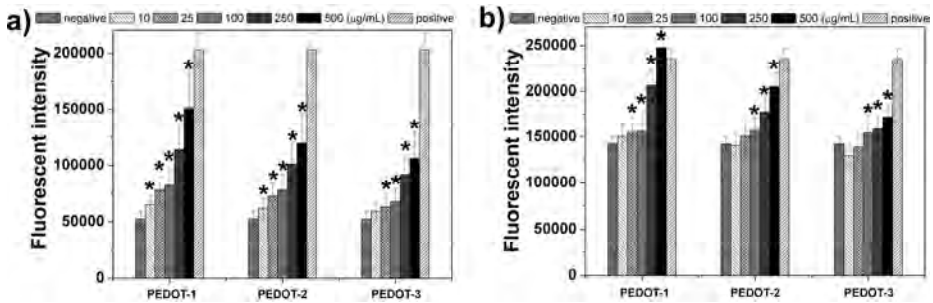

Figure 47. ROS production by a) IMR90; b) J774A.1 cells after incubation with PEDOT nanomaterials at 24 h. H_2O_2 (0.02%) was used as positive control. Values exhibit mean ± SD and each experiment was performed in triplicate. *Statistically significant difference from control exposed to PEDOT nanomaterials ($P<0.05$).

Figure 48 shows the proinflammatory gene expression of J774A.1 macrophages treated with the PEDOT nanomaterials both short term (6 h) and long term (24 h). In comparison to the control, PEDOT nanomaterials at a concentration of 25 mg mL^{-1} for 6 h generated an increase in proinflammatory cytokine release. This result demonstrated that macrophages interacted with PEDOT nanomaterials and consecutively activated the proinflammatory response. The TNF-α gene is expressed at the initial stage (*ca*. 2 h) in activated macrophages [92]. This can enhance other proinflammatory genes such as IL-1 and IL-6 [93]. After long-term incubation, the expression levels of cells treated with PEDOT-1 and PEDOT-2 diminished compared to those at the short term, in contrast to that of PEDOT-3. IL-1and IL-6 genes were down-regulated after treatment except with PEDOT-3 at 24 h. The expression of proinflammatory genes had little connection with the aspect ratio of the PEDOT nanomaterials, and thus further studies would be needed. Considering these data, PEDOT nanomaterials with different aspect ratios induce a proinflammatory response in macrophages.

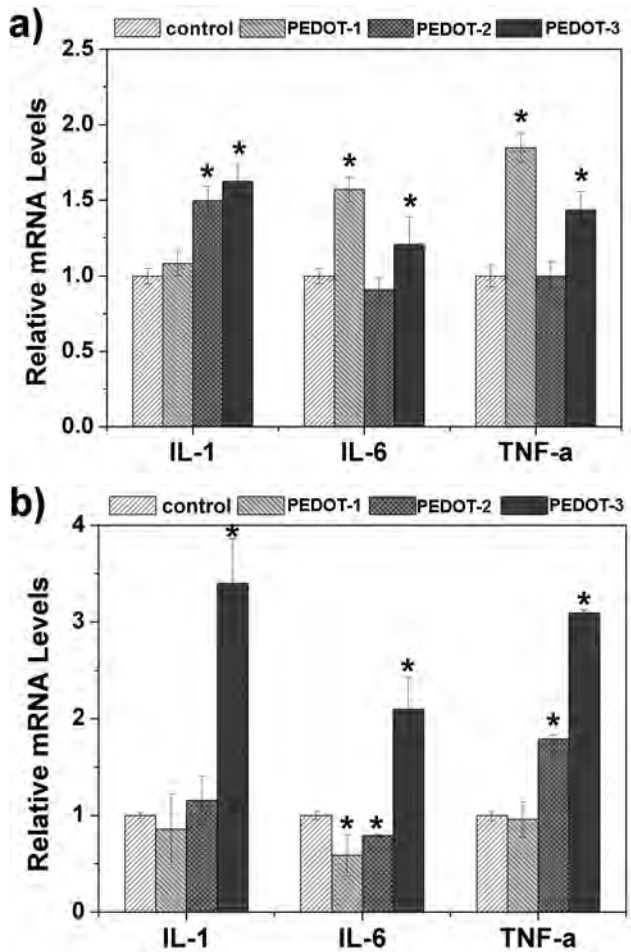

Figure 48. Gene expression of IL-1, IL-6, and TNF-α in J774A.1 macrophages incubated with culture medium containing PEDOT nanomaterials at 25 μg mL^{-1} for a) 6 and b) 24 h. Values exhibit mean ± SD and each experiment was performed in triplicate. *Statistically significant difference from control exposed to PEDOT nanomaterials ($P<0.05$).

3.5 Cytotoxicity of PPy nanoparticles

3.5.1 Fabrication of size-controlled nanoparticles

PPy nanoparticles of five different diameters were readily prepared via chemical oxidation polymerization as shown in Figure 49. The PPy nanoparticles were synthesized in PVA solution as a stabilizer and $FeCl_3$ as an initiator. The introduction of pyrrole monomer into the aqueous dispersion of PVA/$FeCl_3$ complex provided the formation of the PPy nanoparticles, leading to the production of the PPy nanoparticles with narrow size distribution. Figure 49 illustrates SEM images of the PPy nanoparticles with various diameters (termed: 20, 40, 60, 80, and 100 nm) and corresponding ELS histograms. The SEM images and ELS histograms revealed that the dispersity and diameter of the PPy nanoparticles were approximately 25±6 nm, 45±5 nm, 60±5 nm, 88±10 nm, and 112±20 nm, respectively. Precisely controlled PPy nanoparticles could be used to evaluate the size-dependent toxicity of nanoparticles. Size dependence of nanoparticles is one of the major factors that affect biokinetics and thus toxicity [94,95]. Therefore, it is noteworthy to investigate the cellular response using nanoparticles with different diameters.

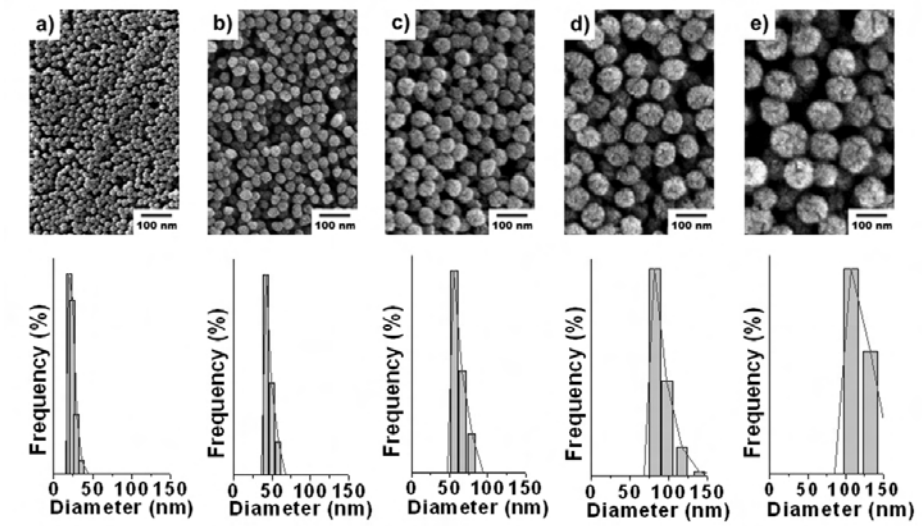

Figure 49. SEM images of the PPy nanoparticles with different diameters (below: size distribution histograms determined by ELS). The average diameters are about (a) 20, (b) 40, (c) 60, (d) 80, and (e) 100 nm, respectively.

3.5.2 Cellular uptake of PPy nanoparticles

Two cell lines (human lung fibroblast IMR90 cells and mouse alveolar macrophage J774A.1 cells) were chosen for investigating pulmonary nanotoxicity because inhalation was a major permeating route of nanomaterials [96,97]. From this point of view, in vitro toxicity evaluations of lung fibroblast and alveolar macrophage were suitable for understanding cellular response of nanomaterials.

The cellular uptake of these nanomaterials was observed by TEM (Figures 50 and 51). The PPy nanoparticles were monodisperse without aggregation in cell culture medium in TEM images (Figures 50b,e and 51b,e,d). It was considered that these PPy nanoparticles entered into cells using different routes. Fibroblasts are well known as representative non-phagocytic cells [98]. As shown in Figure 50d, plasma membranes were invaginated in order to internalize the PPy nanoparticles into IMR90 fibroblast cells. The invagination of the plasma membranes denotes the endocytosis of nanomaterials [99]. Therefore, the PPy nanoparticles were internalized via endocytosis in the IMR90.

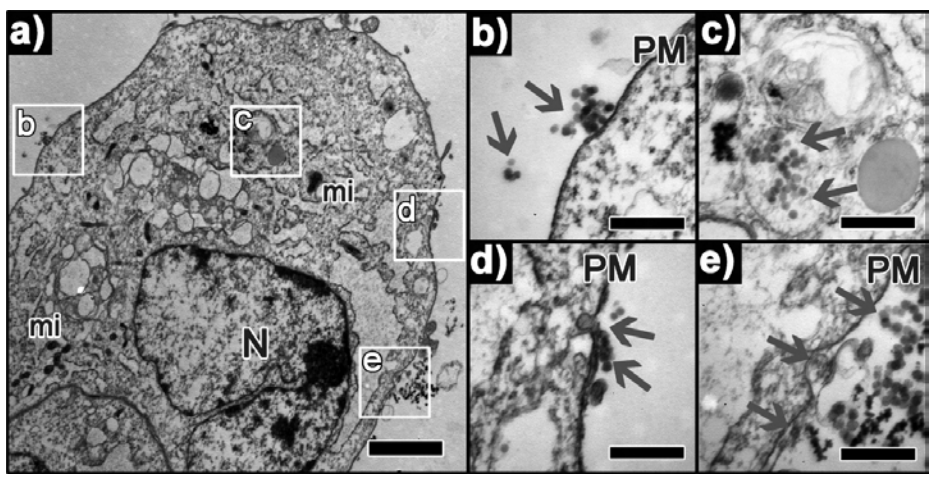

Figure 50. TEM images of the human lung fibroblast IMR90 cells incubated with 100 nm PPy nanoparticles for 24 h (25 μg mL^{-1}). (a) Overall IMR90 cell morphology (scale bar: 2 μm). (b-e) Higher magnification of the boxed area in (a) (scale bar: 500 nm). Red arrows indicate the PPy nanoparticles. (N, nucleus; mi, mitochondria; PM, plasma membrane)

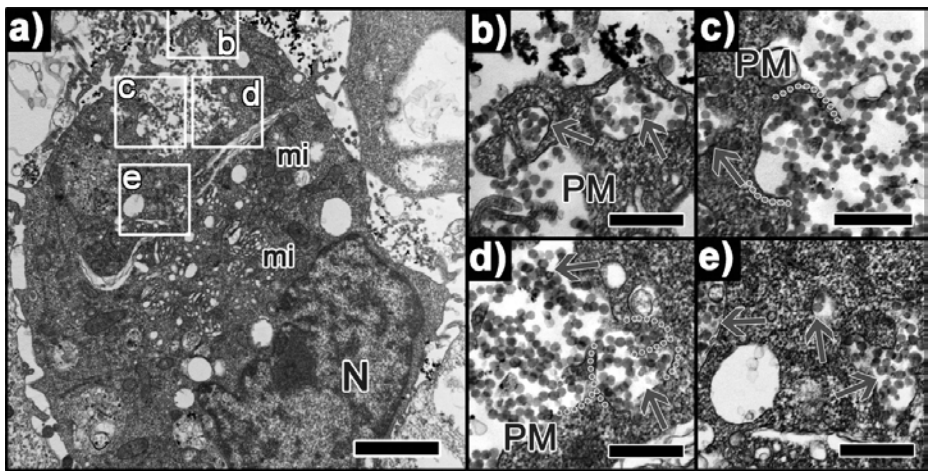

Figure 51. TEM images of the mouse macrophage J774A.1 cells incubated with 100 nm PPy nanoparticles for 24 h (25 μg mL^{-1}). (a) Overall J774A.1 cell morphology (scale bar: 2 μm). (b-d) Higher magnification of the boxed area in (a) (scale bar: 500 nm). Red arrows and greed doted lines indicate the PPy nanoparticles and the protrusion of the plasma membrane for phagocytosis, respectively. (N: the nucleus, mi: the mitochondria, and PM: the plasma membrane)

In the case of the J774A.1 macrophages, however, the protrusions of the plasma membrane (green doted lines in Figure 51c and d, 52) were observed as well as the invagination of the plasma membranes for uptake of the PPy nanoparticles. The plasma membrane protrusion for cellular uptake is one of the characteristics of phagocytosis [99]. Phagocytosis is typically restricted to specialized mammalian cells including macrophages, monocytes and neutrophils [100]. Considering these figures, the PPy nanoparticles were internalized into J774A.1 via both phagocytosis and endocytosis. In general, endocytosed materials were delivered from the plasma membrane to several organelles via multiple pathways [101]. In both cell lines, the PPy nanoparticles were found in endosomes (Figures. 51c and 52e), late endosome/multivesicular bodies (Figures 52d,e,h and j), and endolysosomes (Figure 52). Among various pathways, the data indicated that the most of internalized PPy nanoparticles were transported via endosome network which consist of early endosomes, multivesicular bodies/late endosomes, endolysosomes, and lysosomes. This result is consistent with cellular uptake model, suggested by Mu et al., for multiwalled carbon nanotubes [102]. The PPy nanoparticles did not penetrate into nor interact with the mitochondria or the nucleus. Furthermore, some PPy nanoparticles were observed in the lysosome. These findings suggest that the final destination of transported

PPy nanoparticles via endosome-network is lysosome. These results were consistent with other precedent researches [103,104].

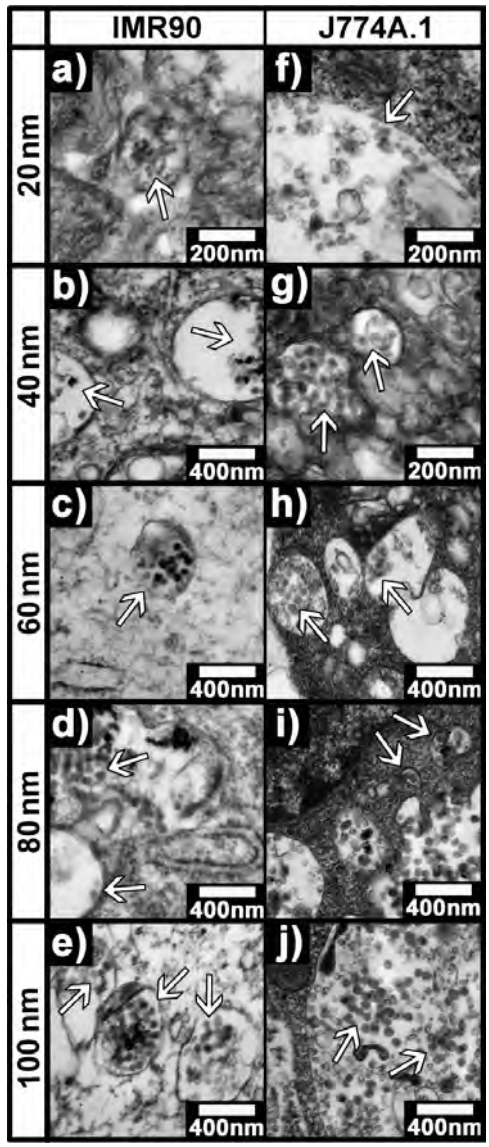

Figure 52. TEM images of (a-e) the human lung fibroblast IMR90 and (f-j) the mouse macrophage J774A.1 cells incubated with different diameters of the PPy nanoparticles for 24 h (25 μg mL^{-1}). White arrows indicate the PPy nanoparticles.

3.5.3 Cytotoxicity and innate immune response of PPy nanoparticles

Viability assays are essential steps in cytotoxicity that elucidate the cellular response to a toxicant. In order to estimate the number of viable cells after treatment of the PPy nanoparticles, luminescence-based ATP assay was conducted (Figure 53). The luminescence is originated from the change of luciferin to oxyluciferin by a luciferase in the presence of ATP. As a result, the luminescence intensity increases in proportion to ATP concentration in cells. In Figure 53, the production of ATP from PPy-treated cells was dose- and sizedependent. As the dose of the PPy nanoparticles increased, the cell viabilities decreased. The viability of PPy-treated macrophages was mostly lower than that of PPy-treated fibroblasts probably due to the phagocytosis of macrophages [105]. Although the viability of the J774A.1 was lower compared to that of the IMR90, the viabilities of the PPy-incubated cells showed over 80% at a concentration of 250 mg mL^{-1}. In the case of silver nanoparticles (6-20 nm), the viability in lung fibroblasts was about 70% at 200 mg mL^{-1} for 24 h [106]. The viability of macrophages treated with TiO_2 nanomaterials (30-40 nm) was ranged from 55 to 65% at 100 mg mL^{-1} for 24

h [107]. Judging from these data, the PPy nanoparticles were less cytotoxic than the aforementioned nanomaterials. In addition, the ATP production of 60 nm PPy-treated J774A.1 exhibited the lowest value than that of other PPy-treated cells although the overall cell viabilitywas in proportion of the diameter of the PPy nanoparticles. These data were in agreement with the results of Y. Yuan *et al*. that reported cytotoxic effects of hydroxyapatite nanoparticles were in order of 45 nm > 26 nm > 78 nm > 175 nm [96]. Several researches reported that particle size of *ca*. 50 nm was considered as the size of the best uptake efficiency [108,109]. Therefore, it could be considered that internalization efficiency affected the cell viability.

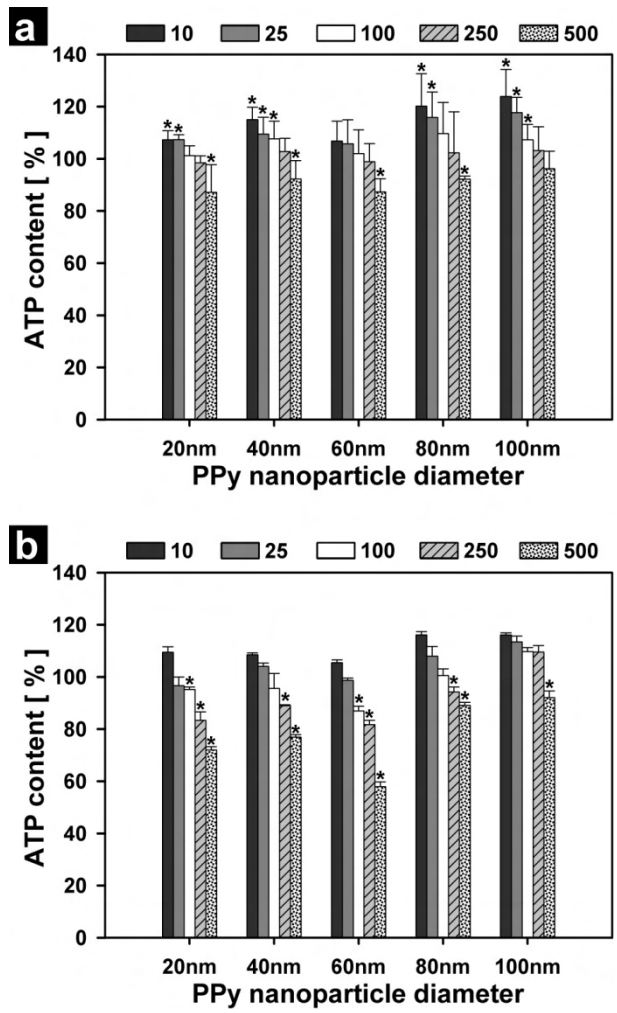

Figure 53. Viability of (a) the IMR90 and (b) the J774A.1 cells in the presence of the PPy nanoparticles, which was determined by the amount of ATP in the viable cells. Viability was calculated relative to untreated cells (a negative control). Values exhibit mean ± SD and each experiment was performed in triplicate. *Statistically significant difference from the control exposed to the PPy nanoparticles ($P<0.05$).

Among various cytotoxicity methods, ROS generations are considered as exemplary mechanism for nanotoxicity [97]. ROS are known to stimulate inflammation aswell as to initiate pro-apoptotic cell signaling [110]. Under normal condition, ROS are generated at low frequency and are readily neutralized by antioxidant defenses system such as glutathione (GSH) and antioxidant enzymes. On the other hand, the neutralization systems may be overwhelmed under a condition of excess ROS production and a large amount of GSH is converted to oxidized glutathione (GSSH). Consequently, drop in the GSH/GSSH ratio causes the cellular protective or injurious response [111]. At higher levels of oxidative stress, this protective response is overtaken by inflammation and cytotoxicity [111]. Under our experimental conditions, DCF-DA assay was performed to detect ROS in the cells treated with the PPy nanoparticles for 24 h. In the presence of ROS, nonfluorescent DCF-DA was oxidized, and then, it was transformed into fluorescent DCF. The generated ROS from the cells can be estimated by the quantifying fluorescent intensity of DCF. Figure 54 represented the value of the ROS as functions of the PPy nanoparticle amount and size on both the cell lines. In the case of particle diameter, 60 nm PPy nanoparticles evoked more noticeable level of ROS than other PPy nanoparticles, and it could be also corroborated by viability results. Furthermore, the size and dose dependence

of the ROS production were well matched to the cell viability values. The ROS value of 60 nm PPy-treated J774A.1 revealed 58% at a concentration of 500 mg mL^{-1} and this value was much higher than that of any other PPy-treated cells due to phagocytosis.

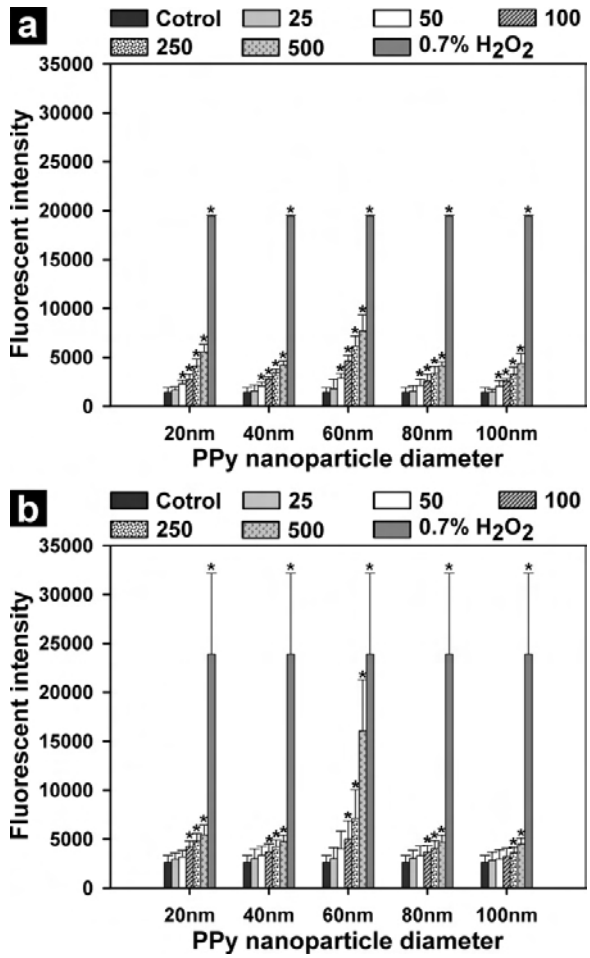

Figure 54. ROS production by (a) the IMR90 and (b) the J774A.1 cells after being exposed to different diameter of the PPy nanoparticles for 24 h. Intercellular ROS were measured using a DCF-DA staining and H_2O_2 (0.7%) was used as a positive control. Untreated cells were considered as a negative control. Values exhibit mean ± SD and each experiment was performed in triplicate. *Statistically significant difference from the negative control exposed to the PPy nanoparticles ($P<0.05$).

Innate immune system is the nonspecific mechanism that defends the human body from pathogens, and it initiates a specific adaptive immune response through antigen presentations [112]. Among the first immune cells, macrophages work on a site of invasion, have contact with foreign agents through Toll-like receptors, and trigger the inflammation. Macrophages have three major functions in inflammation; phagocytosis, antigen presenting, and production of various cytokines and growth factors [113]. These play key roles in the initiation, maintenance, and selectivity of inflammation. In addition, the innate immune response is a direct correlation between the cell viability, ROS-generating, and apoptosis [111]. Therefore, the evaluation of inflammatory response in alveolar macrophages is of importance in nanotoxicological assessments.

In the absence of stimuli, the major states of macrophages are immature. Detecting the foreign agents through phagocytosis, immature macrophages are transformed into mature state. And then, the macrophages express various markers on their surface for triggering the sequential immune process. In particular, CD40, CD80, and CD86 are known to the most important costimulatory molecules for T-cell activation [107]. CD40 expresses on macrophages and interacts with CD154 on the T-cell, which is one of the first steps in T-cell activation. As a consequence of this initial

interaction, interaction between CD28 on the T-cell and CD80 and CD86 expressed on activated macrophages is induced [112]. These molecules play a role to enhance and sustain the T-cell activation signals. The expressed levels of the costimulatory markers (CD40, CD80, and CD86) were quantified using FITC-conjugated antibodies and flow cytometric measurement (Figure 55). Figure 55 represented the expression of CD40, CD80, and CD86 on the J774A.1 incubated with 25 $mgmL^{-1}$ PPy nanoparticles for 24 h. The expression levels of the CD40 and the CD80 were slightly upregulated except the CD40 of 100 nm PPy nanoparticle treatment compared to the control (Figure 55a and b). In Figure 55c, the expression levels of the CD86 exhibited down-regulated in sizes of between 40 nm and 80 nm. It is known that CD40 and CD80 are involved in Th1 response while CD86 is related in Th2 responses [114]. Judging from these results, immune regulatory signals induced by the PPy nanoparticles were mainly Th1 responses. Furthermore, these results did not indicate size dependence of the PPy nanoparticles in contrast to the viability and the ROS values.

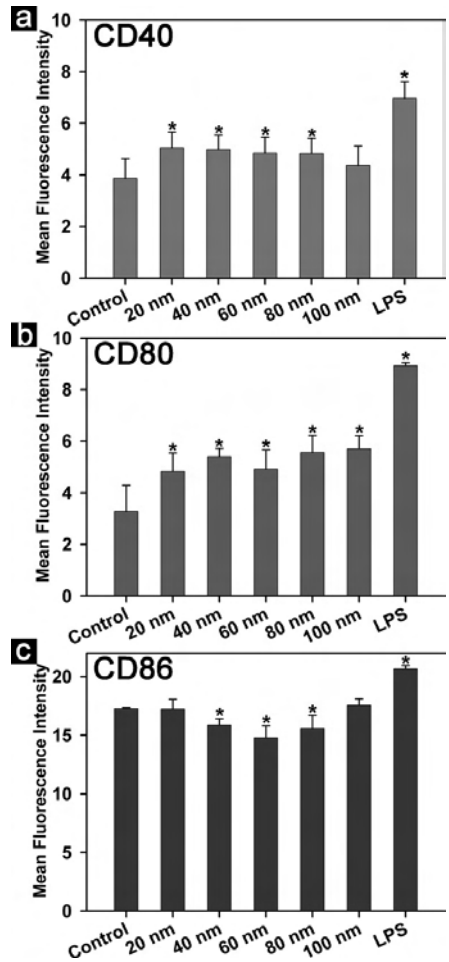

Figure 55. Expression of costimulatory markers (a) CD40, (b) CD80, and (c) CD86 on the J774A.1 cells incubated with 25 μg $mL^{-1}$of the PPy nanoparticles after 24 h. Treated cells were stained with FITC-conjugated antibodies and analyzed by flow cytometry. LPS (0.25 μg mL^{-1}) and FITC conjugated Rat IgG2a, κ isotype control antibody incubated cells were used as a positive control and an isotype control, respectively. Free of the PPy nanoparticles in the cells was considered as a negative control. Each experiment was carried out in triplicate. *Statistically significant difference from the negative control exposed to the PPy nanoparticles ($P<0.05$).

Cell death mechanism was classified into two categories. One is apoptosis and the other is necrosis [115]. In apoptotic cells, PS is translocated from inner (cytoplasm, normal state) to outer (cell surface, apoptotic state) leaflet of the plasma membrane. Exposed PS was detected with Alexa Fluor-488 conjugated aV, which played a role of apoptosis marker. PI that was utilized to detect loss of the membrane integrity was employed for identifying necrotic cell death [116]. Using properties of aV and PI, early apoptosis, late apoptosis, and necrosis can be verified. In order to quantify the categorized cell death, aV/PI assays were performed by FACSCalibur flow cytometry. Statistical results were acquired from the dot plots using WinMDI software, based on the percentages of aV-/PI- (viable cells), and those with aV-/PI+ (necrotic cells), aV+/PI- (early apoptotic cells), and aV+/PI+ (late apoptotic cells). As shown in Figure 56a, amount of viable cells decreased from 83 (untreated cells) to 69.3, 74.5, 64.3, 75.5 and 77.7 in the IMR90 treated with 20 nm, 40 nm, 60 nm, 80 nm, and 100 nm PPy nanoparticles, respectively. In the case of the J774A.1 (Figure 56b), percentage of viable cells was declined from 91.2 (untreated cells) to 68.8, 74.4, 62.2, 76.8 and 76.7 at 24 h, with increasing the diameter of the PPy nanoparticles. The ratio of live cells after treatment of the PPy nanoparticles was also showed in order of 100 nm > 80 nm > 40 nm > 20 nm > 60 nm.

These results were consistent with those of the viability and the ROS assay. However, the reasons of cell death in two cell lines were different. The decreased viability in IMR90 was mostly due to apoptosis (early apoptosis and late apoptosis). In contrast, the viable J774A.1 decreased mainly because of necrosis.

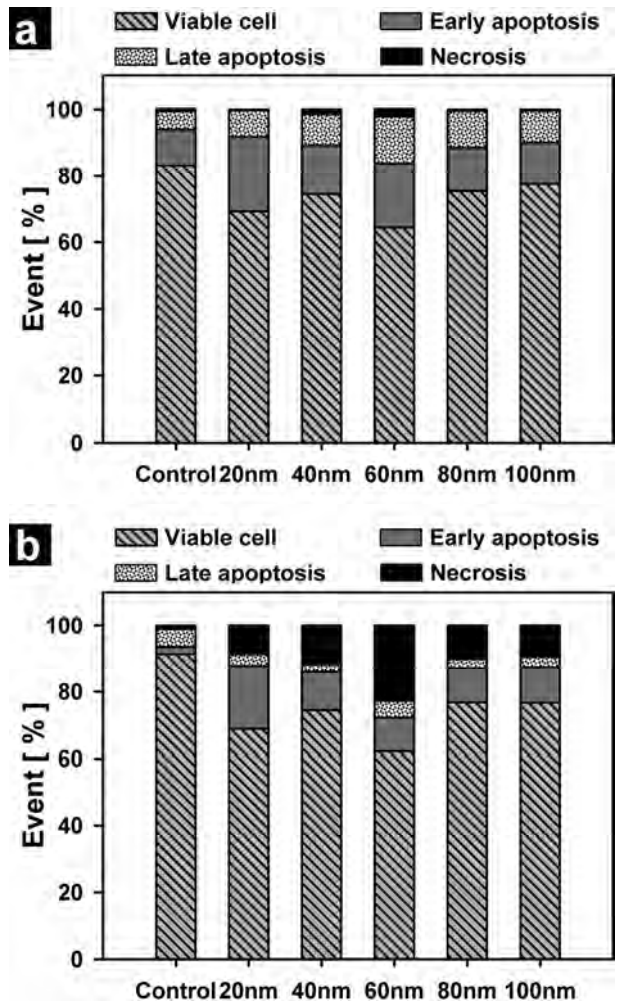

Figure 56. Apoptosis and necrosis ratio obtained by aV and PI double staining and measured by flow cytometry. (a) The IMR90 and (b) the J774A.1 cells were treated with the PPy nanoparticles for 24 h (25 μg mL^{-1}). Free of the PPy nanoparticles in the cells was used as a negative control. Each experiment was performed in triplicate.

Figure 57 exhibits microscopy images of live cells treated with the PPy nanoparticles in which the cells were stained with aV/PI. Unstained cells were presented viable cells, and green fluorescent labels/red fluorescent labels are categorized as early apoptotic cells/necrotic cells. Dual-stained cells are meant as late apoptotic cells. In both of the cell lines, green and red fluorescent dots increased in inverse proportion to the size of the PPy nanoparticles, except 60 nm PPy nanoparticles. Cell death was most triggered by 60 nm PPy nanoparticles than any other size of the PPy nanoparticles (Figure 57c and h). Figure 57a-e shows that green fluorescent dots located mostly at blebs in the IMR90 cells. Blebs on the plasma membrane were one of the characteristics to identify apoptosis. Therefore, as confirmed by FACS analysis, cell death in the IMR90 was mainly originated from early apoptosis. In the J774A.1, however, these images are not enough to determine which cause the cell death, late apoptosis or necrosis (Figure 57fej). Even so, one thing that we take notice is red fluorescent dots increased in the J774A.1 compared with in the IMR90, which is partly agreed with the FACS analysis. Considering these data, the apoptosis and necrosis in PPy-treated cells were size- and cell type-dependent, and especially 60 nm PPy-treated cells were the most toxic in PPy-treated cells.

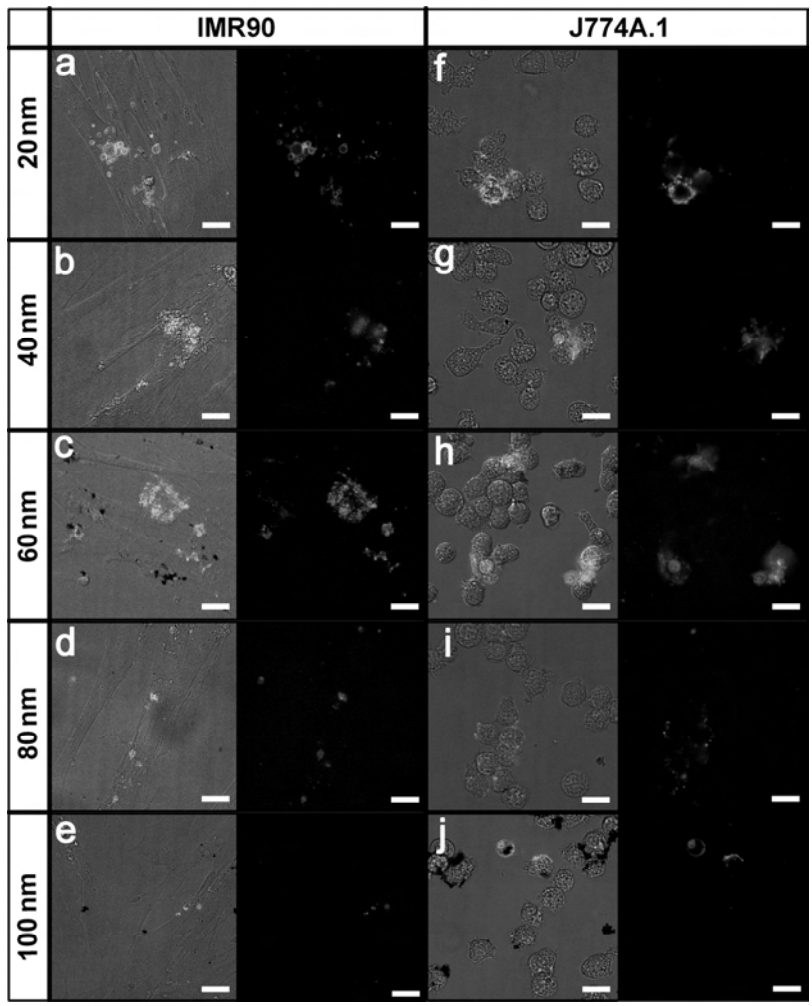

Figure 57. Live cell differential interference contrast (DIC) and fluorescence images of the PPy-treated (a-e) IMR90 and (f-j) J774A.1 cell (25 μg mL^{-1}). The cells were double stained with aV (green) and PI (red) for detection of apoptosis and necrosis. From up to the bottom, diameters of the PPy nanoparticles are (a, f) 20, (b, g) 40, (c, h) 60, (d, i) 80, and (e, j) 100 nm, respectively. DIC images were taken at the same time, corresponding to the fluorescence images. (Scale bars: 20 μm)

3.6 Cytotoxicity of PANi nanoparticles

3.6.1 Fabrication of PANi nanoparticles

Four different shape PANi nanomaterials, termed PANi–1, PANi–2, PANi–3, and PANi–4, were employed to prepare cytotoxicity tests. FE–SEM images (Figure 58) displays PANi nanomaterials prepared with different weight ratio of PVP/aniline. On increasing the ratio of PVP/aniline (from 0 to 1.6 wt%), the morphology of the PANi nanomaterials evolved from nanorods (PANi–4) to nanobeads (PANi–1). These materials gave a unique opportunity to investigate the shape dependence of the cytotoxicity of PANI materials.

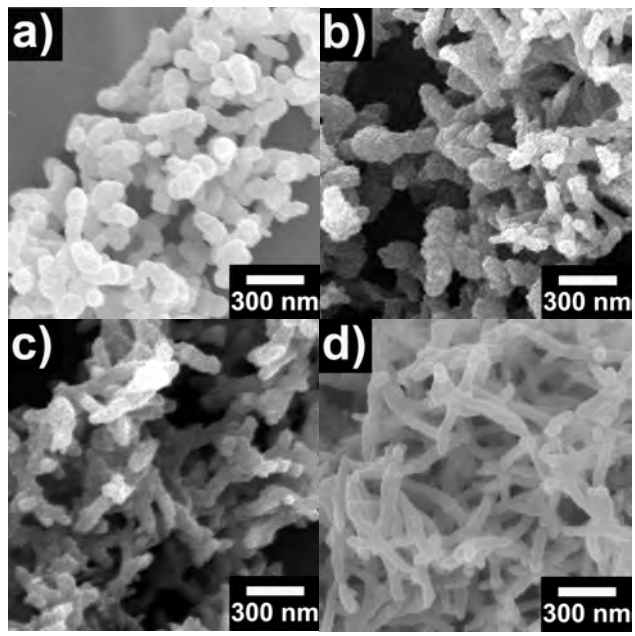

Figure 58. FE–SEM images of PANi nanomaterials with increasing aspect ratio: (a) PANi–1 (2.09), (b) PANi–2 (2.94), (c) PANi–3 (3.92), and (d) PANi–4 (5.35).

The characteristics of the synthsized PANi nanomaterials, including aspect ratio, zeta potential, and conductivity, are summerized in Table 7. The average aspect ratios were 2.09, 2.94, 3.92, and 5.35 for PANi–1, PANi–2, PANi–3, and PANi–4, respectively. The aspect ratio increasing of the PANi nanomaterials were also confirmed by zeta–potential measurements. The resulting values that mean the interparticle forces are the potential of practical interest in dispersion stability because it is measured at the notional boundary (slipping plane) of the nanomaterials [83]. The zeta–potential energy of PANI nanomaterials exhibits increasing from –4.15 to –1.43 with respect to aspect ratio increasing, which correlates to previous results [108]. The conductivity values of PANi nanomaterials were 11, 17, 23, and 29 S cm^{-1} for PANi–1, PANi–2, PANi–3, and PANi–4, respectively. The conductivities of the PANi nanomaterials were much higher than that of bulk (10^{-3}–10^{0} S cm^{-1}) as a control PANi material.

Table 7. Various properties of PANi nanomaterials.

PANi	Diameter (nm)	Length (nm)	Average aspect ratio (L/D)	ζ– potential (mV)	Conductivity (S/cm)
PANi–1	91 ± 8	190 ± 15	2.09	–4.15	11
PANi–2	80 ± 9	235 ± 21	2.94	–2.97	17
PANi–3	74 ± 9	290 ± 25	3.92	–1.75	23
PANi–4	71 ± 12	380 ± 39	5.35	–1.43	29

3.6.2 Cytotoxicity of PANi nanoparticles

Viability assays are essential in toxicological study to elucidate the cellular effect to a toxicant. In addition, knowledge of cell death, survival, and metabolic activities can be obtained from the viablity assays. The high sensitivity of luminescence–based assay and fluorescent–based assay on the cells were performed to investigate the viability and cytotoxicity of PANi nanomaterials. ATP assays to evaluate the adverse effect of PANi nanomaterials showed a shape–, concentration–, and time–dependent decrease in luminescence intensity on lung fibroblast cells (Figure 59). There was no significant change on cell viability below the concentration 25 μg mL^{-1} at 24 h, however, the cell viability slightly decreased at 48 h. The cell viability treatment by PANi nanomaterials at above the concentration 100 μg mL^{-1} decreased drastically at both 24 and 48 h. The adverse effect of low aspect ratio PANi nanomaterials to cells was more pronounced than that of high aspect ratio PANi nanomaterials. It is important to note that the result of PANi–4 was similar to that of bulk. As the nanomaterials become 1D structures, the size and aspect ratio increse, consequently, the surface effect could be smaller. A low ATP measurement relates to metabolic inhibition in cells, therefore, the ATP assay represents metabolic arrest rather than cell

death.

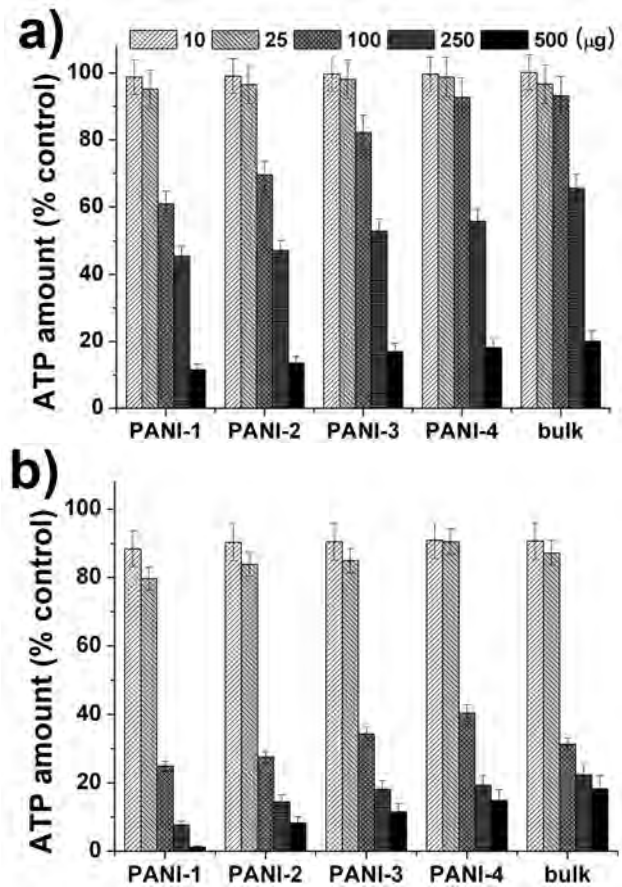

Figure 59. Cell viability obtained from luminescent assay for PANi nanomaterial treated human fibroblast cells determined by the amount of ATP in the cells; a) 24h, b) 48h incubation with PANI nanomaterials.

ATP depletion could damage the mitochondrial respiratory chain. The mitochondrial damage was measured by CellTiter Blue viability assay which detects the reduced dehydrogenase activity (Figure 60). Cell viabiliity shows a concentration–, shape–, and time–dependent decrease and are consistent with the ATP assay values. The viability dramatically diminished at high concentration (over 100 μg mL^{-1}) and decreased as the aspect ratio of PANi nanomaterials lowered. It is noteworthy that the toxicity of PANi nanomaterials were concentration–dependent. In the case of high concentration, agglomeration and subsequent precipitation of PANi nanomaterials could increase, leading to effect toxic on the cells.

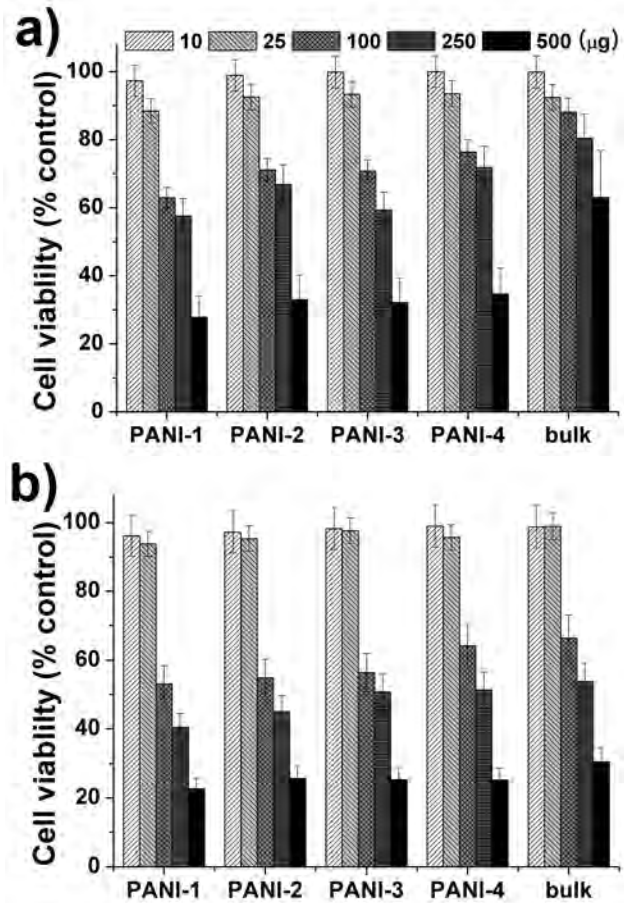

Figure 60. Cell viability obtained from CellTiter Blue assay for PANi nanomaterial treated human fibroblasts indicating metabolically active cells; a) 24h, b) 48h incubation with PANi nanomaterials.

LDH assay represents the effect of PANi nanomaterials on cell membrane intergrity (Figure 61). The integrity of their plasma membrane is sustained in live cells to maintain ion homeostasis over the surrounding media. The LDH places in the cytoplasm and releases to the surrounding medium with respect to the membrane damage. Therefore, the amount of LDH release is proportional to cell death. At 100 μg mL^{-1}, membrane leakage of LDH was 29, 27, 25, and 23% at 24 h, and 43, 39, 37, and 36% at 48 h, decreasing with increasing the aspect ratio of PANi nanomaterials. The lowest aspect ratio at the highest concentration (PANi–1 at 500 μg mL^{-1}) presented the most toxic effect as indicated by LDH measurements. This result was corroborated by the findings of Pan *et al*. that the cytotoxicity of gold nanoparticles was size-dependent [90]. As smaller nanoparticles were highly toxic and larger nanoparticles were comparatively nontoxic, low aspect ratio PANi nanomaterials also showed most cytotoxic mainly due to high surface area and particle number.

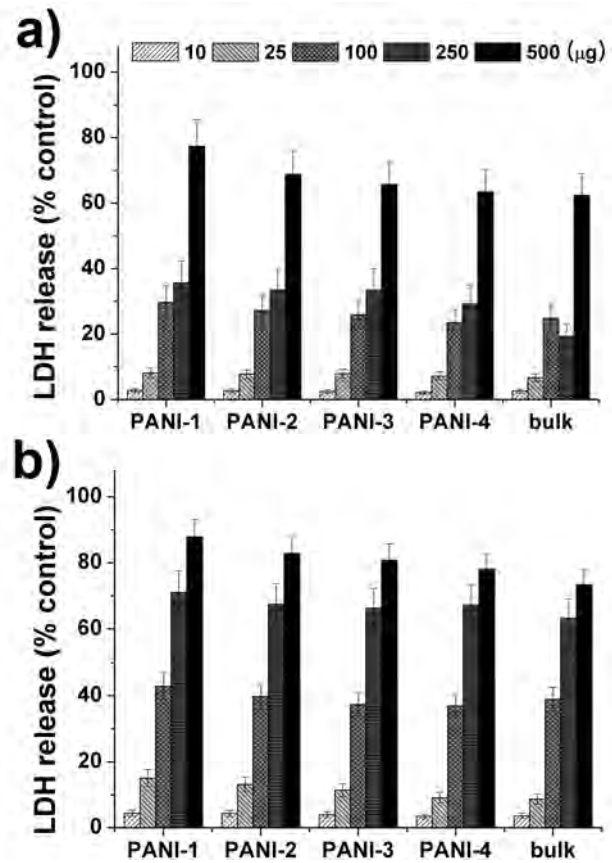

Figure 61. Cell cytotoxicity of PANi nanomaterials on human fibroblast cells determined by the amount of LDH release; a) 24h and b) 48h incubation with PANi nanomaterials.

IMR90 cells were double stained with green fluorescent aV conjugated FITC for cytoplasm as measuring of apoptosis and red fluorescent PI for nuclear as measuring of necrosis. Live cell fluorescent and DIC images display typical views of PANi nanomaterial treated IMR90 cells in Figure 62. Typical necrotic cells induced by 5 mM H_2O_2 as a positive control represent double positive (Figure 62a). Apoptosis and necrosis were more observed in PANi–1 and PANi–2 treated cells (Figure 62b, c) than those of PANi–3 and PANi–4 treated cells (Figure 62d, e). In the case of bulk, the toxicity was comparable of PANi–3 and PANi–4 treatment (Figure 62f).

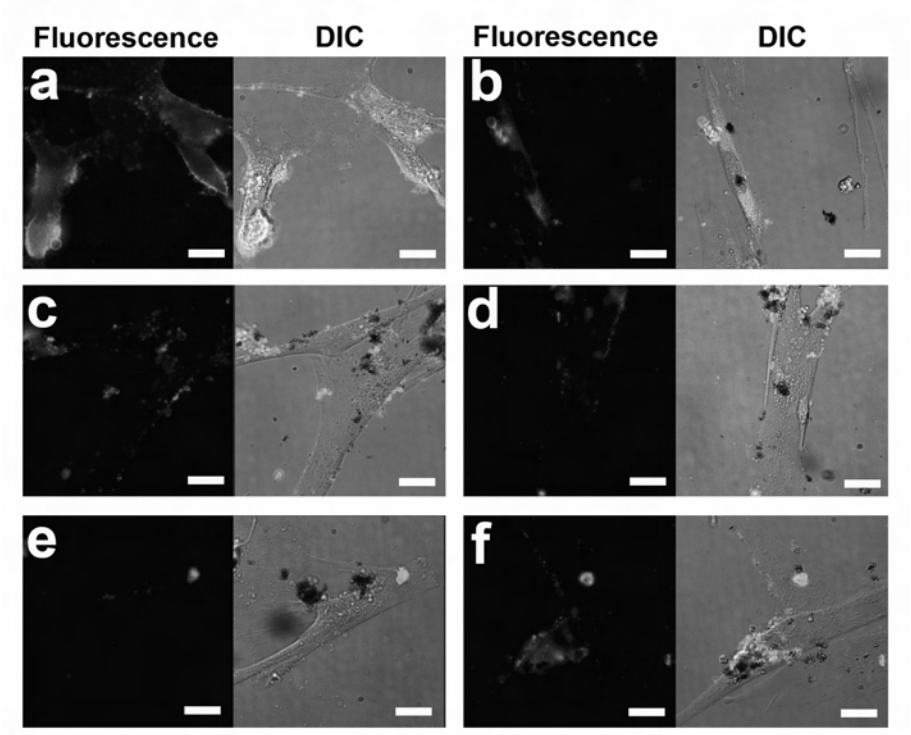

Figure 62. Live cell fluorescent and differential interference contrast (DIC) images of PANi nanomaterial treated IMR90 cells; a) positive control, b) PANi–1, c) PANi–2, d) PANi–3, e) PANi–4, and f) bulk. DIC images were taken at the same time corresponding to the cells in panels a–f. Green (annexin V conjugated FITC) means apoptosis, red (PI) means necrosis. Scale bars approximately 20 μm.

Figure 63 displays flow cytometric results of the relative amounts of live, necrotic, and apoptotic IMR90 cells treatment with PANi–1, PANi–2, PANi–3, PANi–4 and bulk. aV/PI double positive indicate necrotic cells, aV positive/PI negative are classified as apoptosis, aV/PI double negative define live cells. The values suggested that small percentage of the cells induced by PANi nanomaterials indicate apoptosis and necrosis. A decrease in the portion of necrotic cells from 13.96 to 3.56 was observed as the aspect ratio of PANi nanomaterials increased. In contrast, an increase in viability from 83.53 to 90.99 was detected in proportion to increasing PANi nanomaterial aspect ratio.

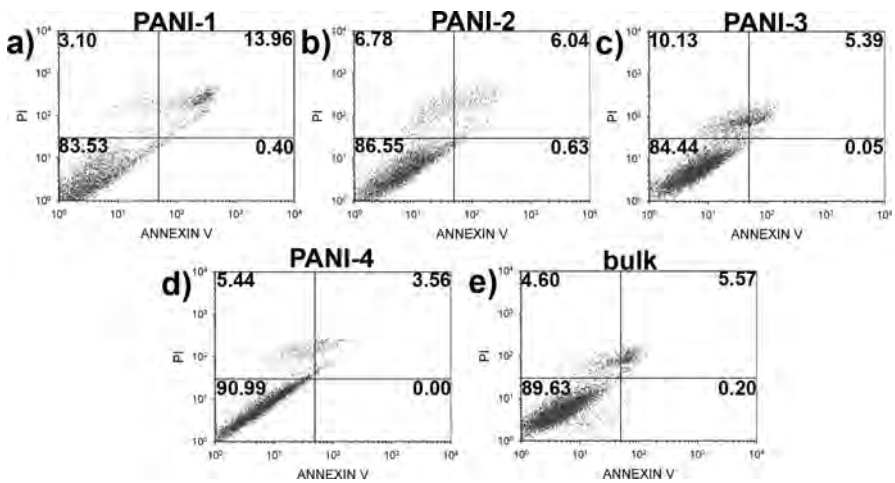

Figure 63. Apoptosis and necrosis on IMR90 affected by (a)PANi–1, (b) PANi–2, (c) PANi–3, (d) PANi–4, and (e) bulk.

ROS has specific effects on the cells, including oxidative damage to DNA and protein. To explore ROS production of PANi nanomaterial treated cells, DCF–DA staining methods were performed (Figure 64). In the presence of ROS, DCF-DA is deacetylated to fluorescent DCF, thus the fluorescent intensity of the cells increased. Untreated cells were used as a negative control to calculate the amount of ROS generation by measuring the percentage of cells with increased fluorescence intensity. The positive control result represented decisive increase 153 % in 5 mM H_2O_2 and decrease with respect to increasing aspect ratio of PANi nanomaterials. The ROS level of PANi–1 was elevated by 64 %, on the other hand, 20 % for that of PANi–4. The results were consistent with the cell viability and cytotoxicity values induced by PANi nanomaterials. As Xia et al. reported that smaller nanoparticles with large surface area and particle number generated more ROS [40], PANi nanomaterials with low aspect ratio induced more ROS in the cells.

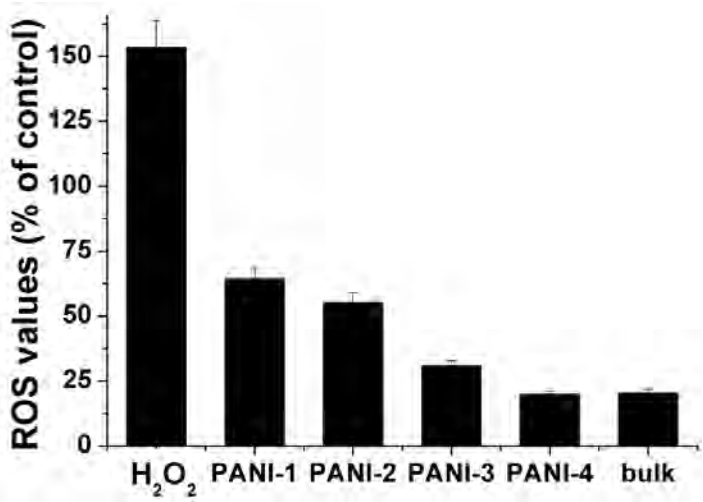

Figure 64. ROS production by IMR90 cell line after incubation with PANi nanomaterials at 24 h (25 μg/well); H_2O_2: 5 mM H_2O_2 as a positive control.

Chapter 4 Conclusions

The cytotoxicity of polymer nanomaterials with controlled sizes and shapes was evaluated by in vitro methods. Furthermore, functional polymer nanomaterials were applied for specific molecule detections. The subtopics could be concluded as follows;

1. PAN nanomaterials as novel bioimaging agents without additional fluorophores were developed by ultrasound induced emulsion polymerization. The PAN nanoparticles exhibited the uniform diameter of *ca.* 40 nm and were well dispersible in aqueous media. The PL properties and amine functional group could be introduced onto the PAN nanoparticles by vapor treatment of EDA. The fluorescence quantum yield of the tPAN nanoparticles was 2.6 times higher than that of DAPI. In addition, the tPAN nanoparticles were low cytotoxic and well uptaken into the SK-BR-3 cells. Bioconjugation with anti-ErbB2 antibody to tPAN nanoparticles allowed active targeting and imaging of breast cancer cells. These tPAN nanoparticles provided potential platform for bioimaging, and disease therapy.

2. An Eu-PAN nanoparticle sensor was prepared for the rapid and sensitive detection of *B. anthracis* spores in aqueous solution. Sensors with Eu-PAN nanoparticles of two different sizes were fabricated by a facile modification, and showed ratiometric detection without calibration based on the internal fluorescence reference (S-PAN). Additionally, the 25 and 50 nm Eu-PAN nanoparticle sensors showed remarkable LOD values, of 10 and 50 pM, respectively, towards Ca-DPA and outstanding selectivity of 160× and 136×, respectively, over aromatic ligands in aqueous solution. The fluorescent PAN nanoparticles and binding with europium complex provide a new direction for the development of rapid, highly sensitive, and selective sensors and could be subsequently expanded to a platform of versatile fluorescence sensors.

4. A novel fluorescent polymeric nanoparticle was synthesized for use as a probe that can selectively detect H_2O_2 over other competing ROS. A new fluorescence peak appeared when the BPAN nanoparticles reacted with H_2O_2, and this peak shifted with a change in the excitation wavelength. This fluorescence behavior was highly specific for H_2O_2. Additionally, the BPAN nanoparticles acted a prochelator, exhibiting increased reactivity toward metal ions after reacting with H_2O_2. The use of these novel nanoparticles to

detect changes in H_2O_2 concentration was demonstrated in macrophage cells. Considering these observations, the BPAN nanoparticles offer a new way to selectively recognize H_2O_2 and scavenge metal ions, and may lead to biomedical applications as an intracellular H_2O_2 sensor and prochelator for use in theragnostics.

5. 1D PEDOT nanomaterials of different shapes represented a meaningful opportunity to study the shape dependence of cytotoxicity and proinflammatory response of nanomaterials. The PEDOT nanomaterials showed aspect ratio-, concentration-, time-dependent cell viability and cytotoxicity. Apoptosis/necrosis and ROS of cells with the PEDOT nanomaterials exhibited similar response with cell viability. In addition, the macrophages with the PEDOT nanomaterials led to elevated levels of proinflammatory cytokines. Other mechanisms including endocytosis rate affects toxicity of cells should be defined by further research. These findings may provide an essential understanding of the geometrical parameters determining toxicity and offer evaluation of the PEDOT nanomaterials for their bio-applications.

6. Monodisperse PPy nanoparticles with five different diameters (termed: 20,

40, 60, 80, and 100 nm) were fabricated *via* chemical oxidation polymerization. We systematically analyzed the cytotoxicity and innate immune response of IMR90 lung fibroblasts and J774A.1 alveolar macrophages incubated with PPy nanoparticles. Cellular uptake of the nanoparticles was observed by TEM. The PPy nanoparticles were internalized into the IMR90 cells *via* endocytosis. In the J774A.1 cells, the nanoparticles were entered *via* both phagocytosis and endocytosis. These endocytosed nanoparticles were transported *via* endosome-network and arrived in lysosomes. The viability of the PPy treated cells was dose- and size-dependent, and the results of apoptosis/necrosis and ROS generation were consistent with the viability results. Among the PPy nanoparticles with different diameters, 60 nm PPy nanoparticles triggered the highest adverse effect on both the cell lines. In the case of innate immune responses, the expression of the CD40 and the CD80 on the macrophages treated with the PPy nanoparticles was up-regulated, while the CD86 was down-regulated in sizes of between 40 nm and 80 nm. These findings may provide better nanotoxicological understanding of polymer nanoparticles, and offer evaluation of the PPy nanoparticles for their bioelectronic applications.

7. The cellular effect of PANi nanomaterial treatment on IMR90 cell line

was investigated by cell viability, cytotoxicity, apoptosis/necrosis, and ROS production. In order to study the toxicity in the view point of shape, concentration, and incubation time, the cell viability of PANi nanomaterials was determined by ATP contents and mitochondrial activites, and the cytotoxicity was based on LDH release. The toxicity was more severe for low aspect ratio PANi nanomaterials than others. Furthermore, PANi nanomaterial treated cells with high concentration and long incubation time showed lower viability than other cells. Apoptosis/necrosis values from PANi nanomaterial treated cells were confirmed the cell viability results. Low aspect ratio PANi nanomaterials produced more ROS than other PANi nanomaterials. Based on these results, lower aspect ratio PANi nanomaterials showed various scopes of adverse effect on the cells than higher aspect ratio PANi nanomaterials.

In summary, PAN nanoparticles with fluorescence were successfully applied for specific molecule detection such as a bioimaging agent, anthrax biomarker, and hydrogen peroxide indicator. These nanoparticles showed enhanced PL intensity *via* PET effect, attachment with various sensing moieties, and biocompatibility. These PAN nanoparticles offer new platform of potential bio- and chemical-sensor. Additionally, conducting polymer

nanomaterials with controlled size and shape were investigated for cytotoxicity assessments. These nanomaterials exhibited size- and shape-dependent toxicity, and this finding was related with their uptake efficiency toward cells. This study may provide new understanding of nanotoxicity and informations for bioapplications of nanomaterials.

References

[1] J. Jang, *Adv. Polym. Sci*. **2006**, *199*, 189.

[2] S. H. Cho, K. T. Song, J. Y. Lee, *Handbook of Conducting Polymers*, 3rd ed. CRC Press, 2003.

[3] H. D. Tran, D. Li, R. B. Kaner, *Adv. Mater*. **2009**, *21*, 1487.

[4] A. B. Kaiser, *Rep. Prog. Phys*. **2001**, *64*, 1.

[5] J. Jang, H. Yoon, *Langmuir* **2005**, *21*, 11484.

[6] J. Jang, J. Bae, *Sens. Actuators B* **2007**, *122*, 7.

[7] C. R. Martin, *Science* **1994**, *266*, 1961.

[8] J. Jang, K. Lee, *Chem. Commun*. **2002**, 1098.

[9] J. Jang, J. Bae, *Chem. Commun.* **2005**, 1200.

[10] J. Jang, J. Bae, *Macromol. Rapid. Commun*. **2005**, *26*, 1320.

[11] J. Jang, S. Kim, K. J. Lee, *Chem. Commun*. **2007**, 2689.

[12] K. J. Lee, W. –K. Oh, J. Song, S. Kim, J. Lee, J. Jang, *Chem. Commun*. **2010**, *46*, 5229.

[13] H. Yoon, M. Choi, K. J. Lee, J. Jang, *Macromol. Res*. **2008**, *16*, 85.

[14] R. A. Petros, J. M. DeSimone, *Nat. Rev. Drug Discovery* **2010**, *9*, 615.

[15] D. A. Giljohann, D. S. Seferos, W. L. Daniel, M. D. Massich, P. C. Patel, C. A. Mirkin, *Angew. Chem. Int. Ed*. **2010**, *49*, 3280.

[16] D. F. Williams, *Biomaterials* **2009**, *30*, 5897.

[17] R. Duncan, *Nat. Rev. Cancer* **2006**, *6*, 688.

[18] J. Jang, J. Bae, E. Park, *Adv. Funct. Mater.* **2006**, *16*, 1400.

[19] L. Chen, C. Chen, R. Li, Y. Li, S. Liu, *Chem. Commun*. **2009**, *45*, 2670.

[20] K. J. Li, J. T. Chen, S. S. Bai, X. Wen, S. Y. Song, Q. Yu, J. Li, *Toxicol. in Vitro* **2009**, *23*, 1007.

[21] X. Liu, J. Zhao, Y. Sun, K. Song, Y. Yu, C. Du, X. Kong, H. Zhang, *Chem. Commun.* **2009**, *44*, 6628.

[22] W. Feng, L.-D. Sun, C.- H. Yan, *Chem. Commun*. **2009**, *44*, 4393.

[23] C. Wu, C. Szymanski, J. McNeill, *Langmuir* **2006**, *22*, 2956.

[24] M. Li, B. Zaman, D. Bardelang, X. Wu, D. Wang, J. C. Margeson, D. M. Leek, J. A. Ripmeester, C. I. Ratcliffe, Q. Lin, B. Yang, and K. Yu, *Chem. Commun.* **2009**, *44*, 6807.

[25] H. –H. Yang, S. –Q. Zhang, F. Tan, Z. –X. Zhuang and X. –R. Wang, *J. Am. Chem. Soc.* **2005**, *127*, 1378.

[26] S. Jin, J. Wang, M. Ji and B. Wang, *Chem. Eur. J.* **2008**, ***14***, 2795.

[27] L. Pu, *Chem. Rev.* **2004**, *104*, 1687.

[28] X. Zhang, L. Chi, S. Ji, Y. Wu, P. Song, K. Han, H. Guo, T. D. James, J. Zhao, *J. Am. Chem. Soc.* **2009**, *131*, 17452.

[29] W. –K. Oh, H. Yoon, J. Jang, *Biomaterials* **2010**, *31*, 1342.

[30] D. A. LaVan, T. McGuire, R. Langer, *Nat. Biotechnol*. **2003**, *21*, 1184.

[31] W. –K. Oh, Y. S. Jeong, K. J. Lee, J. Jang, *Anal. Meth*. **2012**, *4*, 913.

[32] A. Dowling, R. Clift, N. Grobert, D. Hutton, R. Oliver, O. O'neill, J. Pethica, N. Pidgeon, J. Porritt, J. Ryan, *The Royal Academy of Engineering Report* **2004**, *44*, 7.

[33] J. R. McCarthy, R. Weissleder, *Adv. Drug Deli. Rev*. **2008**, *60*, 1241.

[34] W. H. Suh, K. S. Suslick, G. D. Stucky, Y. –H. Suh, *Prog. Neurobio*. **2009**,

87, 133.

[35] C. Sanchez, P. Belleville, M. Popall, L. Nicole, *Chem. Soc. Rev*. **2011**, *40*, 696.

[36] A. E. Nel, L. Mädler, D. Velegol, T. Xia, E. M. V. Hoek, P. Somasundaran, F. Klaessig, V. Castranova, M. Thompson, *Nat. Mater.* **2009,** *8*, 543.

[37] P. V. AshaRani, G. L. K. Mun, M. P. Hande, S. Valiyaveettil, *ACS Nano* **2009**, *3*, 279.

[38] A. Verma, F. Stellacci, *Small* **2010,** *6*, 12.

[39] T. Xia, M. Kovochich, M. Liong, L. Mädler, B. Gilbert, H. Shi, J. I. Yeh, J. I.; Zink, A. E. Nel, *ACS Nano* **2008,** *2*, 2121.

[40] T. Xia, M. Kovochich, M. Liong, H. Meng, S. Kabehie, S. George, J. I. Zink, A. E. Nel, *ACS Nano* **2009,** *3*, 3273.

[41] A. E. Nel, T. Xia, L. Mädler, N. Li, *Science* **2006,** *311*, 622.

[42] S. Kim, W. –K. Oh, Y. S. Jeong, J. –Y. Hong, B. –R. Cho, J. –S. Hahn, J. Jang, *Biomaterials*, **2011**, *32*, 2342.

[43] P. Nativo, I. A. Prior, M. Brust, *ACS Nano* **2008,** *2*, 1639.

[44] H. Jin, D. A. Heller, M. Kalbacova, J. –H. Kim, J. Zhang, A. A. Boghossian, N. Maheshri, M. S. Strano, *Nat Nanotechnol.* **2010,** *5*, 302.

[45] P. Aggarwal, J. B. Hall, C. B. McLeland, M. A. Dobrovolskaia, S. E. McNeil, *Adv. Drug Delivery Rev.* **2009**, *61*, 428.

[46] M. A. Dobrovolskaia, P. Aggarwal, J. B. Hall, S. E. McNeil, *Mol. Pharm.* **2008**, *5*, 487.

[47] M. Tarantola, D. Schneider, E. Sunnick, H. Adam, S. Pierrat, C. Rosman, V. Breus, C. So nnichsen, T. Basché, J. Wegener, A. Janshoff, *ACS Nano*,

2008, *3*, 213.

[48] J. A. Champion, Y. K. Katare, S. Mitragotri, *Proc. Natl. Acad. Sci. USA* **2007**, *104*, 11901.

[49] P. Decuzzi, R. Pasqualini, W. Arap, M. Ferrari, *Pharm. Res.* **2009**, *26*, 235.

[50] K. Midander, P. Cronholm, H. L. Karlsson, Karine Elihn, L. Möller, C. Leygraf, I. O. Wallinder, *Small* **2009**, *5*, 389.

[51] T. Xia, M. Kovochich, J. Brant, M. Hotze, J. Sempf, T. Oberley, C. Sioutas, J. I. Yeh, M. R. Wiesner and A. E. Nel, *Nano Lett.* **2006**, *6*, 1794.

[52] J. Dai, G. L. Baker, M. L. Bruening, *Anal. Chem.* **2006**, *78*, 135.

[53] D. Sehgal, I. K. Vijay, *Anal. Biochem.* **1994**, *218*, 87.

[54] H. Du, R. C. A. Fuh, J. Li, L. A. Corkan and J. S. Lindsey, *Photochem. Photobiol.* **1998**, *68*, 141.

[55] M. G. Dickens, K. J. Franz, *ChemBioChem* **2010**, *11*, 59.

[56] M. G. D. Leed, N. Wolkow, D. M. Pham, C. L. Daniel, J. L. Dunaief, K. J. Franz, *J. Inorg. Biochem.* **2011**, *105*, 1161.

[57] H. Yoon, M. Chang, J. Jang, *Adv. Funct. Mater.* **2007**, *17*, 431.

[58] J. Y. Hong, H. Yoon, J. Jang, *Small* **2010**, *6*, 679.

[59] J. Martínez Urreaga, M. U. de la Orden, *Carbohyd. Polym.* **2007**, *69*, 14.

[60] S. –H. Huang, G. J. Jiang, D. –J. Liaw, C. –L. Li, C. –C. Hu, K. –R. Lee, and J. –Y. Lai, *J. Appl. Polym. Sci.* **2009**, *114*, 1511.

[61] C. Wu, J. McNeill, *Langmuir* **2008**, *24*, 5855.

[62] J. A. Champion, Y. K. Katare, and S. Mitragotri, *Proc. Natl. Acad. Sci. USA*, **2007**, *104*, 11901.

[63] K. J. Lee, J. H. Oh, Y. Kim, J. Jang, *Chem. Mater.* **2006**, *18*, 5002.

[64] K. J. Lee, J. H. Oh, Y. Kim, J. Jang, *Adv. Mater*. **2006**, *18*, 2216.

[65] W. –K. Oh, Y. S. Jeong, J. Song, J. Jang, *Biosens. Bioelectrons*, **2011**, *29*, 172.

[66] A. M. Smith, H. Duan, A. M. Mohs, S. Nie, *Adv. Drug Delivery Rev.* **2008**, *60*, 1226.

[67] F. Osaki, T. Kanamori, S. Sando, T. Sera, Y. Aoyama, *J. Am. Chem. Soc*. **2004**, *126*, 6520.

[68] C. Wu, C. Szymanski, Z. Cain, J. McNeill, *J. Am. Chem, Soc.* **2007**, *129*, 12904.

[69] T. S. Hauck, A. A. Ghazani, W. C. W. Chan, *Small* **2008**, *4*, 153.

[70] M. L. Cable, J. P. Kirby, K. Sorasaenee, H. B. Gray, A. Ponce, *J. Am. Chem. Soc*. **2007**, *129*, 1474.

[71] K. Ai, B. Zhang, L. Lu, *Angew. Chem. Int. Ed*. **2009**, *48*, 304.

[72] J. P. Kirby, M. L. Cable, D. J. Levine, H. B. Gray, A. Ponce, *Anal. Chem*. **2008**, *80*, 5750.

[73] J. C. Harper, R. Polsky, D. R. Wheeler, D. M. Lopez, D. C. Arango, S. M. Brozik, *Langmuir* **2009**, *25*, 3282.

[74] K. J. Lakshmi, M. Auger, J. Raap, J. Lugtenburg, R. G. Griffin, J. Herzfeld, *J. Am. Chem. Soc.* **1993**, *115*, 8515.

[75] E. G. Occhiato, F. L. Galbo, A. Guarna, *J. Org. Chem.* **2005**, *70*, 7324.

[76] J. Lin, Q. –S. Hu, M. –H. Xu, L. Pu, *J. Am. Chem. Soc.* **2002**, *124*, 2088.

[77] A. R. Lippert, T. Gschneidtner, C. J. Chang, *Chem. Commun.* **2010**, *46*, 7510.

[78] M. Abo, Y. Urano, K. Hanaoka, T. Terai, T. Komatsu, T. Nagano, *J. Am. Chem. Soc.* **2011**, *133*, 10629.

[79] M. G. Dickens, K. J. Franz, *ChemBioChem* **2010**, *11*, 59.

[80] M. G. D. Leed, N. Wolkow, D. M. Pham, C. L. Daniel, J. L. Dunaief, K. J. Franz, *J. Inorg. Biochem.* **2011**, *105*, 1161.

[81] A. Changela, K. Chen, Y. Xue, J. Holschen, C. E. Outten, T. V. O'Halloran, A. Mondragón, *Science* **2003**, *301*, 1383.

[82] H. Yoon, J. –Y. Hong, J. Jang, *Small* **2007**, *3*, 1774.

[83] J. Jiang, G. Oberdörster, P. Biswas, *J. Nanopart. Res.* **2009**, *11*, 77.

[84] H. –J. Yen, S. –H. Hsu, C. –L. Tsai, *Small* **2009**, *5*, 1553.

[85] K. Pulskamp, S. Diabaté, H. F. Krug, *Toxicol. Lett.* **2007**, *168*, 58.

[86] S. M. Hirst, A. S. Karakoti, R. D. Tyler, N. Sriranganathan, S. Seal, C. M. Reilly, *Small* **2009**, *5*, 2848.

[87] P. V. AshaRani, G. L. K. Mun, M. P. Hande, S. Valiyaveettil, *ACS Nano* **2009**, *3*, 279.

[88] G. Oberdörster, E. Oberdörster, J. Oberdörster, *Environ. Health Persp.* **2005**, *113*, 823.

[89] A. Nel, T. Xia, L. Mädler, N. Li, *Science* **2006**, *311*, 622.

[90] Y. Pan, A. Leifert, D. Ruau, S. Neuss, J. Bornemann, G. Schmid, W.Brandau, U. Simon, W. Jahnen-Dechent, *Small* **2009**, *5*, 2067.

[91] K. Midander, P. Cronholm, H. L. Karlsson, Karine Elihn, L. Möller, C. Leygraf, I. O. Wallinder, *Small* **2009**, *5*, 389.

[92] M. A. Dobrovolskaia, D. R. Germolec, J. L. Weaver, *Nat. Nanotechnol.* **2009**, *4*, 411.

[93] H. Huang, E. Pierstorff, E. Osawa, D. Ho, *Nano Lett.* **2007**, *7*, 3305.

[94] B. D. Chithrani, W. C. W. Chan, *Nano Lett.* **2007**, *7*, 1542.

[95] M. Auffan, J. Rose, J. Y. Bottero, G. V. Lowry, J. P. Jolivet, M. R. Wiesner, *Nat. Nanotechnol.* **2009**, *4*, 634.

[96] Y. Yuan, C. Liu, J. Qian, J. Wang, Y. Zhang, *Biomaterials* **2010**, *31*, 730.

[97] A. K. Madl, K. E. Pinkerton, *Crit. Rev. Toxicol.* **2009**, *39*, 629.

[98] K. Kostarelos, L. Lacerda, G. Pastorin, W. Wu, S. Wieckowski, J. Luangsivilay, S. Godefroy, D. Pantarotto, J.-P. Briand, S. Muller, M. Prato, A. Bianco, *Nat. Nanotechnol.* **2007**, *2*, 108.

[99] S. D. Conner, S. L. Schmid, *Nature* **2003**, *422*, 37.

[100] M. A. Dobrovolskaia, S. E. McNeil, *Nat. Nanotechnol.* **2007**, *2*, 469.

[101] G. J. Doherty, H. T. McMahon, *Annu. Rev. Biochem.* **2009**, *78*, 857.

[102] Q. Mu, D. L. Broughton, B. Yan, *Nano Lett.* **2009**, *9*, 4370.

[103] J. A. Khan, B. Pillai, T. K. Das, Y. Singh, S. Maiti, *ChemBioChem* **2007**, *8*, 1237.

[104] P. Nativo, I. A. Prior, M. Brust, *ACS Nano* **2008**, *2*, 1639.

[105] W. –K. Oh, S. Kim, H. Yoon, J. Jang, *Small* **2010**, *6*, 872.

[106] N. G. Bastús, E. Sánchez-Tilló, S. Pujals, C. Farrera, C. López, E. Giralt, A. Celada, J. Lloberas, V. Puntes, *ACS Nano* **2009**, *3*, 1335.

[107] J. Palomäki, P. Karisola, L. Pylkkänen, K. Savolainen, H. Alenius, *Toxicology* **2010**, *267*, 125.

[108] W. Jiang, B. Y. S. Kim, J. T. Rutka, W. C. W. Chan, *Nat. Nanotechnol.* **2008**, *3*, 145.

[109] B. D. Chithrani, A. A. Ghazani, W. C. W. Chan, *Nano Lett* **2006**, 6, 662.

[110] H. U. Simon, A. Haj-Yehia, F. Levi-Schaffer, *Apoptosis* **2000**, *5*, 415.

[111] Y. Yuan, C. Liu, J. Qian, J. Wang, Y. Zhang, *Biomaterials* **2010**, *31*, 730.

[112] B. C. Schanen, A. S. Karakoti, S. Seal, D. R. Drake III, W. L. Warren, W. T. Self, *ACS Nano* **2009**, *3*, 2523.

[113] P. D. Dwivedi, A. Misra, R. Shanker, M. Das, *Nanotoxicology* **2009**, *3*, 19.

[114] H. Vallhov, S. Gabrielsson, M. Strømme, A. Scheynius, A. E. Garcia-Bennett, *Nano Lett*. **2007**, *7*, 3576.

[115] Y. Pan, S. Neuss, A. Leifert, M. Fischler, F. Wen, U. Simon, G. Schmid, W. Brandau, W. Jahnen-Dechent, *Small* **2007**, *3*, 1941.

[116] H. Dumortier, S. Lacotte, G. Pastorin, R. Marega, W. Wu, D. Bonifazi, J. -P. Briand, M. Prato, S. Muller, A. Bianco, *Nano Lett*. **2006**, *6*, 1522.

초 록

기능성 고분자 나노물질은 화학산화중합과 에멀젼 주형 중합방법을 이용해 제조되었고, 이는 세포독성과 세포 영향에 대해 조사되었다. 더불어 이 기능성 고분자 나노물질은 특정분자의 검출에도 적용되었다. 특히 표면 개질된 폴리아크릴로니트릴 나노입자는 세포이미징, 탄저균 검출, 단당류 검출, 세포내 과산화수소 센서로 이용되었다. 또한 폴리피롤, 폴리아닐린, 피돗 등의 전도성 고분자 나노물질들은 균일한 모양과 크기로 제조되어 이를 나노독성평가에 응용하였다. 폴리아크릴로니트릴 나노입자의 에틸렌디아민의 기상처리를 통해 형광을 나타내었고, 표면의 항체처리를 통해 선택적인 세포이미징을 할 수 있었다. 시프베이스 처리된 폴리아크릴로니트릴 나노입자는 희토류 분자와의 결합을 통해 탄저균마커로 사용하였다. 이들 나노입자는 내부 형광 때문에 비율 측정이 가능하고, 이들은 놀라운 검출 한계 (10 피코몰)과 뛰어난 선택성 (160배)를 나타내었다. 보론 산 에스터 처리된 폴리아크릴로니트릴 나노입자는 선택적인 세포내 과산화수소 검출에 사용되었다. 광전자 이동효과와 금속 흡착 능력은 이물질이 다양한 바이오 분야에 응용가능함을 보여주었다. 다양한 모양의

피돗 나노물질은 세포독성 및 면역 반응에 대해 조사되었다. 다양한 크기의 폴리피록 나노입자는 크기비례의 세포독성에 대해 조사되었다. 종횡비가 다른 폴리아닐린 나노물질은 인간 섬유아세포에 대해 독성이 조사되었다. 이러한 결과들은 크기별, 모양별의 전도성 고분자 나노물질의 세포독성에 대한 중요한 정보들을 제공하게 될 것이다.

주요어: 기능성 고분자 나노물질; 세포 독성; 바이오이미징; 특정 분자 검출; 탄저균 검출
학 번: 2009-30244

감사의 글

석박사과정 5년 6개월여가 너무 빨리 지나갔습니다. 돌아보면 저에게는 큰 행운이 계속 찾아왔습니다. 연구분야를 잘 모르던 제가 막연하게 고분자를 해보겠다는 생각이 든 것, 물어 물어 장정식 교수님 연구실이 연구를 잘한다는 소식을 듣고 혹시나 해서 지원을 하게 된 것, 교수님께서 처음에 부정적이셨음에도 계속적인 면담을 통해 교수님 마음을 움직이게 된 것, 좋은 선배들을 만나게 된 것, 박사과정에 진학하게 된 것, 새로운 연구분야를 선택하게 된 것, 논문들이 해외 저널에 비교적 잘 통과된 것, 좋은 후배들을 만나게 된 것, 결혼을 하면서 마음에 안정을 찾게 된 것, 비교적 빠른 시간 내에 졸업을 하게 된 것 등 너무나 부족한 제가 박사가 된 건 기적이라 할 수 있습니다. 물론 이렇게 석박사과정을 잘 마치게 된 것에 감사해야 할 분들이 많습니다.

우선 제 길은 인도하시는 하나님께 감사드립니다. “나의 가는 길을 오직 그가 아시나니 그가 나를 단련하신 후에는 내가 정금 같이 나오리라.” (욥23:10) 부족한 저의 인생이 하나님께 영광 돌리는 삶이 되고 싶습니다. 제 삶의 모습이 십년, 이십년 뒤에 어떤 모습이 될지 기대합니다. 또한 지도교수님이신 장정식 교수님께 감사드립니다. 매일 매일 한결같이 새벽에 출근하셔서 늘 학생들을 챙기시고, 연구에 몰입하시는 모습은 제가 우러러 볼 수 밖에 없게 만듭니다. 저나 다른 학생들이 말썽을 피워도 자식처럼 이해해 주시고, 평상시와 다름없이 대해주시는 모습에 저도 그런 모습으로 살아야겠다라는 다짐을 하게 만듭니다. 교수님 지도하에서 연구에 대해 많이 배우고, 제 주제보다 높게 좋은 결과를 얻게 되었습니다. 감사드립니다. 그리고, 박사학위심사에서 지도해 주신 조재영 교수님, 김영규 교수님, 이종찬 교수님, 그리고 KIST 임순호 박사님께 감사드립니다. 특히 우리과에는 좋은 교수님들이 많아 계시는데, 제 삶에 자극을 많이 받고, 지식에 대한 갈망을 갖게 해주십니다. 이번 박사학위심사를 통해서 발표하는 법, 논문 작성하는 법, 연구를 진행하는 법을 잘 배웠습니다.

실험실에서 만난 동료들도 평생 잊지 못할 것 같습니다. 석사로 들어와 아무 것도 모르던 저를 교육해 준 사수 현석이 형, 일본 같이 갔던 경진이, 논문 쓰는 것도 많이 배웠고, 운동도 같이 많이 했었는데, 특허 가르쳐 주던 문정이, 일 같이

하면서 많이 배우고 재밌었다. 엄마같이 잘 챙겨주던 혜영이, 내가 두 번이나 다치게 했던 준혁이, 미안하다. 옆자리에서 말 동무해주던 은유형, 쿨한 오영이, 실험실 생활에서 동무가 되어준 진용이, 추억을 많이 만들어 주어 고맙다. 동기 사훈이, 찬희 너희들이 도와줘서 실험실에 잘 적응할 수 있었어 감사해. 포르투갈 친구 주영이 파이팅! 같은 바이오팀에서 수고해준 너무 고마운 소진이, 너 때문에 여기까지 왔다. 또 너무 고생한 (정)윤선이, 고맙고, 회사에서도 잘 되길 바래. 부족한 고참 만나 고생하는 인규, (장)윤선, 슬기 모두 원하는 걸 이루길 바래. 또 오석, 경환, 천재 현택이, 근영, 은우, 선주, 선혜, 성훈, 유정, 준섭, 민규, 승애, 중현, 현영, 수임, 선아, 송희, 제임스, 종민, 동훈이 모두 고분자재료실험실에서 많은 지식을 쌓고 졸업하길 바랍니다.

늘 기도해주시는 어머니, 그리고 항상 도와주는 누나들에게 감사드립니다. 늘 관심 갖아주시는 장모님, 처형들, 처제에게도 감사드립니다. 마지막으로 어려운 시기에 결혼해주어 뒷바라지 해주는 현모양처 '김소정' 에게도 감사 드립니다. 이제는 점점 '현숙한 여인' 이 되어가는 모습에서 제가 행운아라는 생각이 듭니다. 그리고 너무 귀여운 하랑아 사랑한다.

너희는 눈을 높이 들어 누가 이 모든 것을 창조하였나 보라 주께서는 수효대로 만상을 이끌어 내시고 각각 그 이름을 부르시나니 그의 권세가 크고 그의 능력이 강하므로 하나도 빠짐이 없느니라 야곱아 네가 어찌하여 말하며 이스라엘아 네가 어찌하여 이르기를 내 사정은 여호와께 숨겨졌으며 원통한 것은 내 하나님에게서 수리하심을 받지 못한다 하느냐 너는 알지못하였느냐 듣지못하였느냐 영원하신 하나님 여호와, 땅끝까지 창조하신 자는 피곤치 아니하시며 곤비치 아니하시며 명철이 한이 없으시며 피곤한 자에게는 능력을 주시며 무능한 자에게는 힘을 더하시나니 소년이라도 피곤하며 곤비하며 장정이라도 넘어지며 자빠지되 오직 여호와를 앙망하는 자는 새 힘을 얻으리니 독수리의 날개치며 올라감 같은 것이요 달음박질하여도 곤비치 아니하겠고 걸어가도 피곤치 아니하리로다 사 40:26-31